[UCI]I804:24011-200000237459

2009年 2月
博士學位論文

交流 電磁氣場 可視化 시스템의 開發 및 應用

朝鮮大學校 大學院

情報通信工學科

全 鍾 虞

交流 電磁氣場 可視化 시스템의 開發 및 應用

Development and Application of Visualization System of Alternative Electro-Magnetic Field

2009年　2月　25日

朝鮮大學校 大學院

情報通信工學科

全 鍾 虞

交流 電磁氣場 可視化 시스템의 開發 및 應用

指導敎授　李　鎭　伊

이 論文을 工學 博士學位申請 論文으로 提出함

2008年　10月

朝鮮大學校 大學院

情報通信工學科

全 鍾 虞

全鍾虞의 博士學位 論文을 認准함

委員長 朝鮮大學校 教授 ___________印

委員 朝鮮大學校 教授 ___________印

委員 朝鮮大學校 教授 ___________印

委員 朝鮮大學校 教授 ___________印

委員 (주)포스코 책임연구원 ___________印

2008年 12月

朝鮮大學校 大學院

Contents

ABSTRACT

I. INTRODUCTION 1

II. DEVELOPED TECHNOLOGIES 14

A. MAGNETIC CAMERA 14

B. TECHNOLOGIES FOR THE VISUALIZATION OF AN ALTERNATIVE ELECTRO-MAGNETIC FIELD 15

1. Hall Sensor and Signal Processing Circuit 15

2. Magnetic Sources 18

a. Vertical type magnetic field 20

b. Sheet type induced current 20

c. Improved sheet type induced current 21

d. Combined induced current – magnetic flux leakage 22

C. QUANTITATIVE ANALYSIS ALGORITHM 25

III. APPLICATIONS 30

A. NDT OF THE AUSTENITIC STAINLESS STEEL 30

1. Specimen 33

2. Experiments 36

a. Real time inspection of the crack by using a HSA 36

b. Evaluation of the crack using SSS 37

3. Discussions 44

B. NDT OF THE ALUMINUM ALLOY 45

1. Specimen 46

2. Experiments 47

3. Discussions 60

C. NDT OF COLD ROLLED STEEL 61

1. *Specimens* 61
2. *Experimental Equipment* 63
3. *Discussions* 65
D. NDT OF INCONEL BY PENETRATING OF THE MAGNETIC FLUID 72
1. *Principles* 73
a. Penetrating of the magnetic fluid 73
b. Numerical analysis of EMF 74
2. *Specimen and Experimental Equipment* 79
a. Specimen 79
b. Experimental equipment 81
3. *Discussions* 82
E. DISCRIMINATION OF METALLIC COIN 89
1. *Prologue* 90
2. *Specimens* 92
3. *Discussions* 93
IV. CONCLUSIONS 98
REFERENCE 101
ACKNOWLEDGMENTS 106

List of Tables

Table 1 The class of magnetic sources..19
Table 2 Dimensions of each crack 34
Table 3 Aluminum alloy Al7075 specimens of several shapes and crack sizes..........................46
Table 4 Shapes and sizes of each crack 62
Table 5 Shapes and Sizes of each crack..81
Table 6 Coins(KR:Korea, EU:Europe, US:United Stated, JP:Japan, CH:China, PL:Poland, IN:Indonesia, NZ:Newzland, GM:Germany, EL:England) 92

List of Figures

Fig. 1-1 Schematic diagram of RHR steam condensation lines and HPCI (http://www.nisa.meti.go.jp/english/0207eng.pdf)....2

Fig. 1-2 Restoration of ruptured pipe section (http://www.nisa.meti.go.jp/english/0207eng.pdf).2

Fig. 1-3 Destructed position (http://www.casa.gov.au/fsa/2005/aug/28-33.pdf) 5

Fig. 1-4 Destructed position (http://www.casa.gov.au/fsa/2005/aug/28-33.pdf) 6

Fig. 1-5 Eschede train disaster (http://en.wikipedia.org/wiki/File:Ice_eschede_1.jpg) 8

Fig. 1-6 Details of derailing accident (http://shippai.jst.go.jp/en/Detail?fn=2&id=CA1000637) .8

Fig. 1-7 Magnetic particle testing (http://www.lavender-ndt.co.uk/serv/training/mt.asp)....10

Fig. 1-8 Magnetic flux leakage (http://www.battelle.org/pipetechnology/MFL/MFL98Main.html#Implementation)....11

Fig. 1-9 Eddy current testing....12

Fig. 2-1 Magnetic camera....14

Fig. 2-2 Area-type magnetic camera 16

Fig. 2-3 High pass filter and a low noise operational amplifier construction for high precision measurement system. 17

Fig. 2-4 3rd order Butterworth low pass filter....17

Fig. 2-5 Principles of sheet-type induced current....21

Fig. 2-6 Improved sheet-type induced current....22

Fig. 2-7 Numerical analysis of the electro-magnetic field around each crack using a small yoke-type magnetizer operated by an alternative current of 1 kHz: (a) analysis model; (b) magnetic field on the y-directional crack; (c) magnetic field on the x-directional crack; (d) electric field on the y-directional crack; and (e) electric field on the x-directional crack....24

Fig. 2-8 Components of a scan-type magnetic camera with high precision scanning system. 26

Fig. 2-9 Crack evaluation algorithm of the DC type magnetic camera. 27

Fig. 2-10 Crack evaluation algorithm of the AC type magnetic camera....28

Fig. 3-1 Schematics of the sheet type induced current (STIC) 32
Fig. 3-2 Extraction of the amplitude of alternating current signal due to crack existence....33
Fig. 3-3....Geometry of the investigated austenitic stainless steel specimen (Unit: mm, thickness: 10mm).... 34
Fig. 3-4 Detection result of crack No.5 at 6.4 kHz by using MOI 308/3 (Produced by PRI)....35
Fig. 3-5 Photograph of the Hall sensor array(HAS) 36
Fig. 3-6 Experimental results using HAS 37
Fig. 3-7 Distributions of $DRMS_{HIGH}$ and $\partial D_{HIGH}/\partial x$ by using 38
Fig. 3-8 Factors for evaluation of a crack....39
Fig. 3-9 Relationship between the NDE factors and the crack parameters (D_C, L_C and W_C) 41
Fig. 3-10 Comparison of calculated crack depths by using Eq. (6) and Eq. (11) 43
Fig. 3-11 Comparison of calculated crack volumes by using Eq. (10), Eq. (12) and $Max[\partial(D_{LOW})/\partial x]$....44
Fig. 3-12 Shapes of crack on each specimen.....46
Fig. 3-13 Schematics of the transformer to induce the sheet type current on a specimen and the 3-dimensional scanning equipment.....47
Fig. 3-14 Distributions of the root mean squared value (V_{RMS}) at 3.2 kHz on each crack. 49
Fig. 3-15 Distributions of the root mean squared value (V_{RMS}) at 25.6 kHz on each crack. 50
Fig. 3-16 Relationship between the θ_{TIP} and Δl_C. 51
Fig. 3-17 Relationship between center position of maximum V_{RMS} versus depth of crack and frequency of induced current. 51
Fig. 3-18 Processed images of root mean squared value ($\partial V_{RMS}/\partial x$) at each frequency (3.2 kHz and 25.6 kHz)....53
Fig. 3-19 Processed images of root mean squared value ($\partial V_{RMS}/\partial y$) at each frequency (3.2 kHz and 25.6 kHz)....54
Fig. 3-20 Relationship between θ_{TIP} and (a) Δl_{dx}, (b) $\Delta l_{dy.}$ 55
Fig. 3-21 Relationship between AvrMax[V_{RMS}], AvrMax[$\partial V_{RMS}/\partial x$], AvrMax[$\partial V_{RMS}/\partial y$] and D_{CRACK}, S_{CRACK}, V_{CRACK}....56
Fig. 3-22 D_{CRACK}, $L_{CRACK(exp3.2 \text{ and } exp25.6)}$, $S_{CRACK(section\ area)}$, V_{CRACK} versus the normalized sampling standard deviation of each factor; (1) $\Delta l_C^{3.2}$, (2) AvrMax[$V_{RMS}^{3.2}$], (3) $\Delta l_{dx}^{3.2}$, (4) AvrMax[$\partial V_{RMS}/\partial x^{3.2}$], (5) $\Delta l_{dy}^{3.2}$, (6) AvrMax[$\partial V_{RMS}/\partial y^{3.2}$], (7) $\Delta l_{dxdy}^{3.2}$, (8) AvrMax[$\partial^2 V_{RMS}/\partial x \partial y^{3.2}$], (9) $\Delta l_C^{EXP3.2}$ (10) $\Delta l_C^{25.6}$, (11) AvrMax[$V_{RMS}^{25.6}$], (12) $\Delta l_{dx}^{25.6}$, (13) AvrMax[$\partial V_{RMS}/\partial x^{25.6}$], (14) $\Delta l_{dy}^{25.6}$, (15) AvrMax[$\partial V_{RMS}/\partial y^{25.6}$], (16) $\Delta l_{dxdy}^{25.6}$, (17)

$AvrMax[\partial^2 V_{RMS}/\partial x \partial y^{25.6}]$, (18) $\Delta l_C^{EXP25.6}$. 58
Fig. 3-23 Cold rolled steel specimen. 62
Fig. 3-24 Experimental equipment. 63
Fig. 3-25 Numerical analysis of the electro-magnetic field around each crack using a small sized yoke type magnetizer operated by an alternative current of 1kHz: (a) Analysis model; (b) Magnetic field on the y-directional crack; (c) Magnetic field on the x-directional crack; (d) Electric field on the y-directional crack; (e) Electric field on the x-directional crack. 64
Fig. 3-26 Linearly integrated 64 InSb Hall sensor array on a NiZn ferrite wafer. 65
Fig. 3-27 Experimental results for the horizontal direction with a rolling direction 66
Fig. 3-28 Experimental results for the vertical direction with a rolling direction 67
Fig. 3-29 A-A' section view of each crack seen in Fig. 3-27 68
Fig. 3-30 B-B' section view of each crack seen in Fig. 3-28 69
Fig. 3-31 Evaluation of the slit type crack volume using the proposed algorithm 70
Fig. 3-32 Evaluation of the hole type crack volume using the proposed algorithm 71
Fig. 3-33 Small yoke-type magnetizer and analysis model; (a) photograph, (b) analysis model ..75
Fig. 3-34 Analyzed distribution of magnetic field on the Inconel specimen with DC current supply; (a) x-directional crack with magnetic fluid penetration, (b) y-directional crack with magnetic fluid penetration 77
Fig. 3-35 Analyzed distribution of magnetic and electric field on the Inconel specimen with AC current supply; (a) magnetic field on x-directional crack with magnetic fluid penetration, (b) electric field on x-directional crack with magnetic fluid penetration, (c) magnetic field on y-directional crack with magnetic fluid penetration, (d) electric field on y-directional crack with magnetic fluid penetration 78
Fig. 3-36 Inconel specimen 80
Fig. 3-37 Experimental equipment 82
Fig. 3-38 $\partial V_{RMS}/\partial x$ distributions obtained by scanning to the x-direction with CIC-MFL method 83
Fig. 3-39 $\partial V/\partial y$ distributions obtained by scanning to the y-direction with CIC-MFL method....84
Fig. 3-40 Section view of $\partial V_{RMS}/\partial x$ on each crack at Fig. 3-38 85
Fig. 3-41 Section view of $\partial V/\partial y$ on each crack at Fig. 3-39 86
Fig. 3-42 Evaluation of the crack volume using the proposed algorithm without D2, D3, D5, E2, E3, and E5 87
Fig. 3-43 Small size yoke type electromagnetic coil operated by alternative current. 91

Fig. 3-44 Coins, $\partial V_{RMS}/\partial x$ images and section view 94
Fig. 3-45 Diameters and weight of each coin. Group① is PL-2grosze(◁) and US-1dime(≑). Group② is US-1cent(▲), NZ-5cent(⬢), and PL-5groszy(⊲). Group③ is PL-10groszy(⋊), CH-5jiao(◆), and JP-50yen(⋇). Group④ is JP-50yen(⋇), EU-5cent(●), and KR-50won(⊞), Group⑤ is KR-100won(⊠), and JP-50yen(⋇). Group⑥ is US-5cent(△), EL-20pence(⬠), and PL-2ztote(◀). Group⑦ is JP-100yen(▽), and PL-1ztoty(◀). Group⑧ GM-1mark(☆), KR-100won(⊠), US-25cent(⩕), and IN-500rupiah(b)(⋈). Group⑨ is KR-500won(⊟), and JP-500yen(▼)....................95
Fig. 3-46 Relationship between the peak-distance and the integrated absolute minimum value of the $\partial V_{RMS}/\partial x$....................96
Fig. 3-47 Coin discriminating algorithm. 97

Nomenclature

RHR	: Residual heat removal
SORs	: Safe operation rules
HPCI	: High pressure coolant injection
SDT	: Spin dependent tunneling
OL&C	: Operating limits and conditions
HX-B	: Heat exchanger B
NISA	: Nuclear and industrial safety agency
METI	: Ministry of economy trade and industry
NDT	: Nondestructive Testing
PSI	: Pre-service inspection
ISI	: In-service inspection
MT	: Magnetic particles testing
MFLT	: Magnetic flux leakage testing
ECT	: Eddy current testing
PT	: Penetration testing
ADC	: Analog to digital converter
MR	: Magnetic resistance
GMR	: Giant magnetic resistance
FSO	: Full scale operational range
SDT	: Spin-dependent tunneling
SSS	: Single sensor scanning
LIHaS	: Linearly integrated Hall sensor array
AIHaS	: Area type integrated Hall sensor array
CIC-MFL	: Combined induced current – magnetic flux leakage
STIC	: Sheet type induced current
i-STIC	: Improved sheet type induced current
C-MFL	: Cross type magnetic flux leakage

DC-MFL	: Direct current magnetic flux leakage
P-MFL	: Plate type magnetic flux leakage
IS-MFL	: In-side solenoid magnetic flux leakage
V-MFL	: Vertical type magnetic field leakage
MFPT	: Magnetic fluid penetration testing
MT	: Magnetic Particle Testing
MO	: Magneto-optical
MOI	: Magneto-optical/eddy current imaging
HSA	: Hall sensor array
HPF	:High pass filter
LPF	: Low pass filter
AC	: Alternating current
DC	: Direct current
A-STS	: Austenitic stainless steel
PMR	: Partially magnetized region
H	: Strength of magnetic field [A/m]
RMS	: Root-mean-squared
SSS	: Single Hall sensor scanning
DRMS	: Distribution of root mean square [V/mm]
D	: Depth of the crack [mm]
W	: Width of the crack [mm]
L	: Length of the crack [mm]
Jt	: Density of the induced current on the subsurface $[A/m^2]$
t	: Thickness [mm]
δ	: Skin depth [mm]
f	: Frequency [Hz]
μ	: Permeability [H/m]
σ	: Electrical conductivity [A/V]
$\partial D/\partial x$	: The differential RMS of Hall voltage to the STIC direction [V/mm]
Diameter[$\partial D/\partial x$]	: The interval between the maximum position and the minimum

position [mm]

Distance[$\partial D/\partial x$] : The distance between each set of maximum positions [mm]

Max[$\partial D/\partial x$] : The average of the maximum values of $\partial D/\partial x$ [V/mm]

S : The section area of the crack [mm^2]

V : The volume of the crack [mm^3]

Subscripts

RMS : Root-Mean-Square

C : Crack

EXT : External magnetization

S : Critical saturation

HIGH : High spatial resolution by using single Hall sensor scanning

LOW : Low spatial resolution by using the Hall sensor array

MAG : Angle between the Magnetization direction and the Crack length direction[deg]

MAX : Maximum value of the differential RMS of Hall voltage to the STIC direction[V/mm]

MIN : Minimum value of the differential RMS of Hall voltage to the STIC direction[V/mm]

TIP : Angle between the surface of the specimen and the edge of the crack tip in the direction of depth

Superscripts

$'$: Calculated by S_C divide L_C

3.2 : 3.2kHz Frequency of the STIC

25.6 : 25.6kHz Frequency of the STIC

EXP : Expectation

요 약

교류 전자기장 가시화 시스템의 개발 및 응용

Jun Jongwoo
Advisor : Prof. Jinyi Lee Ph.D.
Department of Information and Communications Engineering,
Graduate School of Chosun University

원자력발전소, 항공기등을 구성하는 구조재의 많은 부분이 알루미늄, 인코넬 및 스테인리스강등과 같은 상자성체(Paramagnetic material) 및 강자성체(Ferromagnetic material)와 상자성체가 혼재된 재질에 의하여 구성되어 있다. 이들의 형태 및 크기, 또는 균열 및 손상 등을 가시화하고 정량적으로 평가하기 위해서는 기존의 정자기장 가시화 기술에 기반한 자기카메라는 한계를 가지고 있다.

본 연구에서는 교류 자기장을 측정, 가시화하고 해석할 수 있는 교류형 자기 카메라를 제안한다. 제안한 자기카메라는 자원과 대상물, 2차원 배열의 자기센서와 3차원 형상의 자기렌즈, A/D 변환기와 컴퓨터 및 모니터로 구성된다. 이들 구성에 의하여 대상물의 형상 또는 결함 주위의 자기장을 자기렌즈로 집속하여 자기센서 배열에 의하여 전기신호로 변환하여 육안으로는 볼 수 없는 자기분포를 기록하고, 해석하기 위한 정량적인 기초 데이터를 얻을 수 있다. 이들 자원으로는 강자성체인가, 또는 상자성체 금속인가에 따라 전자석, 유도전류, 헬름헬츠 코일, 지자기와 같은 정자기장(Static Magnetic Field) 또는 유도형 전자기장(induced magnetic field)을 이

용한다.

본 논문에서는 상자성체 재료 또는 강자성체와 상자성체가 혼재하는 구조물을 가시화하거나 비파괴검사가 가능하도록 하기와 같이 교류형 자기카메라를 개발하여 그 결과를 확인하였다.

1. 자원(Magnetic Source)에 관한 연구 : 상자성체 및 강자성체와 상자성체가 혼재하는 재료에 교류 전자기장의 도입으로 유도전류를 발생시키는 복합 유도전류-누설자속법(CIC-MFL, Combined Induced Current-Magnetic Flux Leakage)과 유도면전류법(STIC, Sheet Type Indeced Current)에 의하여 상기 구조물로부터 전자기장을 유도하고, 균열의 존재에 기인한 자기장의 변화를 가시화하고, 해석하였다.

2. 센서(Sensor head)에 관한 연구 : 교류 전자기장을 측정하기 위해서 홀센서를 사용하였는데 홀센서의 선형 집적화를 통한 높은 분해능을 얻을 수 있었고, 배열에 의한 간섭의 최소화 및 구동회로의 간략화를 이룰 수 있었다.

3. 교류용 자기카메라에 적합한 회로에 관한 연구 : 상자성체 및 강자성체가 혼재된 재질에서 결함의 데이터를 추출하고, 낮은 주파수 잡음을 제거하기 위해서 HPF(High Pass Filter)를 전처리부에 도입하고, 저전력 저잡음 고주파용 op-amp의 도입으로 미약한 결함의 신호를 얻을 수 있었으며, A/D 변환기와 컴퓨터의 빠른 신호처리와 신호해석의 용의함을 위해 RMS(Root Mean Square)회로를 도입하여 보다 더 정밀하고 빠르게 결함 신호를 처리할 수 있었다.

4. 정량평가(Quantitative NDE) 및 역해석(Inverse problem)에 관한 연구 : 자기카메라에 의하여 추출된 정보로부터 결함을 정량평가하기 위한 정해석 및 역해석 알고리즘에 대하여 연구하였다.

5. 다양한 적용분야의 가능성 평가 : 원자력발전소에서 많이 사용하는 오스테나이트계 스테인레스강, 인코넬 구조재, 니켈을 코팅한 인코넬 시험편을 이용하여 상자성체 또는 강자성체와 상자성체가 혼재된 상태의 구조물의 결함을 효율적으로 검출하는 분야에 활용하였다. 또한, 경년항공기의 수명관리를 위한 비파괴검사 적용가능성을 확인하기 위하여 알루미늄 합금 시험편의 인공결함 및 피로균열의 탐상및 평가에 적용하였다. 또한 세계 각국 동전의 자기카메라 영상으로부터 진위 여부의 판별방법을 제안하였다.

이러한 연구에 의하여 교류 전자기장을 측정, 가시화하고 해석할 수 있는 교류스캔형 자기카메라를 기술적으로 실현하였고, 강자성체, 상자성체는 물론, 상자성체 및 강자성체가 혼재된 재료에서도 이면 및 표면 결함을 측정할 수 있어 차세대 에너지 기기, 로켓, 항공기, 교각, 차량, 고층건축, 플랜트 등 대형기기구조물에 내재하는 손상의 고정도 평가와 예측수법의 확립에 의하여 신뢰성 및 안전성을 잃지 않을 정도의 손상은 허용하는 이른바 손상허용 공학적 재료평가가 가능하게 되어 21세기의 차세대 대형기기의 고 신뢰성 혹은 향후 심각한 사회문제로 될 가능성이 농후한 경년기기 및 구조물의 수명평가 정도의 비약적 향상이 기대된다.

I. INTRODUCTION

Large mechanical structures such as nuclear and steam power generation plants, aircraft, and chemical and petroleum refineries operate in critical environments; these include high energy, high temperature, high pressure, and highly corrosive environments. Therefore, small cracks and damage in such structures propagate easily, and sometimes result in accidents. The following cases describe safety accidents that caused loss of life, loss of property, and environmental damage.

Case I. Pipe Rupture Incident at Hamaoka Nuclear Power Station Unit-1, Japan [1].

The schematic diagram of RHR steam condensation lines and HPCI is illustrated in Fig. 1-2. While operating at rated power on November 7, 2001, a pipe rupture occurred in the steam condensation line (train B) of the residual heat removal (RHR) system at the Hamaoka Nuclear Power Station Unit-1 (hereafter, Hamaoka-1) operated by the Chubu Electric Power Company (hereafter, Chubu), resulting in steam with radioactivity released into the reactor building.

The unit started up on February 27, 2001 after the plant's 18th planned annual outage. During power operation before the incident, no abnormal indication was observed on major parameters such as generator output, neutron flux at average power range monitor, reactor pressure, reactor water level, main steam flow rate, feed-water flow rate, and radiation levels at stack monitors and monitoring posts. At 17:02 on November 7, 2001, a high pressure coolant injection (HPCI) surveillance test was carried out by manually actuating the HPCI turbine-driven pump while operating at rated power. This test procedure is specified in the safe operation rules (SORs) for the plant, which are similar to technical specifications in the U.S. When the valves were operated to increase the pump flow rate subsequent to pump actuation, the operating personnel heard a shock sound and the HPCI pump tripped on the "HPCI steam supply line high differential pressure" signal. Approximately 30 seconds later, two isolation valves (1MV-1301

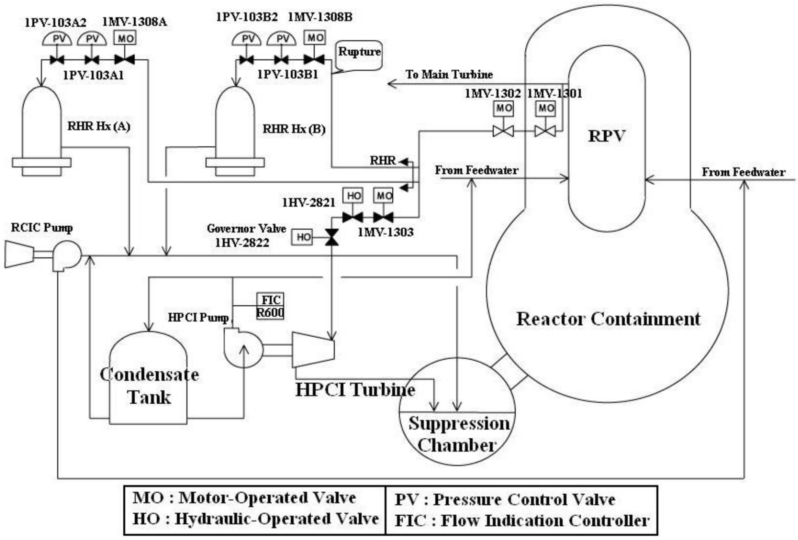

Fig. 1-1 Schematic diagram of RHR steam condensation lines and HPCI
(http://www.nisa.meti.go.jp/english/0207eng.pdf)

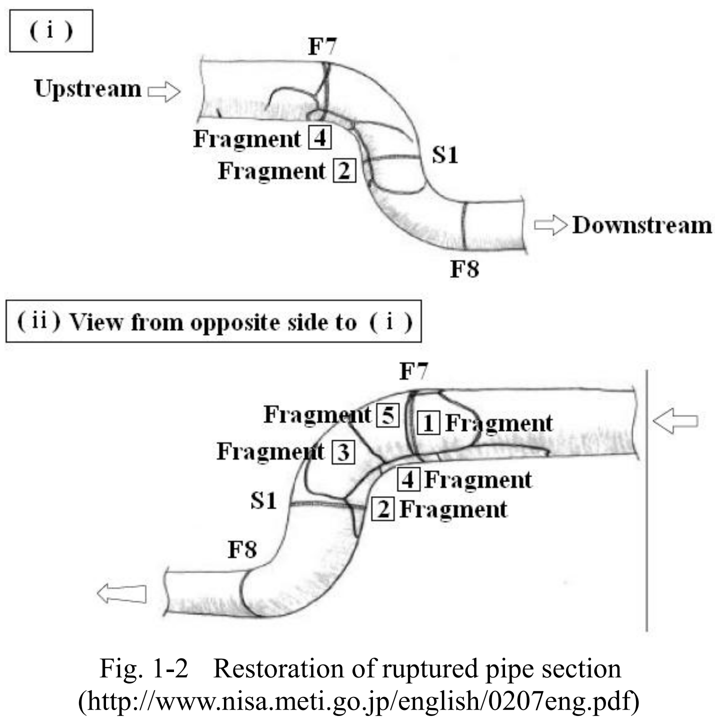

Fig. 1-2 Restoration of ruptured pipe section
(http://www.nisa.meti.go.jp/english/0207eng.pdf)

and 1MV-1302) automatically closed. The control room personnel received several alarms indicating the actuation of ten fire detectors in the reactor building, “high temperature on steam leakage detectors,” and “high-high radioactivity on reactor building ventilation monitors.” Based on the information on the HPCI pump trip and the related conditions, the general manager for power generation decided that the HPCI function could not be restored in the short time specified in the SORs, and declared a deviation from the operating limits and conditions (OL&C). The SORs state that a HPCI is allowed to be out of service for ten days. Consequently, power reduction was initiated at 18:20 and the reactor was manually shut down at 00:01 on November 8, 2001. During the power reduction, the maintenance personnel entered the room, where RHR heat exchanger B (RHR HX-B) was placed, and inspected the local conditions. As a result, at 19:05 on November 7, 2001, it was revealed that the pipe connected to RHR HX-B had ruptured at the elbow section. The steam condensation lines branch from the steam line to the HPCI turbine, and are made of carbon steel with a pipe diameter of 165 mm and a thickness of 11 mm. The Chubu measured the weight of ruptured pipe and restored the elbow by assembling the five fragments, as shown in Fig. 1-2.

The Nuclear and Industrial Safety Agency (NISA) and the Ministry of Economy, Trade and Industry (METI) reported that the reactor was manually shut down immediately after the pipe rupture, and that there was no radioactive release into the environment.

Case II. Boeing 747 SR-100, Japan Airlines Flight 123/Registration JA8119 (August 12, 1985) [2-3].

On August 12, 1985, the flight departed Tokyo bound for Osaka at about 18:10 local time. At 18:56, at an altitude of 5,000 feet of 340 knots, the airplane struck mountains forty-six minutes after takeoff from Tokyo and 32 minutes after a decompression event. 505 passengers and 15 crew members were killed. Four survivors were found near the tail section, which had broken away from the main wreckage field.

Much of the airplane's vertical tail and aft section were lost from the airplane following the decompression event. The accident was caused by deterioration of flying quality and loss of primary flight control functions due to a rupture of the airplane's aft pressure bulkhead and subsequent rupture of part of the fuselage tail, vertical fin, and all four hydraulic lines. This, in turn, resulted in the loss of all primary flight control functions. The empennage structure separated from the airplane as a result of the pressure bulkhead failure.

The aft pressure bulkhead ruptured because fatigue cracks propagating from the spliced section of the bulkhead's web weakened the bulkhead to the extent that it could no longer endure the in-flight cabin pressure. The initiation and propagation of the fatigue cracks were attributable to improper repairs of the bulkhead conducted in 1978. The fact that the fatigue cracks were not found in later maintenance inspections contributed to their continued propagation, leading to the rupture of the bulkhead.

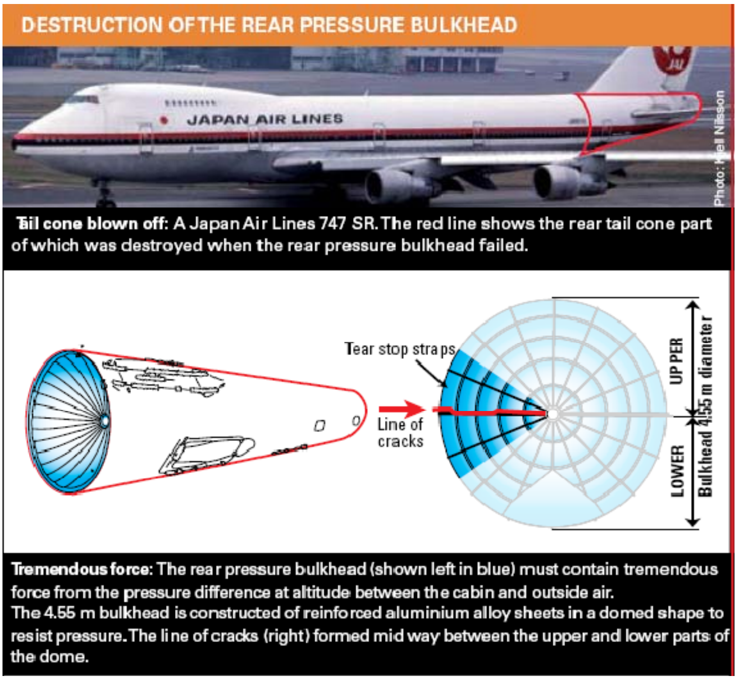

Fig. 1-3　Destructed position (http://www.casa.gov.au/fsa/2005/aug/28-33.pdf)

On June 2, 1978, during a landing incident at Osaka, the airplane experienced a tail strike. Several aft fuselage frames, the skin, and the aft pressure bulkhead were damaged as shown in Fig. 1-3. The airplane was repaired by a Boeing Airplane on-ground team contracted to perform damage repair. They replaced/repaired a major portion of the aft fuselage, replaced the lower half of the pressure bulkhead, and replaced the tail compartment pressure relief door.

Post-repair inspection showed inadequate edge margin on the newly-replaced lower half of the bulkhead. The solution for the inadequate edge margin involved installation of a splice plate to join the upper and lower halves of the bulkhead. The rework design called for a single splice plate to be used. However, the splice plate actually installed on the damaged airplane was cut into two pieces in order to "fit".

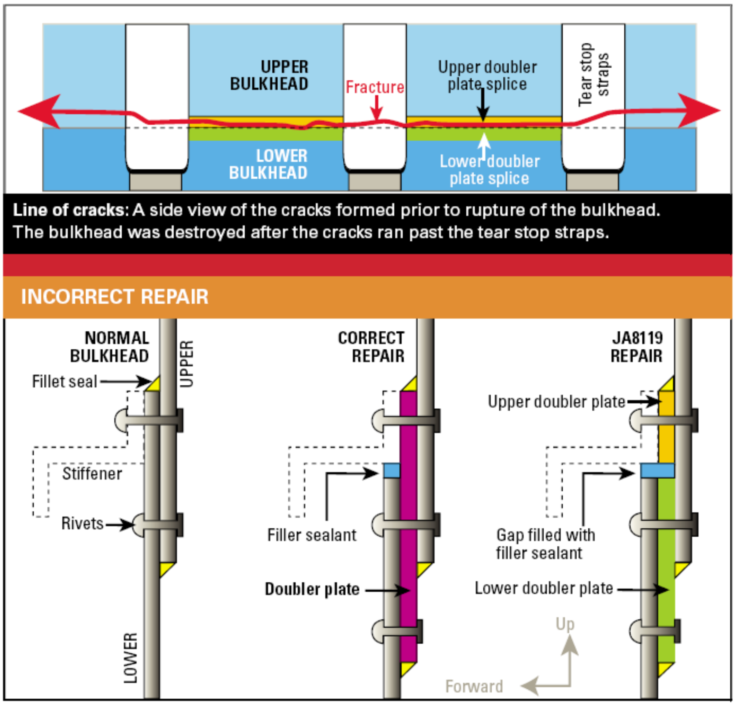

Fig. 1-4　Destructed position (http://www.casa.gov.au/fsa/2005/aug/28-33.pdf)

This resulted in a single row of rivets transferring the load to the upper affected web plate instead of two rows, as specified in the repair instruction drawing as shown in Fig. 1-4. This caused the bulkhead web to be improperly loaded and made it susceptible to early fatigue. Select here to see an animation of this effect. Furthermore, because of the geometry of the repair and the use of fillet sealant to fill the gap, the splice error could not be found through visual inspection. Correct and incorrect configurations would appear to be identical when viewed from either side. The accident board estimated that the strength of the repaired structure was reduced to about 70% of the strength that would have resulted from a proper repair.

Case III. Inter-City Express Accident, June 3, 1998 in Eschede, Germany [4-5].

The Eschede train disaster was the world's deadliest high-speed train accident as shown in Fig. 1-5. It occurred on June 3, 1998 near the village of Eschede in the Celle district of Lower Saxony, Germany. The toll of 101 dead and 88 injured surpassed the 1971 Dahlerau train disaster as the deadliest accident in the history of the Federal Republic of Germany

Inter-City-Express train-set 51 was traveling as ICE 884, "Wilhelm Conrad Röntgen," on the Munich to Hamburg route. After stopping in Hanover at 10:30 am, the train continued its journey northward. Six kilometers south of Eschede, near Celle, the rim of a wheel on the third axle of the first car broke, peeled away from the wheel, and punctured the floor of the car, where it remained embedded.

As the train passed over the first of two track switches, the embedded wheel rim slammed against the guide rail of the switch, pulling it from the railway ties. This steering rail also penetrated the floor of the car, becoming embedded in the vehicle and lifting the axle carriage off the rails. At 10:59, one of the now-derailed wheels struck the points lever of the second switch, changing its setting. The rear axles of car number 3 were switched onto a parallel track, and the entire car was thereby thrown into--and destroyed upon--the piers supporting a 300 metric ton roadway overpass.

Fig. 1-5　Eschede train disaster (http://en.wikipedia.org/wiki/File:Ice_eschede_1.jpg)

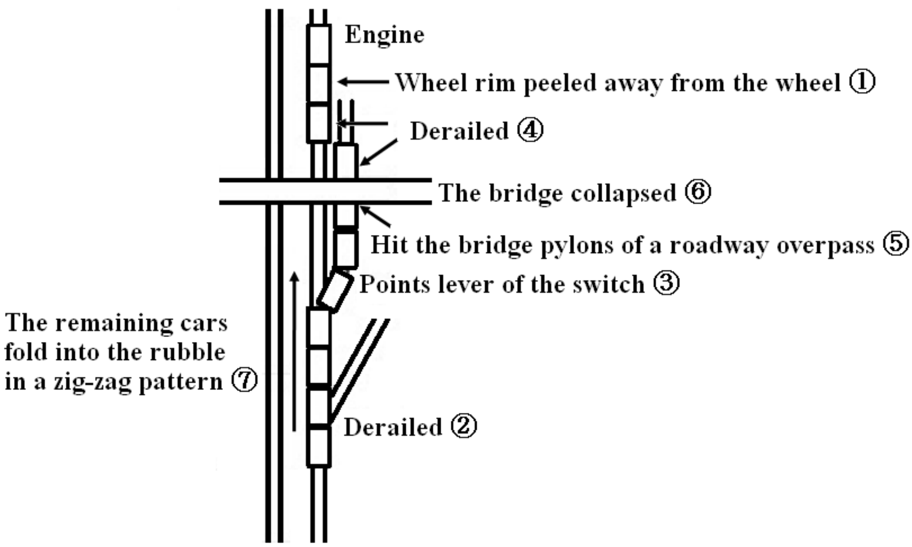

Fig. 1-6　Details of derailing accident
(http://shippai.jst.go.jp/en/Detail?fn=2&id=CA1000637)

The direct cause of the accident was a broken wheel rim that was lining a wheel on an axle of the first passenger car. In order to reduce costs and improve ride comfort, the ICE cars employed a wheel design that used a rubber damping ring between a metal wheel rim and the wheel body. The wheel rim failed due to metal fatigue as shown in Fig. 1-6. The second cause of the accident was an oversight by the maintenance crew. The derailed cars underwent periodic maintenance by a computer on the previous night. The Munich Maintenance Center examined the external diameter of each wheel and sleeve thickness using an acoustic sensor. While the permissible error was 0.6 mm, one of the wheels of the derailed cars had 1.1 mm of error. The maintenance crew did not replace or repair the wheels, assuming that the measured value would only affect ride comfort. The last cause was an insufficient failure detection system. The ICE train did not have a system installed to detect wheel failure and bring the train to an emergency stop.

To operate large structures with reliability, nondestructive testing (NDT) and quantitative evaluation techniques are very important in damage tolerance. Cracks must be found in each of several steps: production of the material, design, machining, manufacturing, and operation.

Cracks are initiated and propagated during production of raw material, or during operation at in critical environments. Each crack must be detected/repaired/replaced in a pre-service inspection (PSI) and in-service inspection (ISI), respectively. Electro-magnetic methods, magnetic particle testing (MT), magnetic flux leakage testing (MFLT), and eddy current testing (ECT) are useful in detecting surface cracks in both of PSI and ISI.

Magnetic particle testing uses electrical current to create a magnetic field within a specimen as shown in Fig. 1-7. Fine magnetic particles are flowed over the surface. The magnetic lines of flux, created by a discontinuity in the specimen, attract the particles presenting a visible indication that can be evaluated. Magnetic particle testing detects surface and subsurface discontinuities on all ferro-magnetic materials. It is simple to use and the equipment can be portable for use in the field. MT has been used in the NDT of turbine blades, diaphragms and rotor coupling surfaces. The length of a crack can be estimated. However, the depth and width of a crack is difficult to evaluate. Also, pre- and post-processing to is necessary to inspect a crack. And the magnetic particles are consumed continuously. And MT's use is limited to magnetic materials.

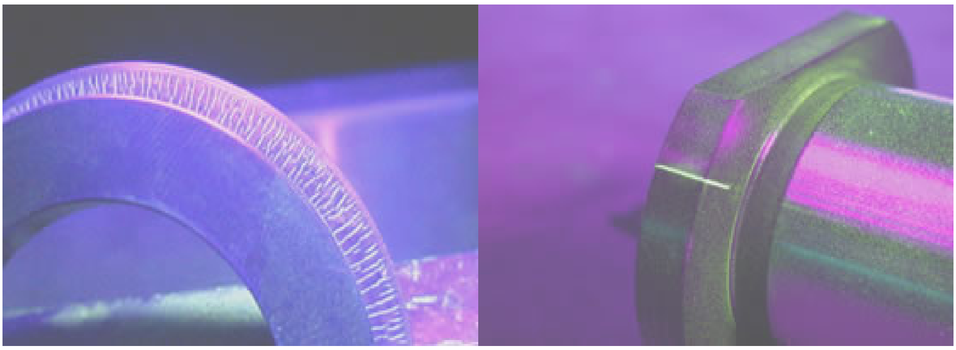

Fig. 1-7 Magnetic particle testing (http://www.lavender-ndt.co.uk/serv/training/mt.asp)

Magnetic flux leakage (MFL) is a magnetic method of nondestructive testing that is used to detect corrosion and pitting in steel structures, most commonly pipelines and storage tanks. The basic principle is that a powerful magnet is used to magnetize the steel. At areas where there is corrosion or missing metal, the magnetic field "leaks" from the steel. In an MFL tool, a magnetic detector is placed between the poles of the magnet to detect the leakage field. Analysts interpret the chart recording of the leakage field to identify damaged areas and hopefully to estimate the depth of metal loss as shown in Fig. 1-8. This article currently focuses mainly on the pipeline application of MFL, but links to tank floor examination are provided at the end. A crack can be evaluated using MFLT. The distribution of a magnetic field can be measured using a magnetic sensor. The existence, position, shape, and size of a crack can be estimated from the measured distribution of the magnetic field around a crack. However, scanning speed, spatial resolution, lift-off, and temperature dependency must be considered in NDT. In particular, cracks in paramagnetic materials or metals combined metal with ferromagnetic and paramagnetic materials are difficult to inspect.

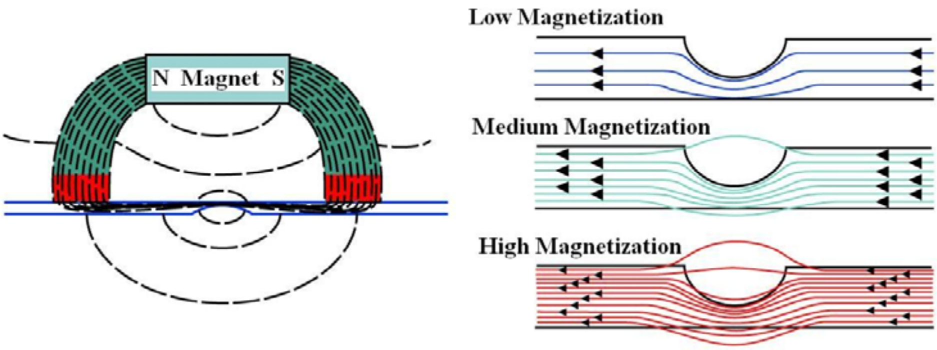

Fig. 1-8 Magnetic flux leakage
(http://www.battelle.org/pipetechnology/MFL/MFL98Main.html#Implementation)

Eddy Current Testing uses an electrical current in a coil to induce eddy currents into a specimen as shown in Fig. 1-9. Interference in the eddy current path results in an indication on the monitoring equipment. In ECT current is induced on the specimen, and an eddy current appears around a crack as shown in Fig. 1-9. Therefore, the impedance is different around a crack compared with a reliable area. However, scanning speed and spatial resolution have limitations. ECT sensors are difficult to array because of electric and magnetic interference and the limitations of eddy current testing include limited inspection depth and lack of a physical shape. Furthermore, cracks in Inconel, Onconel, STS304, 316, 430 and Zr-4 are difficult to inspect with ECT.

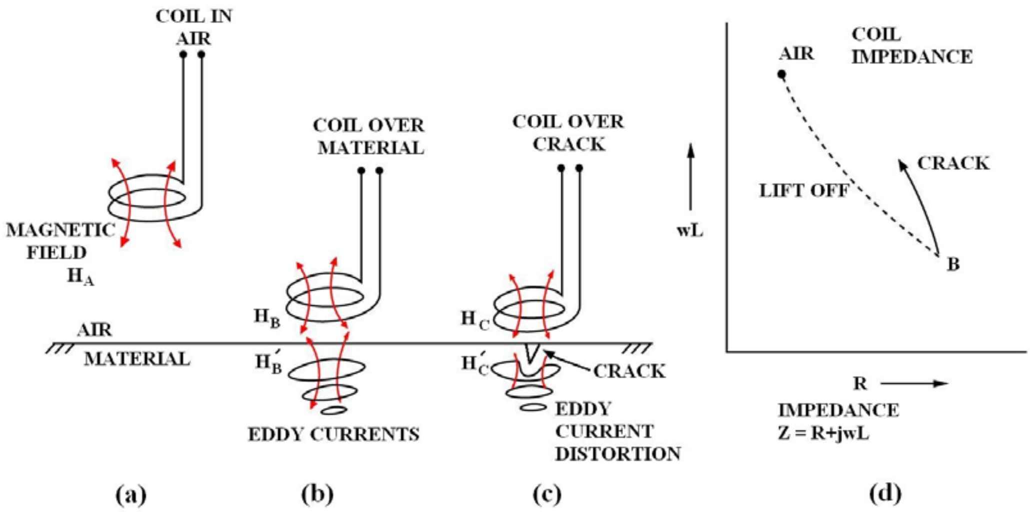

Fig. 1-9 Eddy current testing

Correspondingly, the improved NDT techniques, which (1) does not use a consumable material, such as magnetic particles, (2) require no pre- and post-processing before and after inspection of a crack, respectively, (3) use low power consumption, (4) can be estimated from the measured distribution of the magnetic field around a crack at the surface, sub-surface and far-side position, (5) can be measured distribution of the magnetic field in the ferro- and paramagnetic metal and combined structure, (6) can be measured distribution of the magnetic field with the large inspection area, (7) can be measured distribution of the magnetic field with high speed, and (8) can be measured distribution of the magnetic field with high spatial resolution, are necessary.

In particular, application, maintenance and expansion are necessary to protect home industries. The application is for setup the various ISI systems according to the kind of material, shape and structure of the specimen. The maintenance is for repairing quickly with low price. The expansion is for easy alteration without dependency of abroad. However, over 95% of NDT equipments are imported in our country. The technical level is under 50% compared with the advanced country.

The magnetic camera [9-25] is an approach, which can quantify the distribution of a magnetic field, and can reinforce the weaknesses of MT, MFLT, and ECT. During a doctoral program, the author developed (1) an alternative magnetic source; (2) a sensor array and signal processing circuit; (3) a quantitative nondestructive evaluation algorithm. Also, several applications using austenitic stainless steel, aluminum alloy, cold rolled steel, and nickel coated Inconel were examined, and the discrimination of a metallic coin was performed using a magnetic camera.

This thesis is organized follows 4. The first chapter is the introduction. Chapter 2 describes developed techniques and principles. Chapter 3 discusses applications, and Chapter 4 provides conclusions.

II. DEVELOPED TECHNOLOGIES

A. MAGNETIC CAMERA

A magnetic camera consists of a magnetic source, magnetic sensor array, magnetic lens, signal processing circuit, analog-to-digital converter (ADC), interface, computer and display, as shown in Fig. 2-1. The electro-magnetic field from a direct magnetic field [6, 8], alternating magnetic field, electrical field, induced current, sheet-type induced current [12], and terrestrial magnetism are applied to a specimen. The electro-magnetic field distorts according to the existence of the crack. The distortion affects the distribution of the magnetic field on the space. The distribution of the magnetic field is concentrated on the magnetic lens, [15] and changes with the distribution of electrical signals using a magnetic sensor array. After converting to digital signals using an ADC, the signals are stored in a computer, and finally displayed. Author's main works were developing of the magnetic source and the signal processing circuits in this thesis.

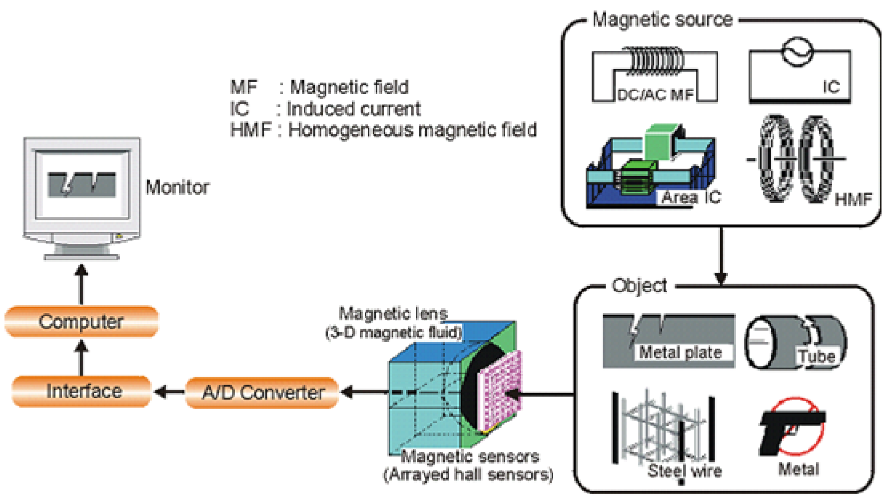

Fig. 2-1 Magnetic camera

B. Technologies for the Visualization of an Alternative Electro-Magnetic Field

1. *Hall Sensor and Signal Processing Circuit*

Hall sensors, magnetic resistance (MR) sensors, and giant magnetic resistance (GMR) sensors have been used as magnetic sensors to obtain the distribution of magnetic fields. A GMR sensor is an ultra-small magnetic sensor whose inventor won the Nobel prize for physics in 2007. GMR sensors have been used in NDT [8, 29]. The full-scale operational (FSO) range and the sensitivity of a Hall sensor with 59.2 dB are approximately $\pm$4 mT and 2.51 (V/mT), respectively. It has a 5~10 times greater FSO range and is 10~100 times sensitive than GMR or spin dependent tunneling (SDT) sensors. The standard deviation is about 0.01V, and with accuracy of 4 μT. Therefore, the Hall sensor is used in magnetic cameras. The distribution of a magnetic field using Hall sensors can be obtained using following three methods:

(1) Scanning using a sensor a 2-D space--single sensor scanning (SSS);

(2) scanning using a linearly-integrated Hall sensor array in 1-D space (LIHaS); and

(3) scanning using an area-type integrated Hall sensors array (AIHaS)

An SSS with 0.5 mm resolution, a LIHaS with 0.52 mm and 0.78 mm resolution, and an AIHaS with 0.78 mm and 3.5 mm resolution were developed during a doctoral program. Fig. 2-2(a) shows the distribution of residual magnetization around a clip using an AIHaS with 0.78 mm of resolution. Fig. 2-2(b) also shows the distribution of a magnetic field in a pipe using an AIHaS with 3.5 mm of resolution.

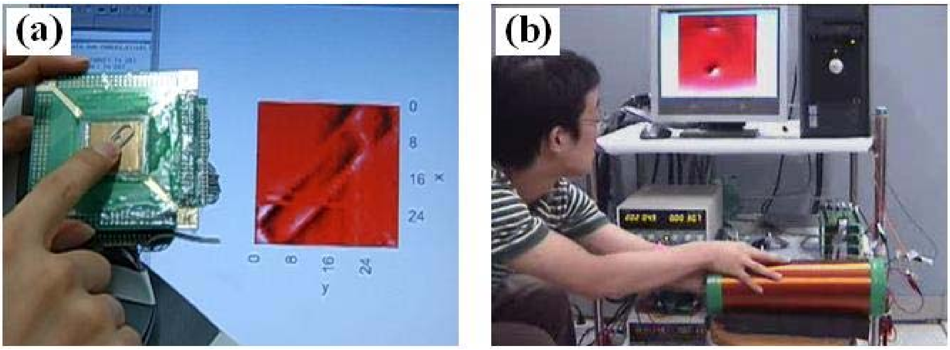

(a) Flat-type AIHaS with a high spatial resolution (b) Cylindrical-type AIHaS

Fig. 2-2 Area-type magnetic camera

A Hall sensor consists of four pins (two input lines and two output lines). The electrical field is supplied via the input lines; then the different of voltages between two output lines increases or decreases in proportion to direction and strength of the magnetic field, which applied to the vertical direction of the Hall sensor. Therefore, the differential amplifier is necessary in the operation of a Hall sensor. High pass filters are needed for separating the alternative signal from the direct magnetic field as shown in Fig. 2-3. Also, the low pass filters need for increasing the signal-to-noise ratio as shown in Fig. 2-4.

The amplitudes of alternative signals in the combined induced current and magnetic flux leakage (CIC-MFL), sheet type induced current (STIC) and improved STIC (i-STIC) are increase in proportion to crack size. Hall voltages have the same frequency as the alternative magnetic source, and amplitudes, which are proportional to the strength of the magnetic field. Moreover, a root mean square (RMS) circuit was used to obtain the amplitude of the Hall voltages in this paper. The distribution of a quantitative magnetic field at any frequency can be measured using the RMS circuit, digitized by ADC, and stored to memory.

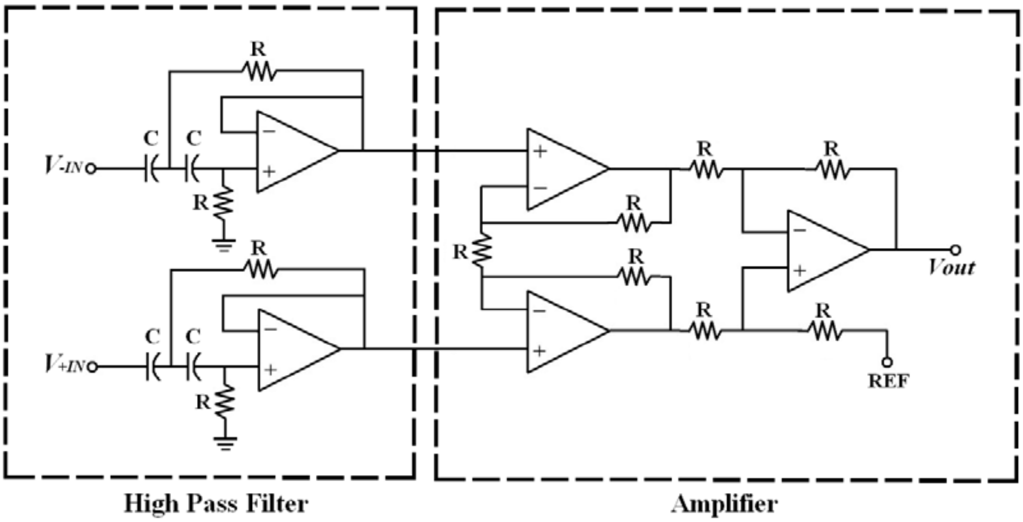

Fig. 2-3 High pass filter and a low noise operational amplifier construction for high precision measurement system.

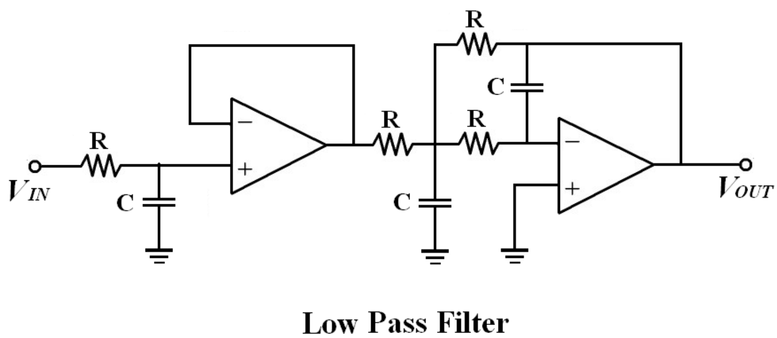

Fig. 2-4 3rd order Butterworth low pass filter

2. ***Magnetic Sources***

Several magnetic sources, such as cross-type magnetic source (C-MFL), direct current magnetic flux leakage (DC-MFL), plate-type magnetic flux leakage (P-MFL), in-side solenoid magnetic flux leakage (IS-MFL), vertical-type magnetic flux leakage (V-MFL), sheet-type magnetic induced current (STIC), improved sheet-type induced current (i-STIC), combined induced current-magnetic flux leakage (CIC-MFL), and magnetic fluid penetration testing (MFPT), have been developed according to the kind of material and the shape of the specimen. The characteristics of each magnetic source are indicated in Table 1.

The C-MFL method uses four cores. Each core is wound by the same number of coil turns, and the same currents are supplied to each coil by a direct current power supply. The specimen is magnetized, and a magnetic loop is produced when a pair of cores, which face each other, is magnetized. Also, the specimen is magnetized in the perpendicular direction when another perpendicular directional pair of cores is magnetized. The crack on the specimen can be detected using this configuration, regardless of the crack direction.

The DC-MFL method consists of two poles with a narrow distance, and is positioned on the bottom of a LIHaS. Cracks on the billet and train wheel are detected using DC-MFL. P-MFL and IS-MFL are used in the NDT of a pipe.

Table 1 The class of magnetic sources

<table>
<tr><th>Magnetic Source Type</th><th>Abbreviation</th><th>Specimen Material</th><th>Character</th><th>Application</th></tr>
<tr><td>Cross type magnetic flux leakage</td><td>C-MFL</td><td>Ferromagnetic</td><td>Crack inspection regardless of crack direction</td><td>ISI of streel and iron structure</td></tr>
<tr><td>Direct current magnetic flux leakage</td><td>DC-MFL</td><td>Ferromagnetic</td><td>Small size NDT system. Suitable in scan type mangetic camera</td><td>PSI in the steel-iron production line. ISI in train wheel</td></tr>
<tr><td>Plate type magnetic flux leakage</td><td>P-MFL</td><td>Ferromagnetic</td><td rowspan="2">NDT of pipe. Suitable in area type magnetic camera</td><td>ISI of steel structure. ISI of wire production</td></tr>
<tr><td>In-side solenoid magnetic flux leakage</td><td>IS-MFL</td><td>Ferromagnetic</td><td>ISI of steel pipe</td></tr>
<tr><td>Vertical type magnetic flux leakage</td><td>V-MFL</td><td rowspan="4">Ferromagnetic, Paramagnetic and Mixed ferromagnetic & paramagnetic</td><td rowspan="2">NDT of metal. Suitable both of scan- and area-type magentic camera.</td><td rowspan="2">ISI of aircraft and nuclear power plant</td></tr>
<tr><td>Sheet type induced current</td><td>STIC</td></tr>
<tr><td>Improved sheet type induced current</td><td>I-STIC</td><td>Suitable in scan type mangetic camera</td><td>ISI of aircraft and nuclear power plant</td></tr>
<tr><td>Combined induced current-magentic flux leakage</td><td>CIC-MFL</td><td>NDT of metal regardless of kinds. Suitable in scan-type magnetic camera</td><td>PSI in steel manufacturing line. ISI of aircraft and nuclear power plant</td></tr>
<tr><td>Magnetic fluid penetration testing</td><td>MFPT</td><td>All material</td><td>Opened surface crack</td><td>ISI of aircraft and nuclear power plant</td></tr>
</table>

a. **Vertical type magnetic field**

The V-MFL method uses a simple structure. The coils are wound with 10~20 turns. The magentic sensors are arrayed in the circular coils. The alternative magnetic field is induced in the vertical direction of the specimen. The alternative current is then induced in the specimen. Depending on the configuration of a crack, the induced current is distorted, and the distribution of the magneitc field is changed. The distribution has various values according to the crack's configuration and shape, and the size of the specimen.

b. **Sheet type induced current**

STIC is used to induce current in the specimen, as shown in Fig. 2-5. Alternating current (AC) input on the primary coil (Fig. 2-5(a)) generates an alternating magnetic flux in the core (Fig. 2-5(b)). At the same time, homogeneous current is induced in the copper sheet (Fig. 2-5(c)), which passes through the core. STIC is induced when the copper sheet is located on the surface of the specimen (Fig. 2-5(d)). Also, eddy current is generated due to the existence of the crack because the STIC on the specimen is distorted at both crack tips. Correspondingly, a magnetic field is generated around the crack, as shown in Fig. 2-5(e). The frequencies of each output of the Hall sensor coincide with the frequency of the input current of the primary coil. Also, the bias output is mixed with the alternative Hall voltage, because the specimen contains a partially-magnetized region in austenite stainless steel. The amplitude of the alternating Hall voltage can be converted to a direct response signal using a high-pass-filter (HPF) and the root-mean-squared (RMS) circuit ignoring the bias voltage.

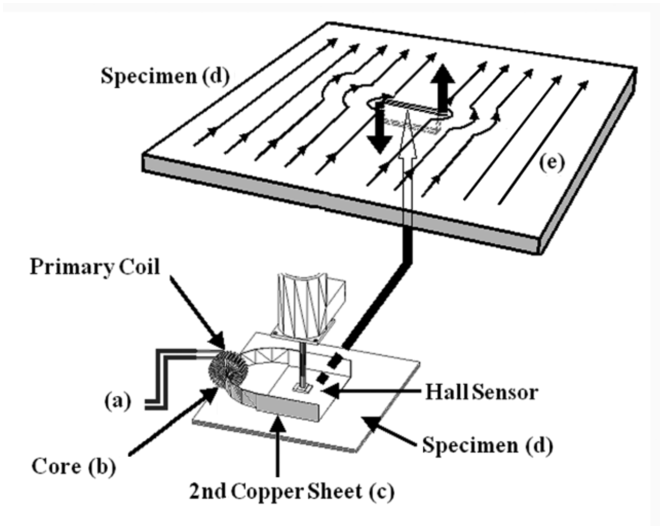

Fig. 2-5 Principles of sheet-type induced current

c. **Improved sheet type induced current**

The i-STIC is a kind of STIC, and is useful in a scan-type magnetic camera using LIHaS. A copper sheet is directly wound in the core, as shown in Fig. 2-6.

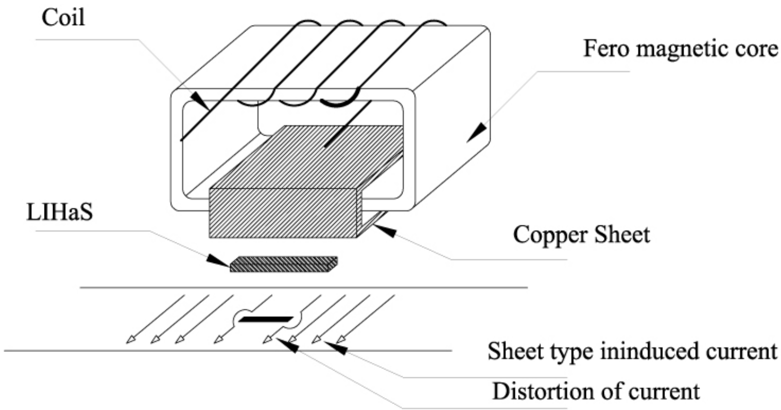

Fig. 2-6 Improved sheet-type induced current

d. Combined induced current – magnetic flux leakage

Fig. 2-7 shows a schematic of the small yoke-type magnetizer (hereafter yoke) and the numerical analysis results of the CIC-MFL method. The y-direction and x-direction represent the sensor array direction and scanning direction of the LIHaS, respectively. The z-direction indicates the vertical direction to the specimen plane. An assumed core, having a length of 40 mm in the y-direction, a width of 16 mm in the x-direction, a height of 27 mm in the z-direction, a thickness of 3.5 mm, a permeability of 250 (S/m), and a permittivity of 1.6×10^{-7} (F/m), is located on the back side of the LIHaS. The x-directional magnetic field occurs in the specimen as shown in Figs. 2-7(b) and 2-7(c), when an alternative current of 0.28A with 1 kHz is applied to the coil. The coil is wound on both sides of the core with a 16 mm height and 3 mm thickness. The specimen was assumed to be a ferromagnetic metal with dimensions 60 mm × 60 mm × 0.8 mm, and 250 (S/m) and 1.6×10^{-7} (F/m) of permeability and permittivity, respectively. The lift-off is 2 mm. The magnetic flux leakage has a maximum value when the length direction of a crack, with length of 10 mm, width of 1 mm, and depth of 0.8 mm, is vertical to the magnetizing direction (i.e., the x-direction) as shown in Fig. 2-7(b). Also, when the crack length direction is horizontal with the x-direction, the magnetic flux leakage is minimized as shown in Fig. 2-7(c). On the other hand, the induced current occurs in a vertical direction with the magnetizing direction, as shown in Figs. 2-7(d) and (e).

These induced currents are distorted around the tips of the crack, and a z-directional magnetic field is generated. The strength of the magnetic field due to the distortion of the induced current is maximized when the crack length direction is horizontal with the magnetization direction as shown in Fig. 2-7(e). Correspondingly, the crack can be detected independently with the length direction of the crack on a ferromagnetic metal, such as cold rolled steel, by using a small yoke-type alternative magnetizer. The author has called this improved magnetizing method the CIC-MFL method [9] because the induced current and magnetic field leakage can be used to detect a crack.

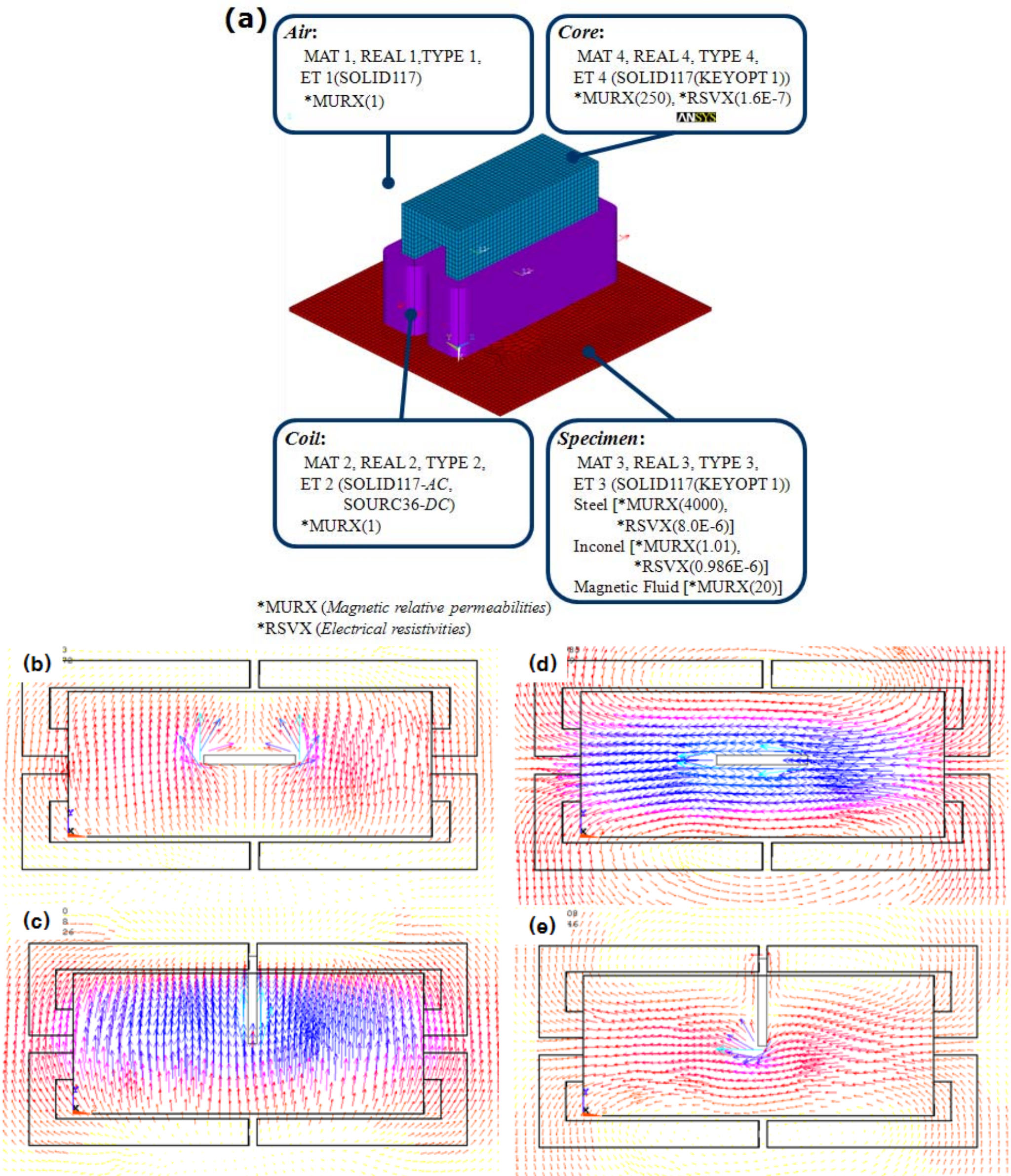

Fig. 2-7 Numerical analysis of the electro-magnetic field around each crack using a small yoke-type magnetizer operated by an alternative current of 1 kHz: (a) analysis model; (b) magnetic field on the y-directional crack; (c) magnetic field on the x-directional crack; (d) electric field on the y-directional crack; and (e) electric field on the x-directional crack

C. QUANTITATIVE ANALYSIS ALGORITHM

Fig. 2-9 shows an algorithm for crack evaluation. The spatial resolution of scanning, S, is determined according to the equipment shown in Fig. 2-8. In addition, the operator has to determine the detectable crack length, L, by using LIHaS. Next, the V_H, $\partial V_H/\partial x$ and $\partial V_H/\partial y$ images are obtained by using the scan-type magnetic camera. The length (L_c), angle (θ_{MAG}) between the magnetization direction and the crack length direction, and crack shape were estimated by using the $\partial V_H/\partial x$ and $\partial V_H/\partial y$ images. If L_c is larger than L, L_c/S is determined by using the $\partial V_H/\partial x$ image, or is assigned as 1 in other cases. The crack volume information $\partial V_H/\partial x|_{total}$ can be calculated by using Eq. (1) and (2). Therefore the crack shape, length, direction and volume can be evaluated by using the proposed algorithm and the LIHaS system.

$$\left.\frac{\partial V_H}{\partial x}\right|_{total} = \sum_{i=1}^{L_c/S}\left[Max\left(\frac{\partial V_{H,i}}{\partial x}\right) + Abs\left(Min\left(\frac{\partial V_{H,i}}{\partial x}\right)\right)\right] \qquad (1)$$

$$V_c = C_1 \cdot \left(\left.\frac{\partial V_H}{\partial x}\right|_{total}\right)^{C_2} \qquad (2)$$

where C_1 and C_2 are constants specified by the specimen material, the lift-off, the Hall coefficient, the Hall input current, the amplitude ratio, the magnetizer shape, and the magnetizing intensity.

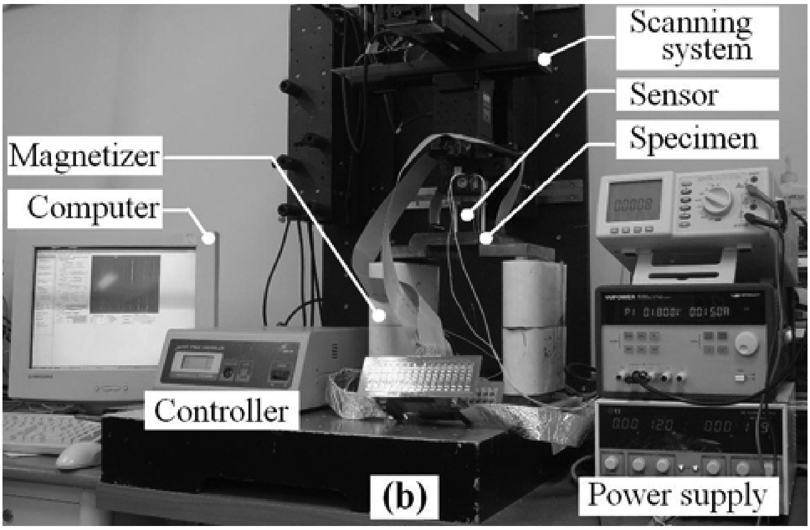

Fig. 2-8 Components of a scan-type magnetic camera with high precision scanning system.

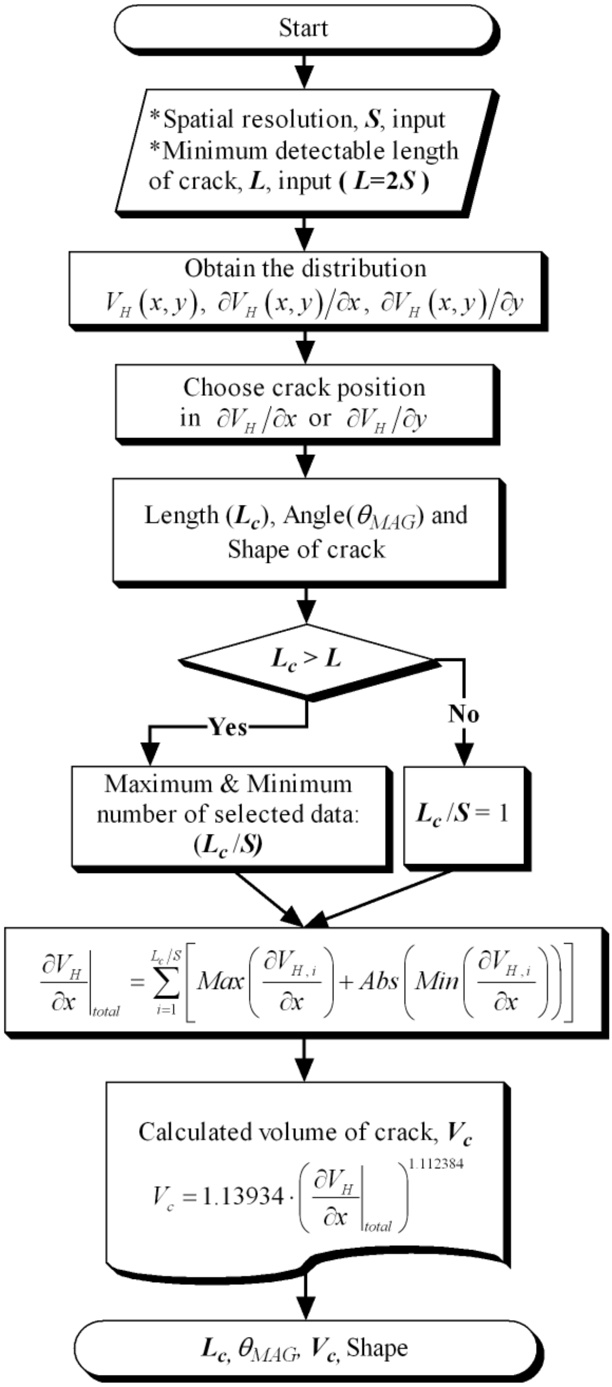

Fig. 2-9 Crack evaluation algorithm of the DC type magnetic camera.

$$\frac{\partial V_{RMS}}{\partial x}(x,y,z) \approx \frac{V_{RMS,Total}(x+\Delta x,y,z) - V_{RMS,Total}(x,y,z)}{\Delta x} \quad (3)$$

Here, L is the length of each crack obtainable from the distribution of $\partial V_{RMS}/\partial x$. Also, S is the scanning spatial resolution and is 0.5mm in this paper.

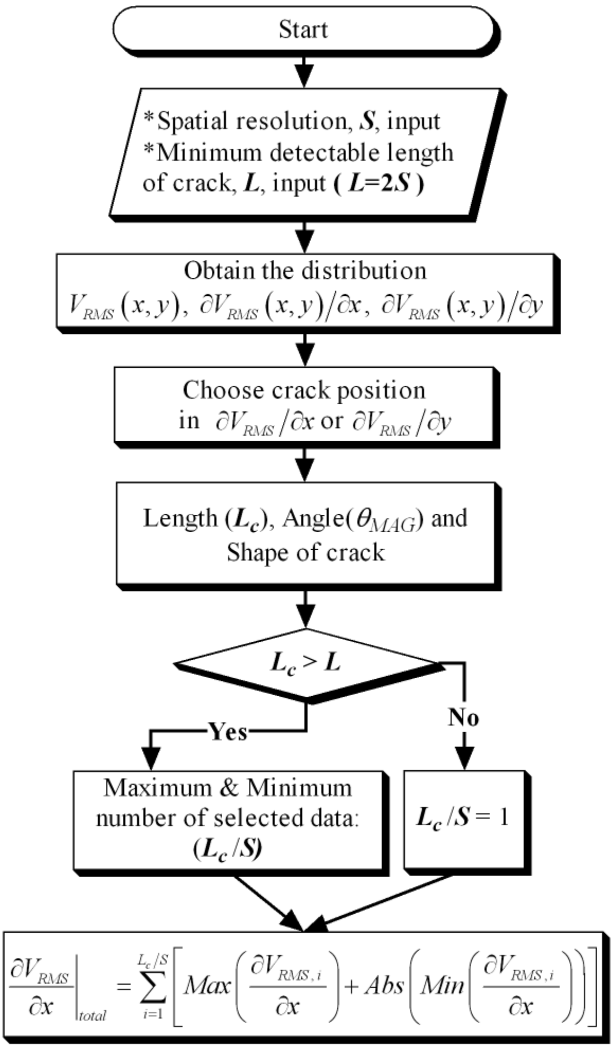

Fig. 2-10 Crack evaluation algorithm of the AC type magnetic camera.

This crack evaluation algorithm can be used in AC type magnetic camera as shown in Fig. 2-10. Eq. (3) shows an equation of the crack evaluation instead of Eq. (1). The $\partial V_H/\partial x|_{total}$ in DC type magnetic camera express as $\partial V_{RMS}/\partial x|_{total}$ in AC type magnetic camera. Also, C1 and C2 in Eq. (2) had different values , conductivity according to the permeability of material and frequency of AC source.

III. APPLICATIONS

A. NDT OF THE AUSTENITIC STAINLESS STEEL

Austenitic stainless steels (hereafter A-STS) such as SUS304 and SUS316 have been used in important mechanical structures with very large sizes, such as nuclear power plants, chemical plants, food industry facilities, and petrol storage tanks, because of their excellent anti-corrosive and heat resistant properties. The cracks on these mechanical structures have to be rapidly inspected and evaluated quantitatively in the damage tolerance engineering [40-41]. Usually, a nondestructive inspection method is correspondence with material properties. A-STS are paramagnetic metals where eddy current testing is useful. But, a small amount of partial magnetization is generated in A-STS because of their imperfect final heat treatments and mechanical processing such as rolling and welding. Correspondingly, the partially magnetized region (hereafter PMR) may be misrecognized as a crack when using previous types of nondestructive testing.

Conversely, the real time inspection of a crack in a large area (e.g., a circle area with a diameter of 75 mm) at a high spatial resolution is an advantage of MOI (magneto-optical/eddy current imaging) [35-36, 50]. MOI was developed for use in inspecting fatigue cracks and corrosion in aluminum alloys of aged aircraft. We induced a sheet type current on the specimen to generate a magnetic flux around a crack in the MOI. A sheet type induce current (STIC) is distorted when there is a crack. This distorted current induces a magnetic flux in a direction normal to the specimen. Therefore, the crack can be detected by using magnetic optical film (MO film) and a polarized optical system. However, the magnetic domains of the MO film of the MOI, having small saturated magnetization (H_S), are saturated partially on A-STS because of the external magnetic field (H_{EXT}) of the PMR exceeds H_S. Therefore, the surface cracks on partially magnetized A-STS are difficult to inspect by using MOI. Also, the shape and depth of the cracks are difficult to evaluate quantitatively because the distribution of the magnetic field cannot be obtained by MOI.

A magnetic camera using Hall sensors has been developed to inspect and evaluate cracks [14-16]. The distribution of the magnetic field can be measured quantitatively; then, the crack can be evaluated using a scan type magnetic camera [12]. On the other hand, a type of area magnetic camera using a Hall sensor array (HSA) has merit; that is, a crack can be detected with high speed without sensor scanning. However, the spatial resolution of a HSA is low so the detailed distribution of a magnetic field cannot be obtained. The detailed distribution of the magnetic field can be obtained by using single sensor scanning (hereafter SSS). But a large scanning time is necessary in SSS.

We propose high speed improved nondestructive testing and evaluating method. A STIC is induced on the A-STS, having a PMR and distortion around the tip of a crack. As a result, the alternating magnetic field, which is due to the crack existence, with a bias magnetic field due to the existence of the PMR, is produced. We propose a signal processing circuit for measuring the root-mean-square value (RMS) of the alternating magnetic field without the bias magnetic field. The distribution of the magnetic field with low spatial resolution can be visualized by using a HSA in real time. The detailed magnetic field distribution around a detected crack area is obtained by using SSS for evaluating the crack. Scanning time can be decreased because the scan area can be limited using this method. We evaluated the crack length, width, depth, section area, and volume by using experimentally obtained formulas.

A STIC is used to induce a current in a specimen as shown in Fig. 3-1. The alternating current (AC) input at 2.3 A and 6.4 kHz on the primary coil (Fig. 3-1(a)) generates an alternating magnetic flux in the core (Fig. 3-1(b)). At the same time, a homogeneous current is induced in the copper sheet (Fig. 3-1(c)), which passes through the core. A STIC is induced when the copper sheet is located on the surface of the specimen (Fig. 3-1(d)). Also, an eddy current is generated from the existence of a crack because the STIC on the specimen is distorted at both tips of the crack. Correspondingly, a magnetic field is generated around a crack as shown in Fig. 3-1(e).

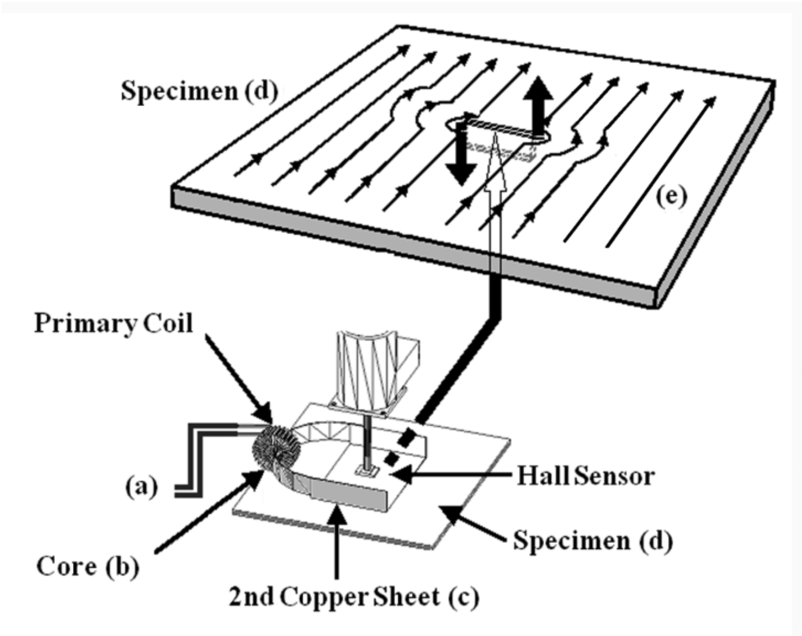

Fig. 3-1 Schematics of the sheet type induced current (STIC)

The frequencies of each output of the Hall sensor coincide with the frequency of the input current of the primary coil as shown in Fig. 3-2(a). Also, the bias output is mixed with the alternative Hall voltage, as shown in Fig. 3-2(b), because the specimen contains a PMR in the A-STS. The amplitude of the alternating Hall voltage (Fig. 3-2(c)) can be converted to the direct response signal (Fig. 3-2(d)) by using a high-pass-filter (HPF) and the root-mean-squared (RMS) circuit ignoring the bias voltage.

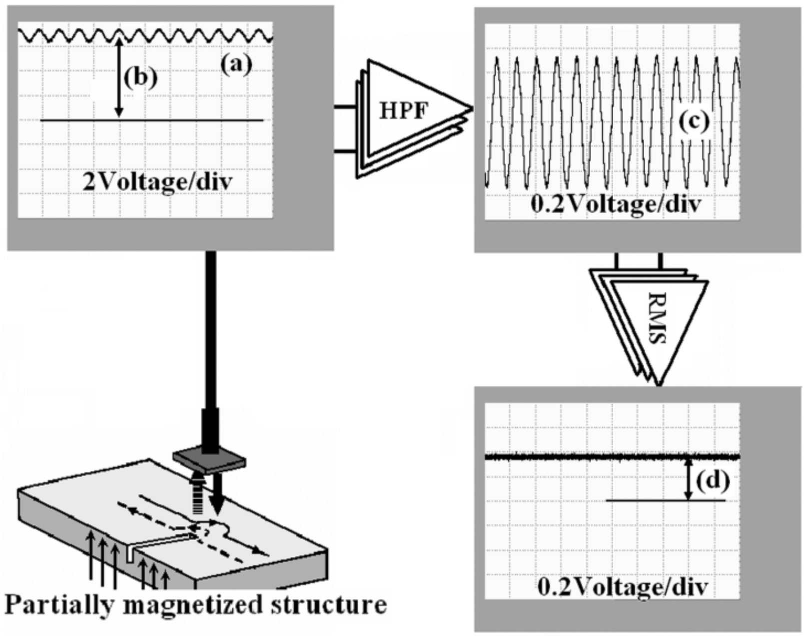

Fig. 3-2 Extraction of the amplitude of alternating current signal due to crack existence

1. *Specimen*

Cracks (9 slits) were introduced on partially magnetized A-STS, a SUS304 specimen, by using electronic discharge machining as shown in Fig. 3-3. Table 2 shows the dimensions of each crack. Fig. 3-4 shows a result of crack observation by using MOI. The crack was difficult to inspect by using MOI because of the PMR in the A-STS.

Table 2 Dimensions of each crack

Crack No	Depth[mm]	Width[mm]	Length [mm]
1	2	0.79	10
2	4	0.82	10
3	6	0.82	5
4	6	0.61	10
5	6	0.80	10
6	6	0.98	10
7	6	0.74	15
8	8	0.80	10
9	9	0.80	10

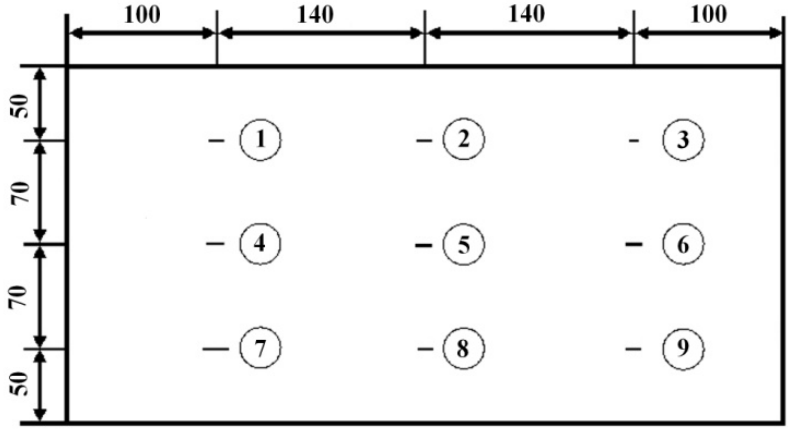

Fig. 3-3 Geometry of the investigated austenitic stainless steel specimen
(Unit: mm, thickness: 10mm)

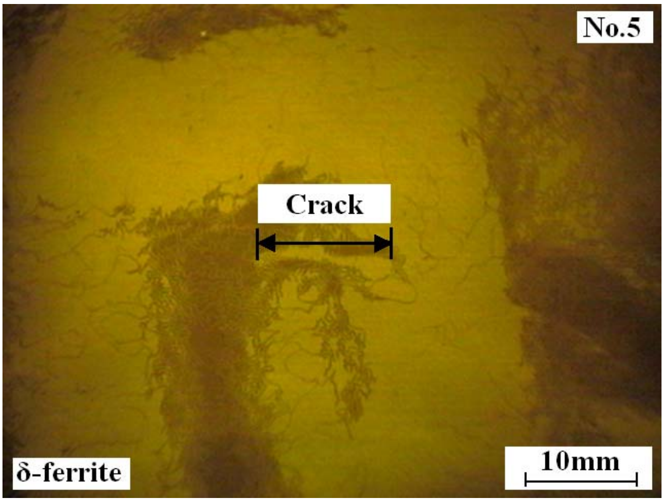

Fig. 3-4 Detection result of crack No.5 at 6.4 kHz by using MOI 308/3 (Produced by PRI)

The 64 Hall sensors of the HSA were arrayed in an 8 by 8 configuration of 3.5 mm spatial resolution as shown in Fig. 3-5. Therefore, the crack in the 28 mm by 28 mm area can be detected at the same time in this structure. The HSA was positioned on a copper sheet which induced STIC on a specimen. The AC input at 2.3 A and 6.4 kHz was derived from a function generator and amplified by an AC power amplifier. The AC input was applied to the primary coil and generated the STIC on the copper sheet. There were 45 and 46 turns of the primary coils in the HSA and SSS, respectively. Also, the thickness and the area of the copper sheet were 100 × 105 mm by 0.3 mm and 150 × 110 mm by 0.4 mm in the HSA and SSS, respectively. The copper sheet was positioned on the specimen. The lift-offs were 0.5 mm and 1 mm in the HSA and SSS, respectively.

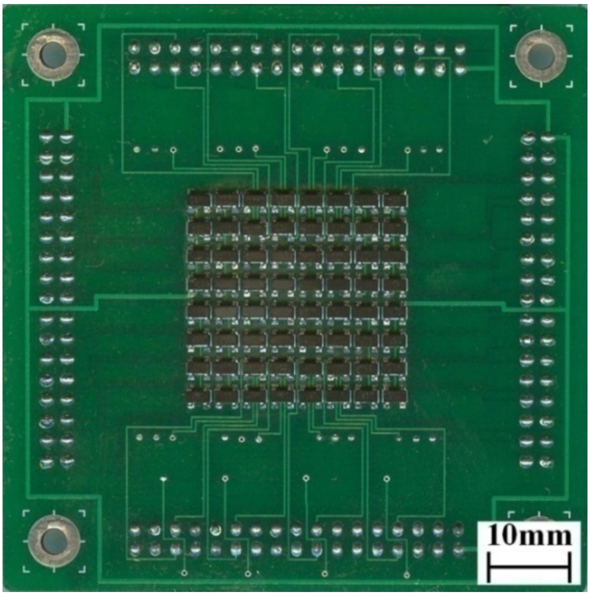

Fig. 3-5 Photograph of the Hall sensor array(HAS)

2. *Experiments*

a. Real time inspection of the crack by using a HSA

A HSA (Fig. 3-5) was used to confirm the real time inspection. The distribution of RMS Hall voltages, using a MX636JN RMS to DC converter, was obtained from a HSA of 3.5 mm spatial resolution (hereafter $DRMS_{LOW}$).

The $DRMS_{LOW}$ permitted crack detection of the partially magnetized specimen in real time. Two peak values from the $DRMS_{LOW}$ appeared at both tips of the crack, as shown in Fig. 3-6, because the STIC was distorted at the tips of the crack and the magnetic field was maximized at the same position. Also, the height of the peak was closely related to the crack size. However, the $DRMS_{LOW}$ was difficult to use in evaluating a crack because of its low spatial resolution.

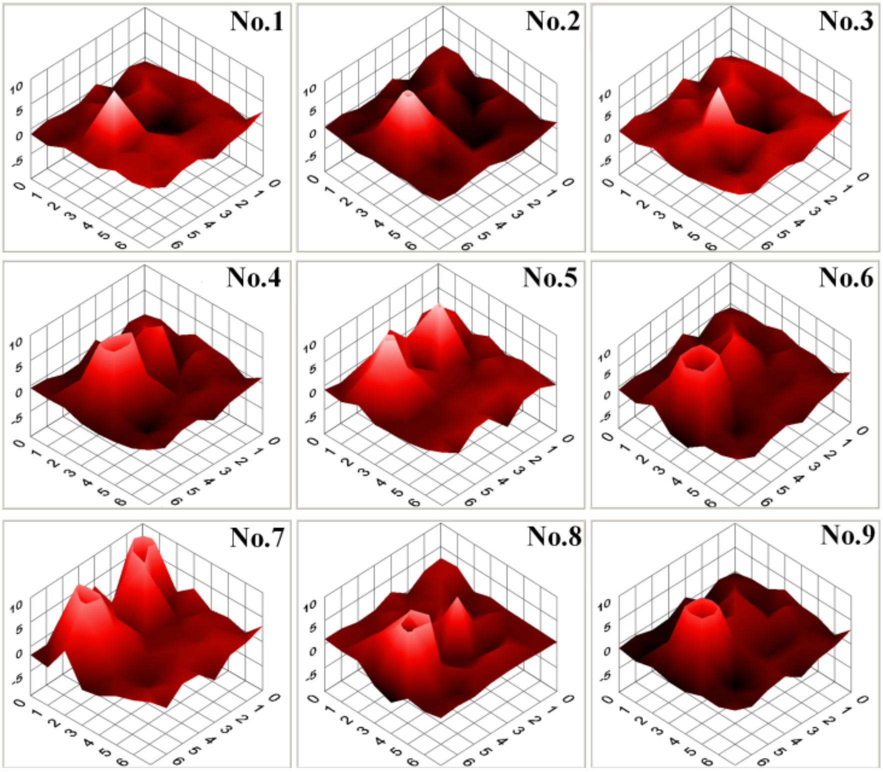

Fig. 3-6 Experimental results using HAS

b. **Evaluation of the crack using SSS**

The SSS could obtain the distribution of the RMS Hall voltage by using a MX636JN with a large spatial resolution of 0.5 mm (hereafter $DRMS_{HIGH}$). Fig. 3-7 shows the $DRMS_{HIGH}$ and its differential value in the STIC direction, $\partial (D_{HIGH})/\partial x$. The maximum value of the $DRMS_{HIGH}$ increased according to the depth of the crack (D_C) when the width (W_C) and length (L_C) of the crack were fixed as shown in Fig. 3-7, No.1, No.2, No.3, No.8, and No.9. These phenomena can be explained by the skin effect and with the help of the detailed Eq. (4). The density of the induced current on the subsurface J_t is defined in the following equation [37].

$$Jt = e^{-t/\delta} Js \tag{4}$$

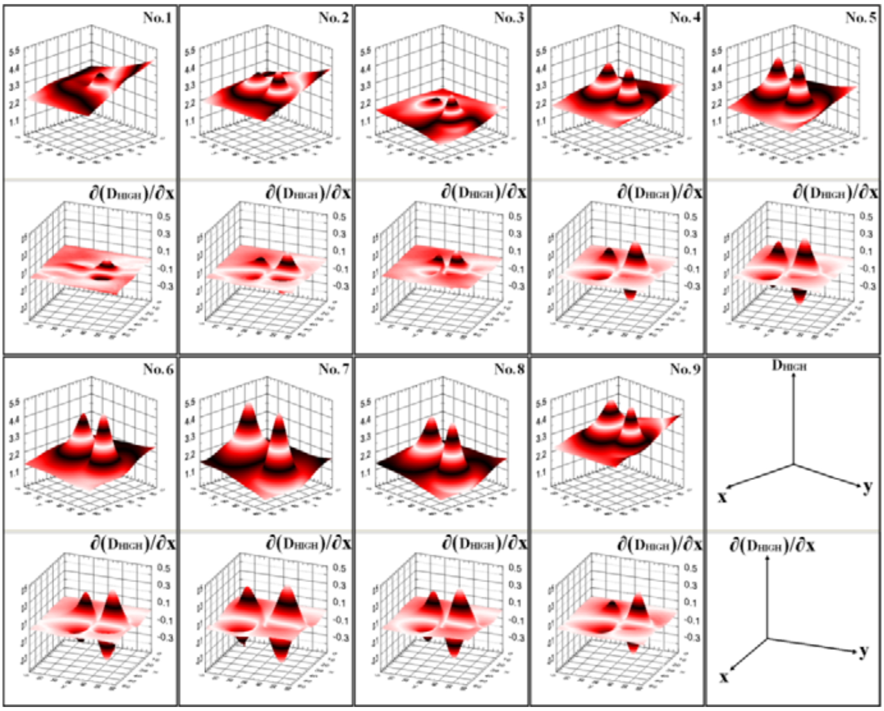

Fig. 3-7 Distributions of $DRMS_{HIGH}$ and $\partial D_{HIGH}/\partial x$ by using

Where, t and δ are the depth and skin depth, respectively. Js denotes the induced current on the surface. Here, the skin depth δ is defined as [38]:

$$\delta = \frac{1}{\sqrt{\pi f \mu \sigma}} \tag{5}$$

Where, f, μ and σ are frequency, permeability and electrical conductivity, respectively. According to specimen SUS 304, μ and σ are assumed as 1 and 2, respectively [39]. At a frequency of 6.4 kHz the skin depth is 5 mm. From Eq. (4), Jt / Js = 37 % if t is equal to δ in

5mm. For crack No.9, $t = 9$ mm, so $Jt / Js = 16.5$ %. So far, the deepest crack (9 mm) can be distinguished with other shallow cracks by this STIC experiment.

Fig. 3-8 shows the meaning of Max[$\partial(D_{HIGH})/\partial x$], Distance[$\partial(D_{HIGH})/\partial x$], and Diameter[$\partial(D_{HIGH})/\partial x$] in the $\partial(D_{HIGH})/\partial x$ distribution. The interval between the maximum position and the minimum position (hereafter, Diameter[$\partial(D_{HIGH})/\partial x$]) in $\partial(D_{HIGH})/\partial x$, which represented the gradient of each peak, was closely related to the crack parameter, D_C. Conversely, the distance between each set of maximum positions (hereafter Distance[$\partial(D_{HIGH})/\partial x$]) showed a close relationship with L_C, as shown in Fig. 3-7, No.3, No.5, and No.7.

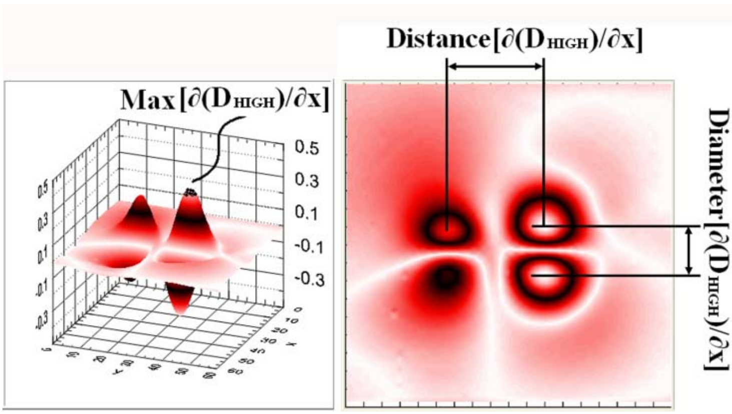

Fig. 3-8 Factors for evaluation of a crack

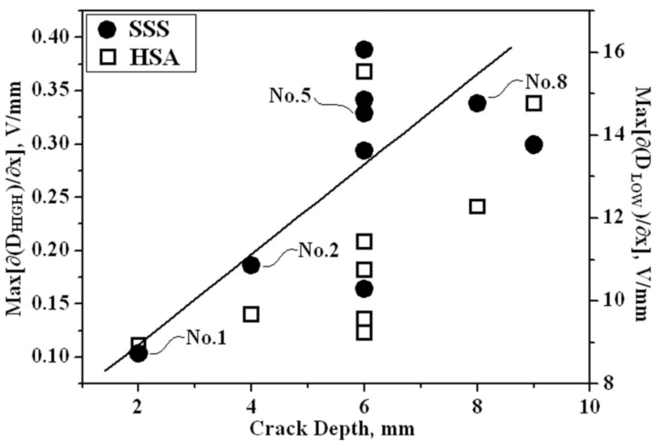

SSS
HSA
No.1
No.2
No.5
No.8
Max[∂(D_HIGH)/∂x], V/mm
Max[∂(D_LOW)/∂x], V/mm
Crack Depth, mm

(a)

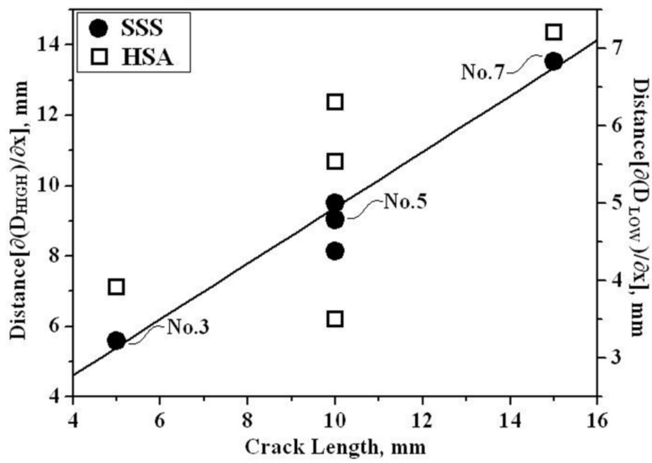

SSS
HSA
No.3
No.5
No.7
Distance[∂(D_HIGH)/∂x], mm
Distance[∂(D_LOW)/∂x], mm
Crack Length, mm

(b)

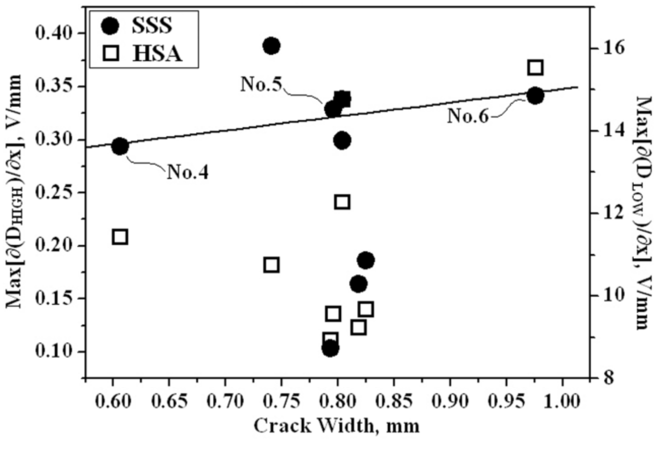

SSS
HSA
No.4
No.5
No.6
Max[∂(D_HIGH)/∂x], V/mm
Max[∂(D_LOW)/∂x], V/mm
Crack Width, mm

(c)

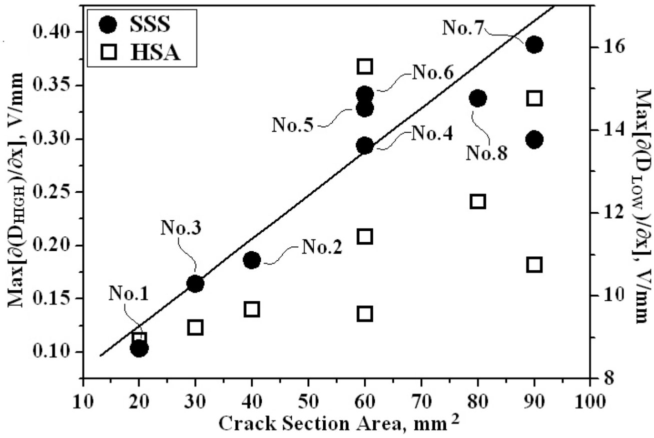

(d)

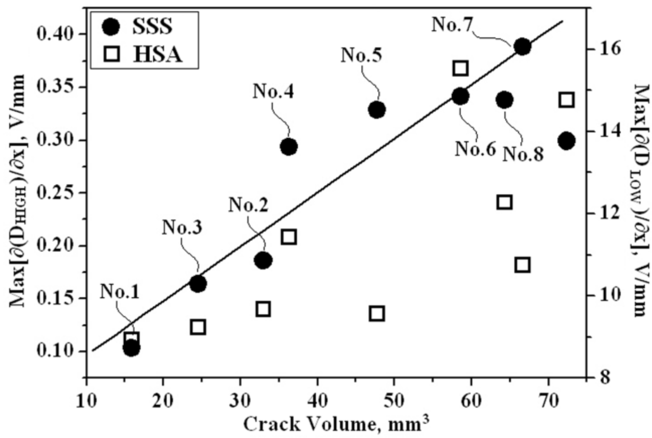

(e)

Fig. 3-9 Relationship between the NDE factors and the crack parameters (D_C, L_C and W_C)

Fig. 3-9 shows the relationship between Max[$\partial(D_{HIGH})/\partial x$], Distance[$\partial(D_{HIGH})/\partial x$], and the crack parameters (D_C, L_C, and W_C). The Max[$\partial(D_{HIGH})/\partial x$] showed a close relationship with D_C as shown in Eq. (6), which was derived from cracks No.1, No.2, No.5, and No.8 in Fig. 3-9(a) when the W_C and L_C were fixed.

$$Dc = 23.6574 \times Max\left[\partial(D_{HIGH})/\partial x\right] - 0.02765 \tag{6}$$

Also, the Distance[$\partial(D_{HIGH})/\partial x$] showed a close relationship with the L_C as shown in Eq. (7), which was derived from cracks No.3, No.5, and No.7 in Fig. 3-9(b).

$$Lc = 1.25837 \times Distance\left[\partial(D_{HIGH})/\partial x\right] - 1.89301 \tag{7}$$

Furthermore, the Max[$\partial(D_{HIGH})/\partial x$] showed a close relationship W_C by cracks No.4, No.5 and No.6 in Fig. 3-9(c).

$$Wc = 8.31739 \times Max\left[\partial(D_{HIGH})/\partial x\right] - 1.97097 \tag{8}$$

In addition, the section area, S_C, and the volume of the crack, V_C, can be calculated by using Eq. (9) and Eq. (10), derived from Figs. 3-9(d) and (e), respectively.

$$Sc = 244.49878 \times Max\left[\partial(D_{HIGH})/\partial x\right] - 10.53301 \tag{9}$$

$$Vc = 194.9318 \times Max\left[\partial(D_{HIGH})/\partial x\right] - 8.88109 \tag{10}$$

The L_C Eq. (7) showed less error than the W_C and D_C equations. Also, the section area Eq. (9) was derived from Fig. 3-9(d), showed a small error. Correspondingly, D_C' can be calculated from S_C by using Eq. (11) because the section area is multiplied by L_C and D_C'.

$$Dc' = Sc/Lc = \frac{\{244.49878 \times Max\left[\partial(D_{HIGH})/\partial x\right] - 10.53301\}}{\{1.25837 \times Distance\left[\partial(D_{HIGH})/\partial x\right] - 1.89301\}} \tag{11}$$

We calculated the depth of the crack with extreme accuracy by using Eq. (11) and compared it with Eq. (6) as shown in Fig. 3-10.

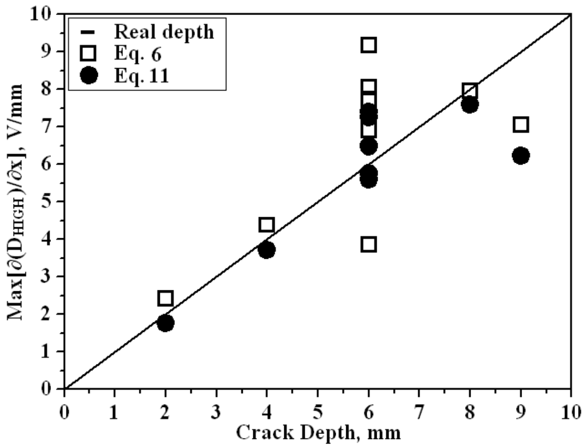

Fig. 3-10 Comparison of calculated crack depths by using Eq. (6) and Eq. (11)

The Max[$\partial(D_{HIGH})/\partial x$] included relevant information on the depth, width and length of the crack. Also, the changes of depth and length affected more easily than that of the width. Fortunately, the length of the crack, L_C, could also be calculated by using Distance[$\partial(D_{HIGH})/\partial x$] with less error than W_C. Correspondingly, the calculated volume of the crack, obtained by multiplying L_C (Eq. (7)), W_C (Eq. (8)), and D_C' (Eq. (11)), as shown in Eq. (12). We expect this calculation to have less error.

$$
\begin{aligned}
&Volume = Lc \times Wc \times Dc' \\
&= \{1.25837 \times Distance\left[\partial(D_{HIGH})/\partial x\right] - 1.89301\} \\
&\times \{8.31739 \times Max\left[\partial(D_{HIGH})/\partial x\right] - 1.97097\} \\
&\times \frac{\{244.49878 \times Max\left[\partial(D_{HIGH})/\partial x\right] - 10.53301\}}{\{1.25837 \times Distance\left[\partial(D_{HIGH})/\partial x\right] - 1.89301\}}
\end{aligned} \qquad (12)
$$

However, the calculated volume using Eq. (12), with a bigger error than Eq. (10) at the 72 mm^3 of volume, was obtained as shown in Fig. 3-11. The bigger errors resulted from the accumulation of errors in Eq. (7), Eq. (8), and Eq. (11).

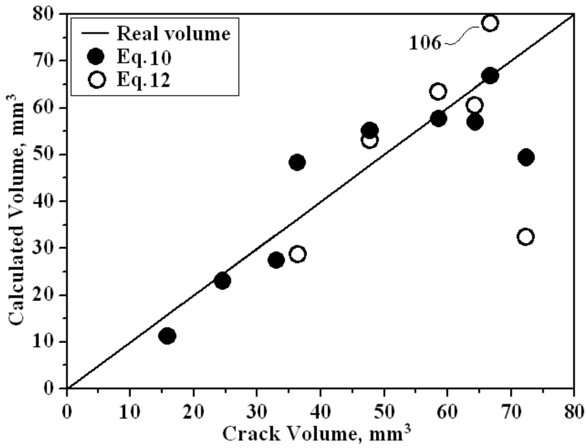

Fig. 3-11 Comparison of calculated crack volumes by using Eq. (10), Eq. (12) and Max[$\partial(D_{LOW})/\partial x$]

3. *Discussions*

We proposed a nondestructive evaluation method for cracks occurring on the surface of austenitic stainless steel with a partially magnetized area in real time. The crack was inspected in real time by using a Hall sensor array and a sheet type induced current. And the distribution of the magnetic field ($DRMS_{HIGH}$), the differential value of $DRMS_{HIGH}$ ($\partial(D_{HIGH})/\partial x$), the maximum value of $\partial(D_{HIGH})/\partial x$ (Max[$\partial(D_{HIGH})/\partial x$]), the interval between the maximum position and minimum position in the $\partial(D_{HIGH})/\partial x$ (Diameter[$\partial(D_{HIGH})/\partial x$]), and the distance between each set of maximum positions (Distance[$\partial(D_{HIGH})/\partial x$] were obtained by using single sensor scanning at the inspected crack area.

The depth, width, length, section area, and volume of the crack, can be calculated by equations derived from the relationship between the Max[$\partial(D_{HIGH})/\partial x$], Distance[$\partial(D_{HIGH})/\partial x$], Diameter[$\partial(D_{HIGH})/\partial x$], and the crack morphologies.

B. NDT OF THE ALUMINUM ALLOY

According to aircraft accident statistics [40], aircraft fatigue is responsible for 60 to 80% of all accidents. Despite these statistics, aircrafts are permitted to operate with cracks and damage that are smaller than damage tolerance sizes [40-41]. Therefore, crack inspection and evaluation techniques are important for damage tolerance engineering. Electromagnetic nondestructive techniques are especially useful for inspection and evaluation of cracks on the surface of a specimen [42-43]. Paramagnetic metals like aluminum alloys are used in aircraft due to their light weight. Magneto-optical eddy current imager (MOI) is a nondestructive magneto-optical technique that is used to inspect fatigue cracks and corrosion in the aluminum alloy of aged aircraft [16, 36]. Unfortunately, the quantitative distribution of distorted magnetic flux leakage (MFL) from crack tips is difficult to measure, and therefore, the shapes and sizes of cracks are difficult to evaluate quantitatively. Additionally, the inspected results vary significantly according to the skill level of the worker. Single Hall sensor scanning for crack inspection in paramagnetic materials (SSS) is developed by Jun, et al. [42-43]. Distorted alternate currents (DAC) are produced around the crack tips when the sheet type induced current (STIC) is induced on the specimen in the SSS system. The alternate MFL resulting from the DAC is detected using a Hall sensor. The RMS of the MFL obtained by using high pass filters after the use of the Hall sensor is converted to a digital signal by an analog-to-digital converter (ADC), stored in a computer, and processed by interface and operation software [44]. An algorithm for the quantitative nondestructive testing and evaluation of cracks of different shapes and sizes on the aluminum alloy, Al7075, is proposed in this chapter. The induced current and eddy current, which are magnetic sources, allow the detection of cracks in paramagnetic materials. A high precision 3-dimensional movement system moves the Hall sensor to scan the magnetic field.

1. ***Specimen***

Fig. 3-12 and Table 3 show the aluminum alloy (Al7075, 250 × 250 × 6.6 mm) specimen with a crack at its center used to investigate the relationship between the RMS of MFL and crack information. The volume and section area of a crack and the angle between the surface of the specimen and the edge of the crack tip in the direction of depth (θ_{TIP}) are evaluated as crack information.

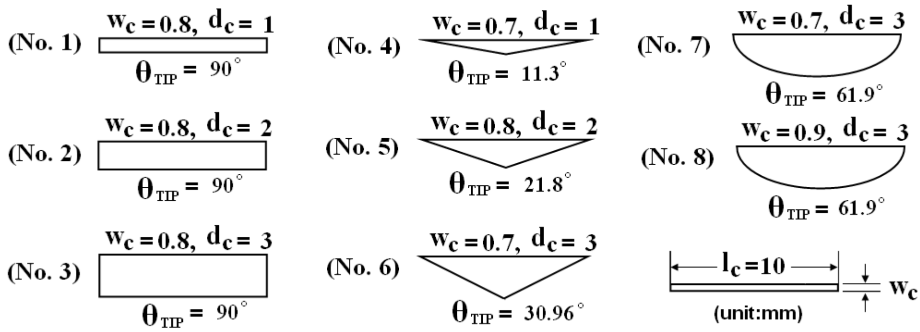

Fig. 3-12 Shapes of crack on each specimen.

Table 3 Aluminum alloy Al7075 specimens of several shapes and crack sizes

Crack No	Shape	Width [mm]	Depth [mm]	Length [mm]	Section area[mm^2]	Crack volume[mm^3]	Crack angle[deg]
1	Rectangle	0.8	1.0	10	10	8	90°
2	Rectangle	0.8	2.0	10	20	16	90°
3	Rectangle	0.8	3.0	10	30	24	90°
4	Triangle	0.7	1.0	10	5	3.5	11.3°
5	Triangle	0.8	2.0	10	10	7	21.8°
6	Triangle	0.7	3.0	10	15	12	30.96°
7	Circular Arc	0.7	3.0	10	23.57	16.5	61.9°
8	Circular Arc	0.9	3.0	10	23.57	21.0	61.9°

2. ***Experiments***

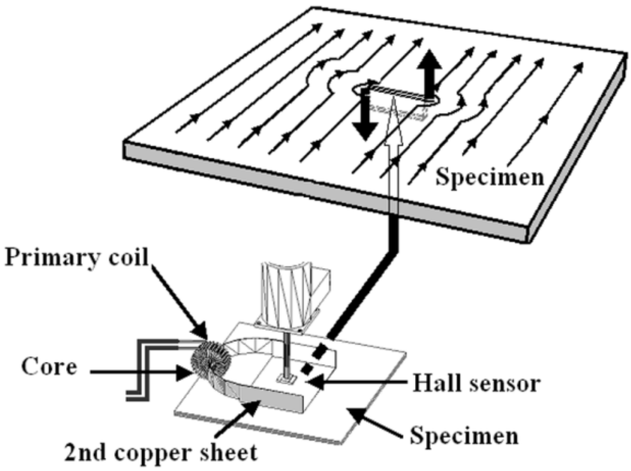

Fig. 3-13 Schematics of the transformer to induce the sheet type current on a specimen and the 3-dimensional scanning equipment.

A current transformer is used to induce the STIC on a specimen [35-36, 42-43, 45, 50,]. The transformer consists of a ferromagnetic core, a primary coil wounded around the core, and a copper film 112 mm in width, as shown in Fig. 3-13. The toroidal ferromagnetic iron core, which has internal and external diameters of 24 mm and 47 mm respectively, is used as the transformer. The primary coil is wound 46 times on the core. Also, the input current is a sinusoidal wave of 2 A. The width, total length, effective length of the specimen, and thickness of the copper film are 112 mm, 610 mm, 155 mm, and 0.3 mm respectively.

The distribution of the RMS of the MFL is measured by using a SSS system when STICs of 3.2 kHz and 25.6 kHz are induced on each specimen of Table 3. Fig. 3-14 and Fig. 3-15 show the distributions of the RMS Hall voltages (V_{RMS}) on each specimen, for STICs of 3.2 kHz and 25.6 kHz respectively. Two peaks in each V_{RMS} distribution appear around the tips of crack because the induced current on the specimen is distorted around each tip. Therefore, the lengthwise direction of the crack can be determined from the line connecting the peaks. Increases in crack depth influence the increase of the peak V_{RMS} values at 3.2 kHz of STIC, as shown in Fig. 3-14. This phenomenon shows that the STIC is induced on the surface and subsurface of the specimen. Correspondingly, the average of several maximum values on the distribution of V_{RMS} at 3.2 kHz of STIC (AvrMax[$V_{RMS}^{3.2}$]) include information about the crack depth. Also, the V_{RMS} and the distance between peaks, $\Delta l_C^{3.2}$, show rectangular cracks (No. 1, 2, 3) are larger than triangular (No. 4, 5, 6) or circular arc-shaped cracks (No. 7, 8).

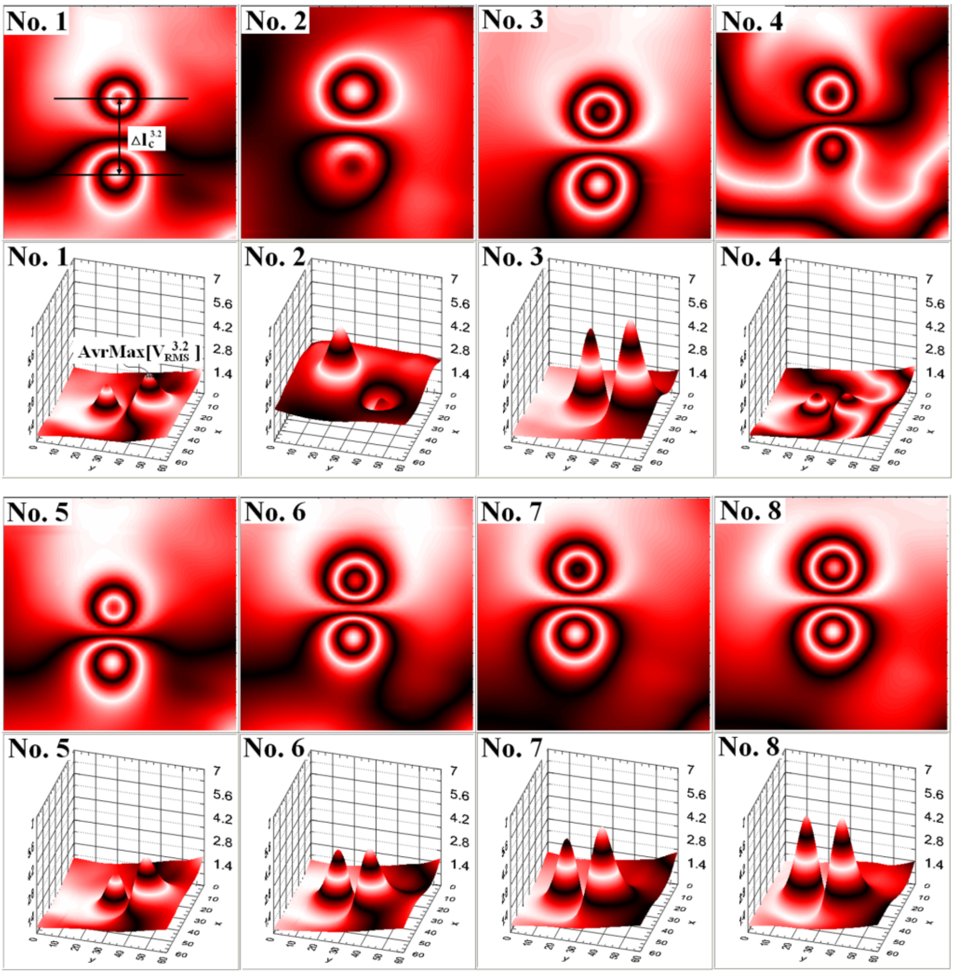

Fig. 3-14 Distributions of the root mean squared value (V_{RMS}) at 3.2 kHz on each crack.

Fig. 3-15 shows the V_{RMS} distribution at 25.6 kHz of STIC. These V_{RMS} distributions are smaller than those at 3.2 kHz, because the STIC is induced near the specimen surface under a high frequency environment. The V_{RMS} and the $\Delta l_C^{25.6}$ show larger values for rectangular cracks (No.1, 2, 3) compared to triangular cracks (No. 4, 5, 6) and circular arcs (No. 7, 8), similar to results shown in Fig. 3-15. Therefore, crack depth information is included in the AvrMax[$V_{RMS}^{25.6}$].

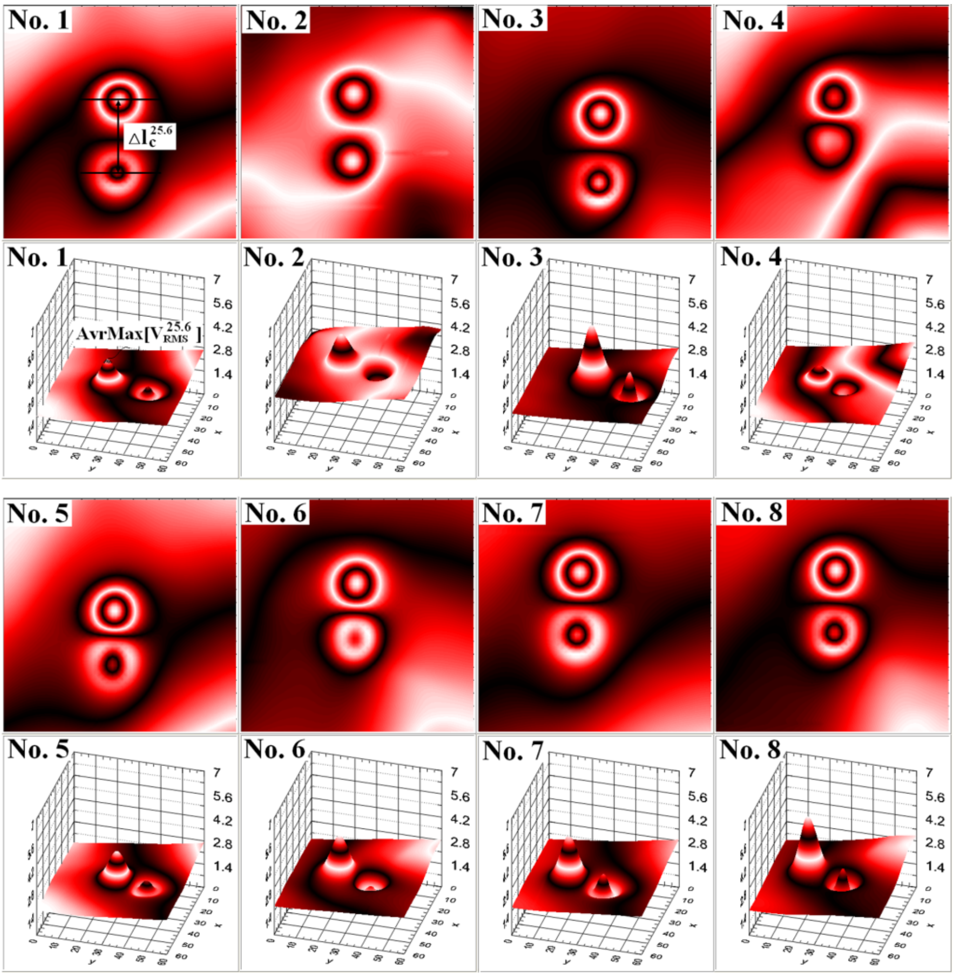

Fig. 3-15 Distributions of the root mean squared value (V_{RMS}) at 25.6 kHz on each crack.

The center positions of the $V_{RMS}{}^{3.2}$ and $V_{RMS}{}^{25.6}$ appear at a location where the STIC is distorted, that is, around crack tips. Therefore, $\Delta l_C{}^{3.2}$ and $\Delta l_C{}^{25.6}$ are approximately the same as the length of the crack in the case of 90° of θ_{TIP} (No. 1, 2, 3). When the θ_{TIP} is smaller than 90° (No. 4, 5, 6, 7, 8), the $\Delta l_C{}^{3.2}$ and $\Delta l_C{}^{25.6}$ decrease as shown in Fig. 3-16. Further, the $\Delta l_C{}^{25.6}$ is usually smaller than the $\Delta l_C{}^{3.2}$. These phenomena are explained by the skin effect. The density of the induced current on the surface and in the subsurface at depth t, J_s and J_t respectively, is expressed by following Eq. (4) at chapter B. Here, δ is the skin depth, which is expressed as following Eq. (5) at chapter B. Also, f, μ and σ are the frequency of induced current, permeability, and conductivity of the metal respectively. According to Eq. (4), if the depth t coincides with δ, than J_t/J_s is approximately 37%.

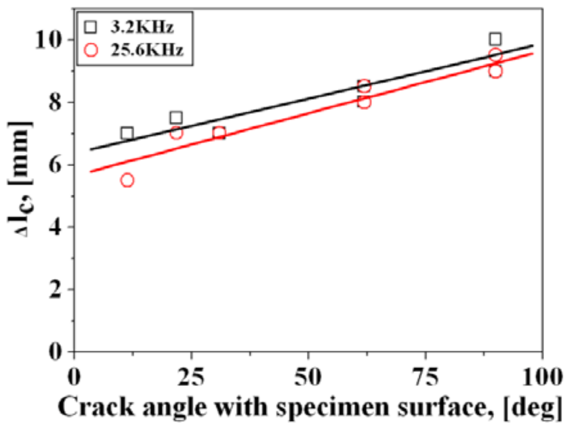

Fig. 3-16 Relationship between the θ_{TIP} and Δl_C.

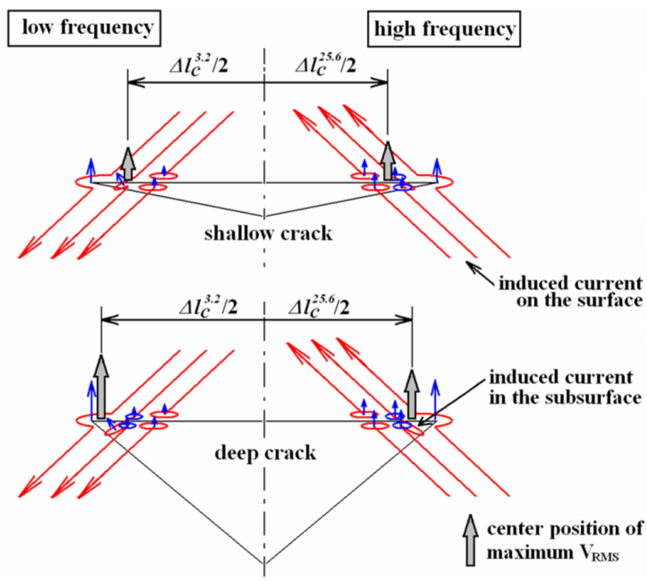

Fig. 3-17 Relationship between center position of maximum V_{RMS} versus depth of crack and frequency of induced current.

According to the skin effect, if the alternate current is low frequency, current in the subsurface is more easily induced compared to high frequency, as shown in Fig. 3-17. Correspondingly, the $\Delta l_C^{25.6}$ is shorter than the $\Delta l_C^{3.2}$. Corresponding to a decrease of crack depth, $\Delta l_C^{3.2}$ and $\Delta l_C^{25.6}$ also decrease. The depth from the surface to the crack tip at each position in the direction of crack length depends on the θ_{TIP}. The difference between $\Delta l_C^{3.2}$ and $\Delta l_C^{25.6}$ relates well to the θ_{TIP}, as shown in the following equation derived from Fig. 3-16:

$$\theta_{TIP} = 13.39 \cdot \left(\Delta l_C^{\ 3.2} + \Delta l_C^{\ 25.6} \right) - 160.54 \tag{13}$$

The real crack length, $\Delta l_{C,}$ can be calculated using Eq. (14), which is obtained empirically:

$$\Delta l_C^{\ EXP3.2} = \Delta l_C - 3.32 \cdot \cos\theta_{TIP} \tag{14}$$

As shown in Fig. 3-14 and Fig. 3-15, the distributions of V_{RMS} show small gradients in the x- and the y-direction, which expresses the STIC direction and the vertical to the x-direction on the surface of specimen respectively. These gradients are due to the deviations of the V_{RMS} distribution because of the excitation core and the STIC. These gradients are reduced by using the differential to the x-direction distance, $\partial V_{RMS}/\partial x$, and the differential to the y-direction distance, $\partial V_{RMS}/\partial y$.

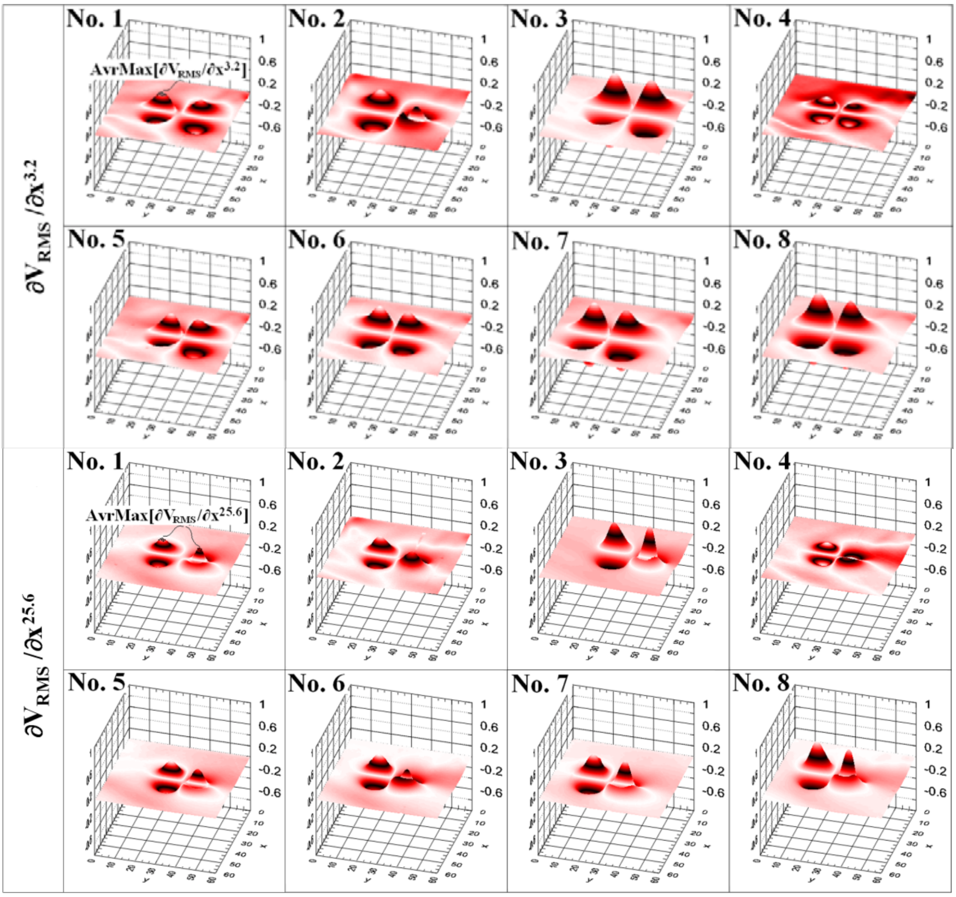

Fig. 3-18 Processed images of root mean squared value ($\partial V_{RMS} / \partial x$) at each frequency (3.2 kHz and 25.6 kHz).

The $\partial V_{RMS}/\partial x$ expresses the gradient in the x-direction. Maximum and minimum gradients, which have the positive and negative values respectively, appear on each tip of the crack according to the x-directional section at the $\partial V_{RMS}/\partial x$ distribution, as shown in Fig. 3-18. Using the maximum and minimum values of $\partial V_{RMS}/\partial x$, the crack is more easily detected compared to using the V_{RMS}. The averages of several maximum values on the distribution of $\partial V_{RMS}/\partial x$, AvrMax[$\partial V_{RMS}/\partial x^{3.2}$], and AvrMax[$\partial V_{RMS}/\partial x^{25.6}$] contain the crack size information, similarly as AvrMax[$V_{RMS}{}^{3.2}$] and AvrMax[$V_{RMS}{}^{25.6}$].

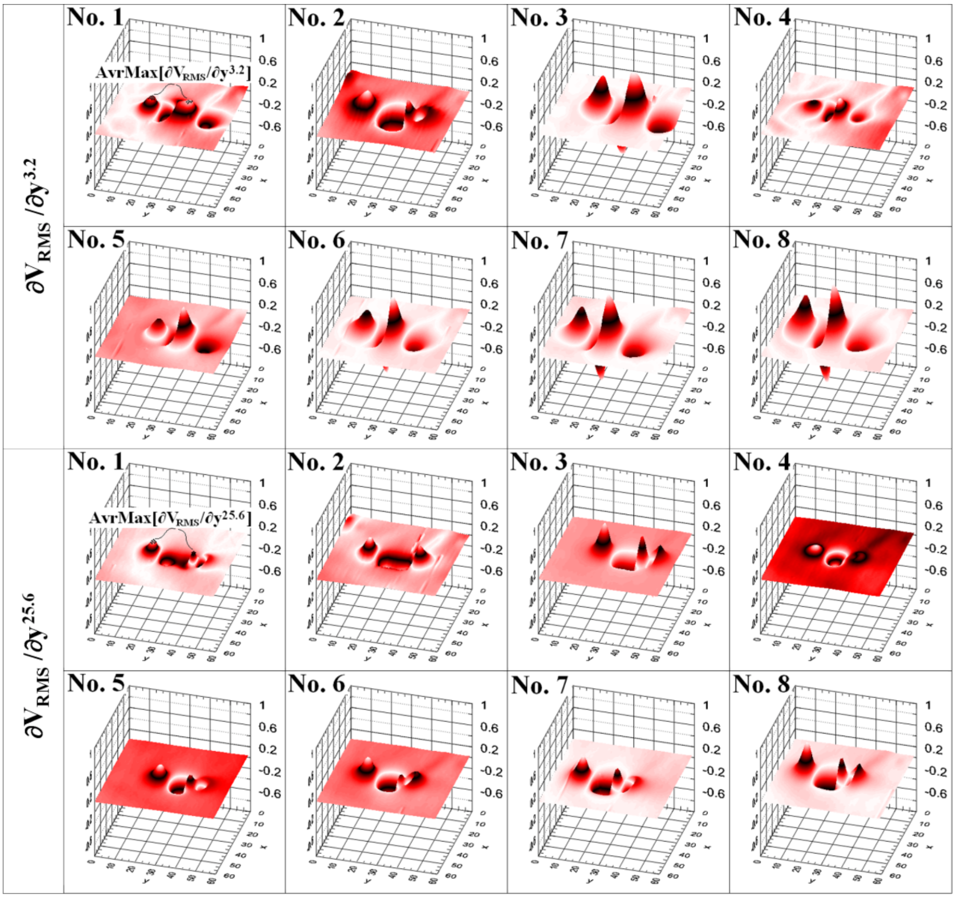

Fig. 3-19 Processed images of root mean squared value ($\partial V_{RMS} / \partial y$) at each frequency (3.2 kHz and 25.6 kHz).

Fig. 3-19 shows the distributions of $\partial V_{RMS}/\partial y$, which express the gradient in the y-direction. The maximum and minimum gradients, which have positive and negative values respectively, appear on each tip of the crack according to the y-directional section at the $\partial V_{RMS}/\partial y$ distribution, as shown in Fig. 3-19. Using these maximum and minimum values of $\partial V_{RMS}/\partial y$, the crack is more easily detected compared to using the V_{RMS}. The averages of several maximum values on the distribution of $\partial V_{RMS}/\partial y$, AvrMax[$\partial V_{RMS}/\partial y^{3.2}$], and AvrMax[$\partial V_{RMS}/\partial y^{25.6}$] contain the crack size information, similar to AvrMax[$\partial V_{RMS}/\partial x^{3.2}$] and AvrMax[$\partial V_{RMS}/\partial x^{25.6}$].

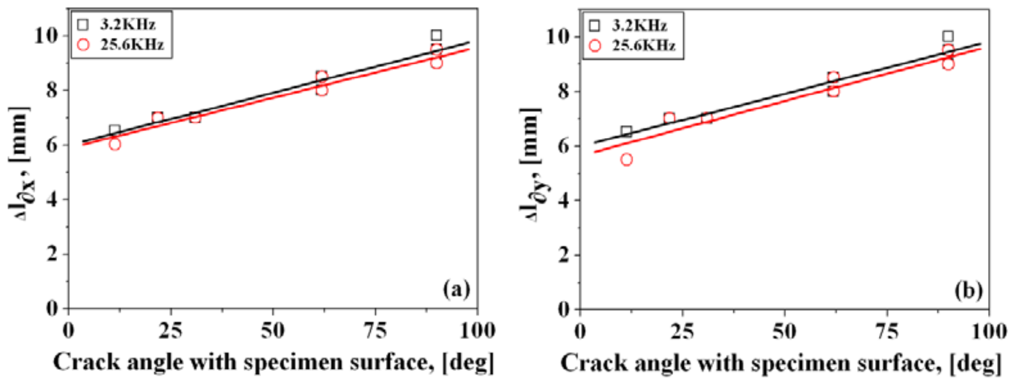

Fig. 3-20 Relationship between θ_{TIP} and (a) Δl_{dx}, (b) Δl_{dy}.

Fig. 3-20 shows the relationship between the θ_{TIP} versus $\Delta l_{dx}{}^{3.2}$, $\Delta l_{dx}{}^{25.6}$, $\Delta l_{dy}{}^{3.2}$ and $\Delta l_{dy}{}^{25.6}$, which are obtained from Figs. 3-18 and 3-19. The θ_{TIP} is estimated using following equations obtained from Fig. 3-20:

$$\theta_{TIP} = 13.3 \cdot \left(\Delta l_{dx}{}^{3.2} + \Delta l_{dx}{}^{25.6} \right) - 158.18 \tag{15}$$

$$\theta_{TIP} = 14.21 \cdot \left(\Delta l_{dy}{}^{3.2} + \Delta l_{dy}{}^{25.6} \right) - 174.62 \tag{16}$$

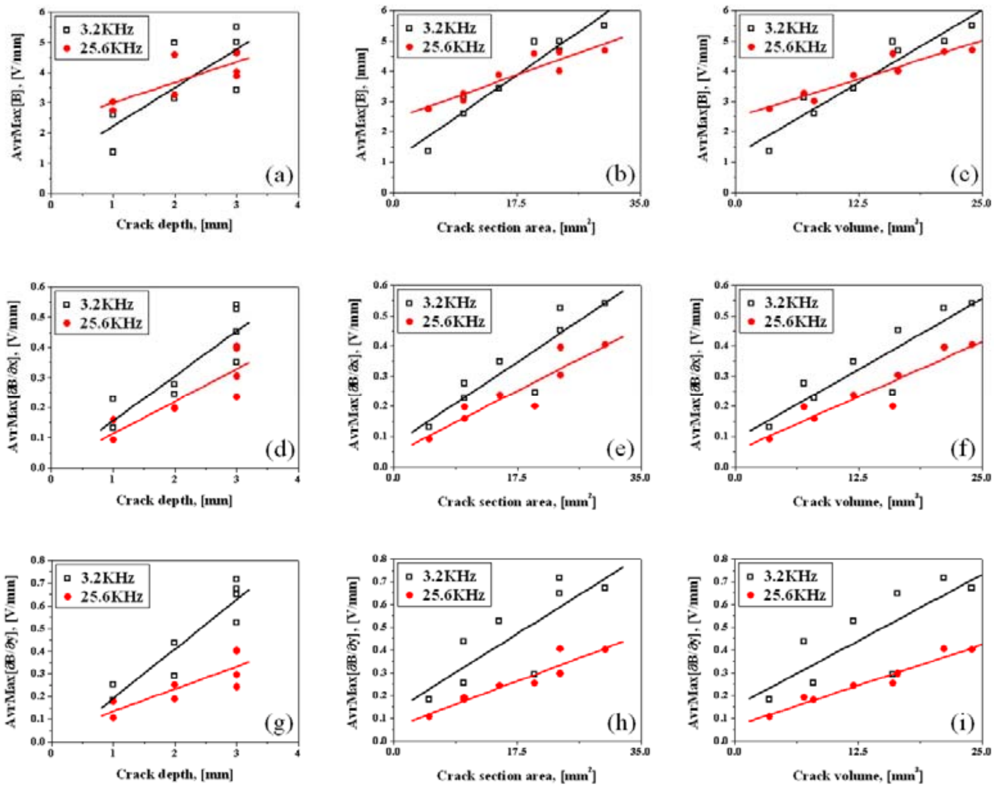

Fig. 3-21 Relationship between AvrMax[V_{RMS}], AvrMax[$\partial V_{RMS}/\partial x$], AvrMax[$\partial V_{RMS}/\partial y$] and D_{CRACK}, S_{CRACK}, V_{CRACK}.

Fig. 3-21 shows the relationships between the crack information, such as the depth (D_{CRACK}), section area (S_{CRACK}), and volume (V_{CRACK}) of each crack, with the experimental results, such as AvrMax[${V_{RMS}}^{3.2}$], AvrMax[${V_{RMS}}^{25.6}$], AvrMax[$\partial V_{RMS}/\partial x^{3.2}$], AvrMax[$\partial V_{RMS}/\partial x^{25.6}$], AvrMax[$\partial V_{RMS}/\partial y^{3.2}$], and AvrMax[$\partial V_{RMS}/\partial y^{25.6}$]. These relationships are expressed by the following equations;

$$D_{CRACK}\left({V_{RMS}}^{3.2}\right) = 0.79 \cdot AvrMax\left({V_{RMS}}^{3.2}\right) - 0.76 \tag{17}$$

$$D_{CRACK}\left({V_{RMS}}^{25.6}\right) = 1.48 \cdot AvrMax\left({V_{RMS}}^{25.6}\right) - 3.43 \tag{18}$$

$$D_{CRACK}\left(\partial V_{RMS}/\partial x^{3.2}\right)=6.7\cdot AvrMax\left(\partial V_{RMS}/\partial x^{3.2}\right)-0.04 \tag{19}$$

$$D_{CRACK}\left(\partial V_{RMS}/\partial x^{25.6}\right)=9.28\cdot AvrMax\left(\partial V_{RMS}/\partial x^{25.6}\right)-0.05 \tag{20}$$

$$D_{CRACK}\left(\partial V_{RMS}/\partial y^{3.2}\right)=4.59\cdot AvrMax\left(\partial V_{RMS}/\partial y^{3.2}\right)+0.12 \tag{21}$$

$$D_{CRACK}\left(\partial V_{RMS}/\partial y^{25.6}\right)=10.16\cdot AvrMax\left(\partial V_{RMS}/\partial y^{25.6}\right)-0.38 \tag{22}$$

$$S_{CRACK}\left({V_{RMS}}^{3.2}\right)=6.18\cdot AvrMax\left({V_{RMS}}^{3.2}\right)-6.5 \tag{23}$$

$$S_{CRACK}\left({V_{RMS}}^{25.6}\right)=12.06\cdot AvrMax\left({V_{RMS}}^{25.6}\right)-29.3 \tag{24}$$

$$S_{CRACK}\left(\partial V_{RMS}/\partial x^{3.2}\right)=64.02\cdot AvrMax\left(\partial V_{RMS}/\partial x^{3.2}\right)-4.78 \tag{25}$$

$$S_{CRACK}\left(\partial V_{RMS}/\partial x^{25.6}\right)=83.47\cdot AvrMax\left(\partial V_{RMS}/\partial x^{25.6}\right)-3.55 \tag{26}$$

$$S_{CRACK}\left(\partial V_{RMS}/\partial y^{3.2}\right)=50.94\cdot AvrMax\left(\partial V_{RMS}/\partial y^{3.2}\right)-6.54 \tag{27}$$

$$S_{CRACK}\left(\partial V_{RMS}/\partial y^{25.6}\right)=85.98\cdot AvrMax\left(\partial V_{RMS}/\partial y^{25.6}\right)-5.09 \tag{28}$$

$$V_{CRACK}\left({V_{RMS}}^{3.2}\right)=5.24\cdot AvrMax\left({V_{RMS}}^{3.2}\right)-6.49 \tag{29}$$

$$V_{CRACK}\left({V_{RMS}}^{25.6}\right)=9.87\cdot AvrMax\left({V_{RMS}}^{25.6}\right)-24.47 \tag{30}$$

$$V_{CRACK}\left(\partial V_{RMS}/\partial x^{3.2}\right)=53.5\cdot AvrMax\left(\partial V_{RMS}/\partial x^{3.2}\right)-4.79 \tag{31}$$

$$V_{CRACK}\left(\partial V_{RMS}/\partial x^{25.6}\right)=68.68\cdot AvrMax\left(\partial V_{RMS}/\partial x^{25.6}\right)-3.5 \tag{32}$$

$$V_{CRACK}\left(\partial V_{RMS}/\partial y^{3.2}\right)=43.1\cdot AvrMax\left(\partial V_{RMS}/\partial y^{3.2}\right)-6.51 \tag{33}$$

$$V_{CRACK}\left(\partial V_{RMS}/\partial y^{25.6}\right)=69.88\cdot AvrMax\left(\partial V_{RMS}/\partial y^{25.6}\right)-4.54 \tag{34}$$

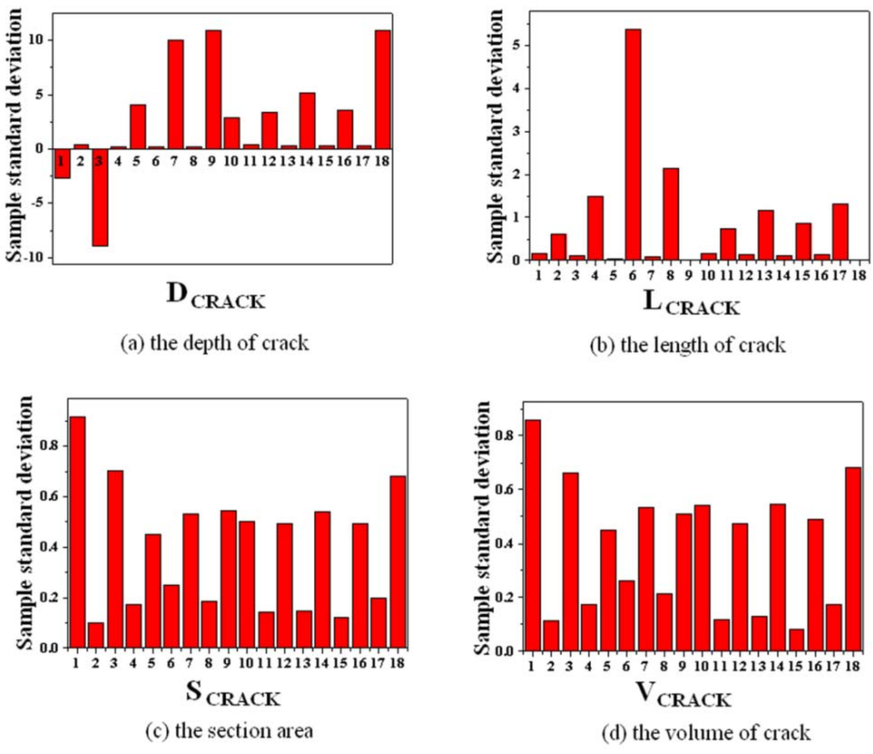

Fig. 3-22 D_{CRACK}, $L_{CRACK(exp3.2\ and\ exp25.6)}$, $S_{CRACK(section\ area)}$, V_{CRACK} versus the normalized sampling standard deviation of each factor; (1) $\Delta l_C^{3.2}$, (2) AvrMax[$V_{RMS}^{3.2}$], (3) $\Delta l_{dx}^{3.2}$, (4) AvrMax[$\partial V_{RMS}/\partial x^{3.2}$], (5) $\Delta l_{dy}^{3.2}$, (6) AvrMax[$\partial V_{RMS}/\partial y^{3.2}$], (7) $\Delta l_{dxdy}^{3.2}$, (8) AvrMax[$\partial^2 V_{RMS}/\partial x\partial y^{3.2}$], (9) $\Delta l_C^{EXP3.2}$ (10) $\Delta l_C^{25.6}$, (11) AvrMax[$V_{RMS}^{25.6}$], (12) $\Delta l_{dx}^{25.6}$, (13) AvrMax[$\partial V_{RMS}/\partial x^{25.6}$], (14) $\Delta l_{dy}^{25.6}$, (15) AvrMax[$\partial V_{RMS}/\partial y^{25.6}$], (16) $\Delta l_{dxdy}^{25.6}$, (17) AvrMax[$\partial^2 V_{RMS}/\partial x\partial y^{25.6}$], (18) $\Delta l_C^{EXP25.6}$.

Fig. 3-22 shows the relationships between factors that are introduced to estimate crack information using the normalized sampling standard deviations, $\bar{\sigma}$, obtained from Eq. (17)-(34) and the experimental results of Fig. 3-21. Usually the V_{RMS} is larger than $\partial V_{RMS}/\partial x$ and $\partial V_{RMS}/\partial y$, hence the sampling standard deviations, $\bar{\sigma}$, are not comparable to each other. Correspondingly, the normalized sampling standard deviations, $\bar{\sigma}$, represented by Eq. (35), are used to compare each other.

$$\bar{\sigma} = \sqrt{\frac{\sum_{i=1}^{n}\left(f_{EXPERIMENT} - f_{THEORY}\right)^2}{n-1}} \Big/ F.S.O \qquad (35)$$

Where, F.S.O. is the full scale operational range. The $\Delta l_C^{3.2}$ and $\Delta l_{dx}^{3.2}$ have a negative gradient, and so the F.S.O has a negative value. Then, the $\bar{\sigma}$ has negative values as shown in Fig. 3-22(a).

The (4) AvrMax[$\partial V_{RMS}/\partial x^{3.2}$], (6) AvrMax[$\partial V_{RMS}/\partial y^{3.2}$] and (8) AvrMax[$\partial^2 V_{RMS}/\partial x\partial y^{3.2}$] are useful to estimate crack depth, as shown in Fig. 3-22(a). Usually, the length of a crack is expected to relate well with $\Delta l_C^{3.2}$, $\Delta l_{dx}^{3.2}$, $\Delta l_{dy}^{3.2}$, $\Delta l_{dxdy}^{3.2}$, $\Delta l_C^{25.6}$, $\Delta l_{dx}^{25.6}$, $\Delta l_{dy}^{25.6}$, and $\Delta l_{dxdy}^{25.6}$. However, these factors have large errors as shown in Fig. 3-22(b) due to the aforementioned shape of the crack. Fortunately, Δl_C^{EXP} can be used to estimate crack length with small $\bar{\sigma}$, as shown in Fig. 3-22(b). Furthermore, (2) AvrMax[$V_{RMS}^{3.2}$], (4) AvrMax[$\partial V_{RMS}/\partial x^{3.2}$], (11) AvrMax[$V_{RMS}^{25.6}$], (13) AvrMax[$\partial V_{RMS}/\partial x^{25.6}$], and (15) AvrMax[$\partial V_{RMS}/\partial y^{25.6}$] can be used to estimate the crack section area and volume because of small $\bar{\sigma}$. The $\bar{\sigma}$ of the V_{CRACK} and S_{CRACK} are 0.080461 and 0.10058 respectively, meaning that the equation used to evaluate a V_{CRACK} has a smaller error compared to the one used to evaluate S_{CRACK}. Correspondingly, the effect of the width of the crack on the distribution of the V_{RMS} cannot be ignored because V_{CRACK} is obtained by multiplying the S_{CRACK} by the width of a crack.

3. *Discussions*

A sheet type induced current on the specimen and single Hall sensor scanning are used to inspect and evaluate a crack quantitatively on a paramagnetic aluminum alloy. A crack can be inspected by using the distribution of RMS Hall voltages caused by the alternate magnetic flux leakage around the crack tips. Alternate magnetic flux leakage occurs from distortion of the sheet type induced current at the crack tips. The angle between the depth directional crack edge and the surface of a specimen can be obtained by using the distance between the inflection points of the distribution of the RMS magnetic flux leakage and their processed results. The real length of crack can be calculated using an empirical equation that uses the distance between the peak of the root mean squared Hall voltages at the 3.2 kHz and the calculated crack tip angle. Conversely, the volume and the section area of the crack can be estimated quantitatively by using the average of 50 maximum values of the V_{RMS}, $\partial V_{RMS}/\partial x$, $\partial V_{RMS}/\partial y$ and $\partial^2 V_{RMS}/\partial x \partial y$ distribution.

C. NDT OF COLD ROLLED STEEL

Generally, cold rolled steel is relatively thick, has a clean surface, accuracy dimension, is flat, and has an easy mechanical forming property. Correspondingly, this steel is widely used in the exterior plate of automobiles, fireproof safes, office desks, refrigerators, washing machines, and kitchen utensils. However, the small cracks, generated during the manufacturing process, affect the quality deterioration of the final products. Therefore, these cracks have to be inspected and evaluated during the manufacturing step where magnetic particle testing has been used. Pre- and post-processing are necessary. Expendables, such as magnetic particles, have to be used continuously in magnetic particle testing. Furthermore, a large amount of electric power has to be used to magnetize the specimen.

We propose a method, in this chapter, which can detect and evaluate cracks on cold rolled steel, without expendables such as magnetic particles, without pre- and post-processing, and with smaller electric power required than the magnetic particle testing method. That is, we successfully detected and evaluated cracks on a specimen by using a scan type magnetic camera, which uses a linearly integrated Hall sensor array as a magnetic sensor and a small yoke type alternative magnetizer as a magnetic source.

1. *Specimens*

Fig. 3-23 shows the crack position on a cold rolled steel plate with 300 × 300 × 1.8 mm sizes. The several length, width, depth of slit, and hole type cracks, as shown in Table 4, were introduced by using electric discharge machining.

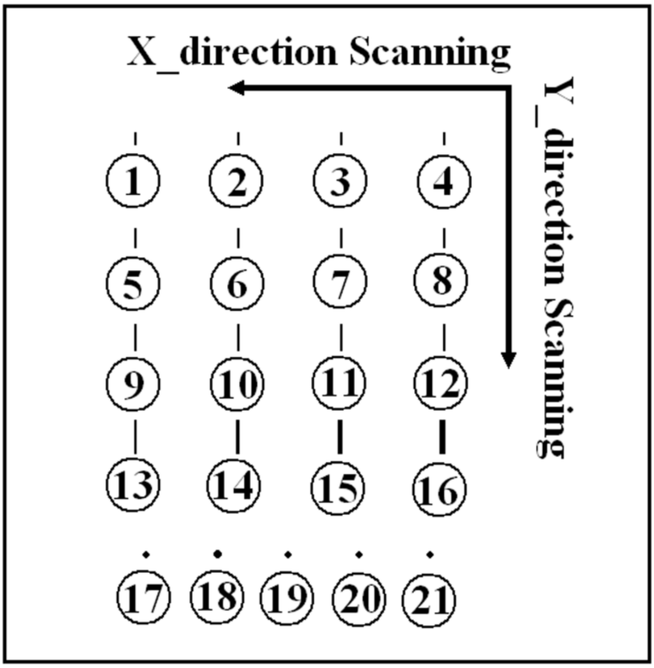

Fig. 3-23 Cold rolled steel specimen.

Table 4 Shapes and sizes of each crack

No	**Length [mm]**	**Width [mm]**	**Depth [mm]**	**No**	**Length [mm]**	**Width [mm]**	**Depth [mm]**
1	2	0.3	0.1	9	4	0.3	0.1
2	2	0.3	0.3	10	4	0.3	0.3
3	2	0.3	0.4	11	4	0.3	0.4
4	2	0.3	0.5	12	4	0.3	0.5
5	3	0.3	0.1	13	5	0.3	0.1
6	3	0.3	0.3	14	5	0.5	0.3
7	3	0.3	0.4	15	5	0.7	0.4
8	3	0.3	0.5	16	5	0.9	0.5
No	**Diameter [mm]**		**Depth [mm]**	**No**	**Diameter [mm]**		**Depth [mm]**
17	0.2		0.2	20	0.35		0.2
18	0.4		0.4	21	0.3		0.1
19	0.35		0.5				

2. *Experimental Equipment*

Fig. 3-24 shows a schematic of our experimental set-up. The 200 mA alternative current, with 1 kHz, amplified by using a function generator and a power amplifier, was applied in the coil of the core, that is, the yoke-type magnetizer.

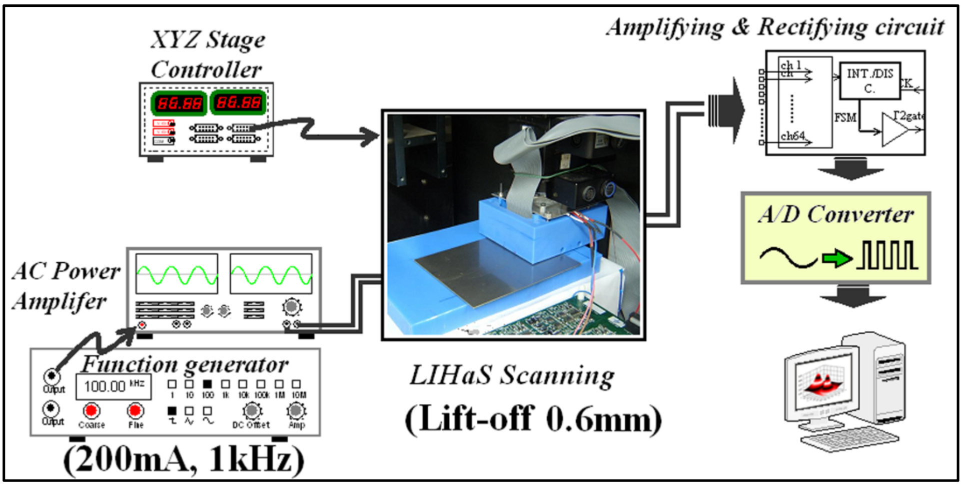

Fig. 3-24 Experimental equipment.

Fig. 3-25 shows a schematic of the small yoke type magnetizer (hereafter yoke). The y- and x-direction represent the sensor array direction and scanning direction of the LIHaS, respectively. The z-direction indicates the vertical direction to the specimen plane. A core, having a length of 40 mm in the y-direction, a width of 16 mm in the x-direction, a height of 27 mm in the z-direction, a thickness of 3.5 mm, is located on the backside of the LIHaS. The x-directional magnetic field occurs in the specimen as shown in Figs. 3-25(b) and (c), An alternative current of 0.28 A with 1 kHz is applied in the coil, wound on the both sides of the core, with 16 mm of height and 3 mm of thickness.

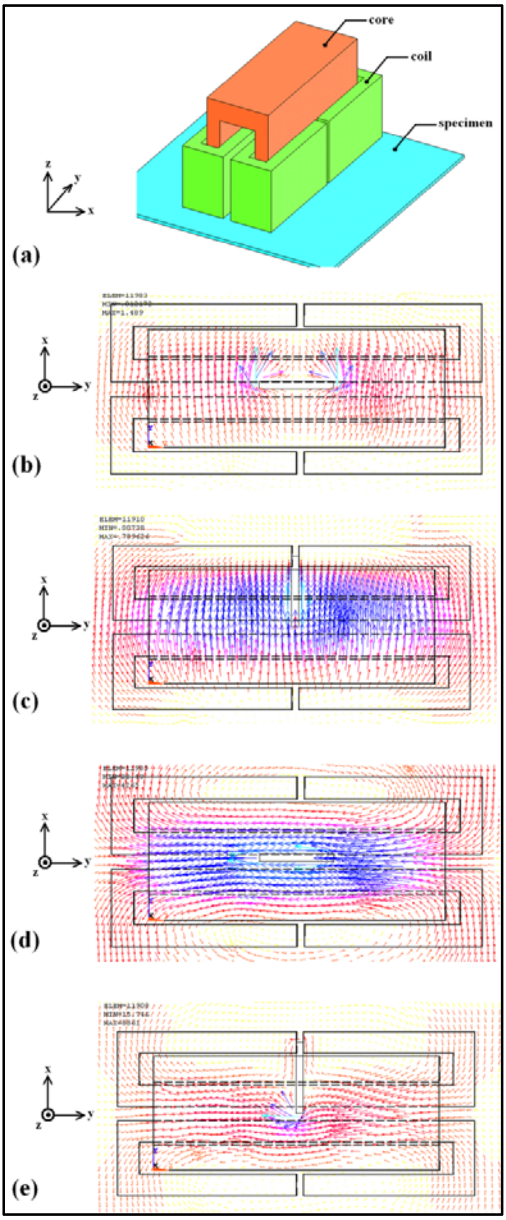

Fig. 3-25 Numerical analysis of the electro-magnetic field around each crack using a small sized yoke type magnetizer operated by an alternative current of 1kHz: (a) Analysis model; (b) Magnetic field on the y-directional crack; (c) Magnetic field on the x-directional crack; (d) Electric field on the y-directional crack; (e) Electric field on the x-directional crack.

Also, the input current to the LIHaS was 300 mA, and the lift-off was 0.6 mm. The 64 InSb Hall elements were arrayed on a Ni-Zn ferrite wafer with 0.52 mm intervals as shown in Fig. 3-26.

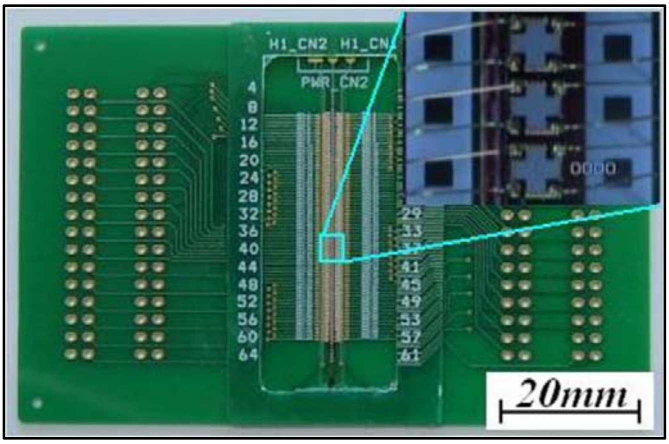

Fig. 3-26 Linearly integrated 64 InSb Hall sensor array on a NiZn ferrite wafer.

The 64 analog-to-digital convertors (ADC) were used to store the distribution of Hall voltages, that is, the distribution of magnetic field in the computer. The scanning interval was 0.5 mm.

3. *Discussions*

Figs. 3-27 and 28 show the distribution of $\partial V_{RMS}/\partial x$ on a specimen shown in Fig. 3-23. The $\partial V_{RMS}/\partial x$ distribution is useful to reduce the bias error of each sensor of the LIHaS, and is obtained by using the following equation: [6, 19]

$$\frac{\partial V_{RMS}}{\partial x}(x,y,z) \approx \frac{V_{RMS,Total}(x+\Delta x,y,z) - V_{RMS,Total}(x,y,z)}{\Delta x} \tag{36}$$

The crack could be detected in either the case of the crack direction being vertical to the magnetization direction (Fig. 3-27) or horizontal to the direction (Fig. 3-28). The smallest slit type crack with 2 mm, 0.3 mm, and 0.1 mm of length, width, and depth, respectively, (No.1), could be detected on the lift-off 0.6 mm. Also, the smallest hole type crack with 0.2 mm of depth and diameter (No.17) was clearly detected

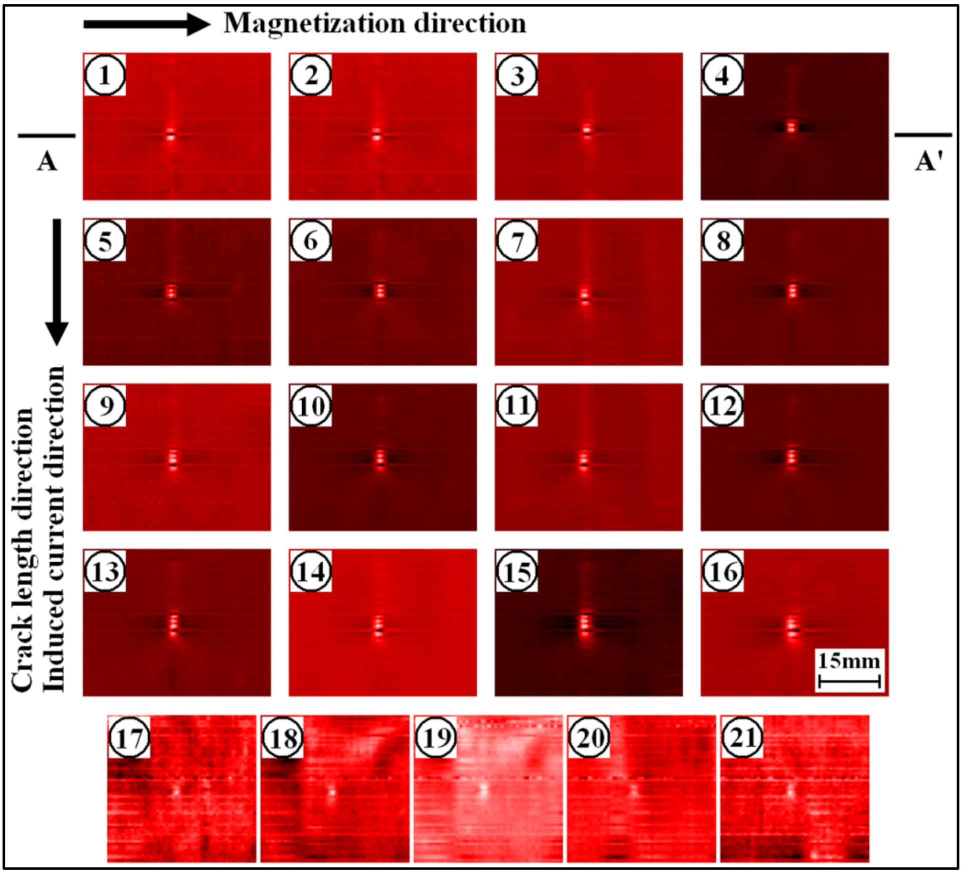

Fig. 3-27 Experimental results for the horizontal direction with a rolling direction

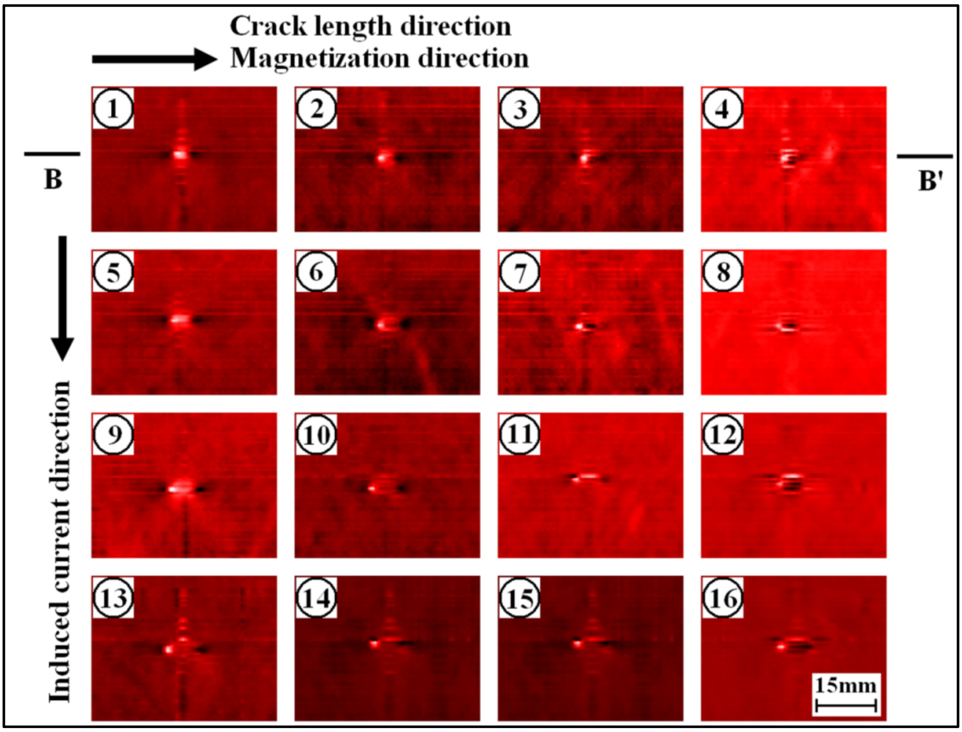

Fig. 3-28 Experimental results for the vertical direction with a rolling direction

This was because the magnetic flux leakage was maximized in the case of Fig. 3-27, and the distortion of the induced current was maximized in the case of Fig. 3-28 as abovementioned, in abovementioned paragraph The Combined Induced Current-Magnetic Flux Leakage Method, with the CIC-MFL method. Figs. 3-29 and 30 show the sectional distribution of $\partial V_{RMS}/\partial x$ on each crack. The $\partial V_{RMS}/\partial x$ values are increased proportional to the crack size. Correspondingly, the $\partial V_{RMS}/\partial x$ values could be used to evaluate a crack. Other researchers have proposed an algorithm for crack volume estimation in prior research [10] as shown in following equation:

$$\left.\frac{\partial V_{RMS}}{\partial x}\right|_{Total} = \sum_{i=1}^{Lc/S}\left[Max(\frac{\partial V_{RMS,i}}{\partial x}) + Abs(Min(\frac{\partial V_{RMS,i}}{\partial x}))\right] \tag{37}$$

Here, L is the length of each crack obtainable from the distribution of $\partial V_{RMS}/\partial x$ as shown in Figs. 3-27 and 28. Also, S is the scanning spatial resolution and is 0.5 mm in this chapter.

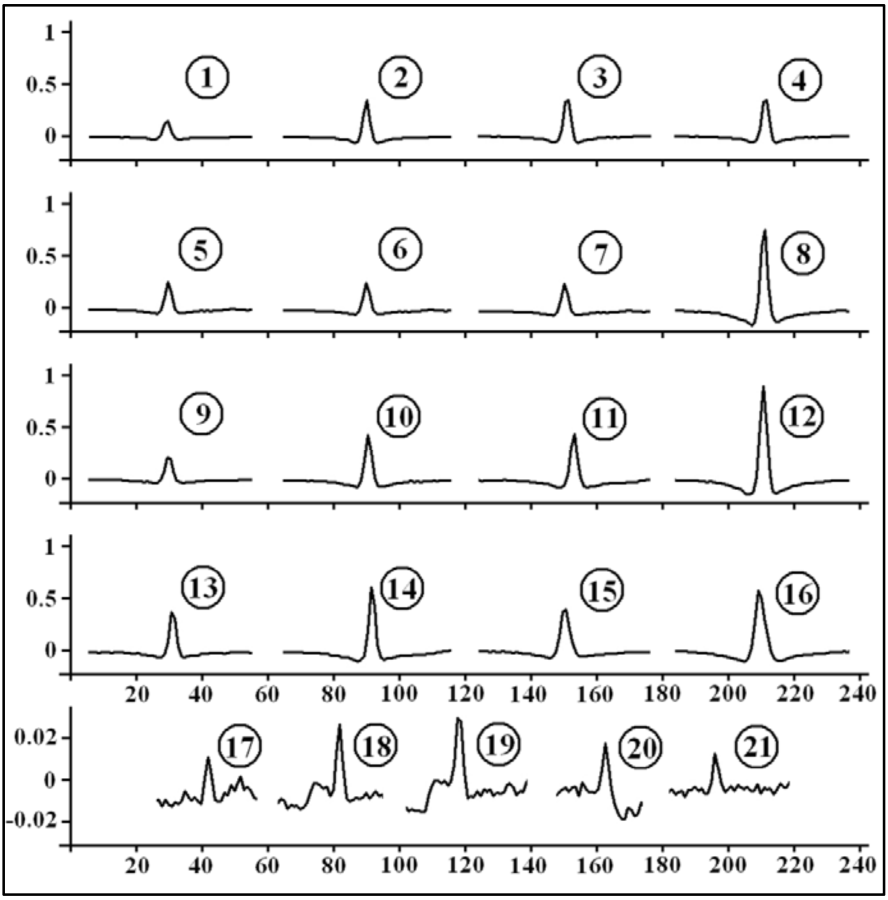

Fig. 3-29 A-A' section view of each crack seen in Fig. 3-27

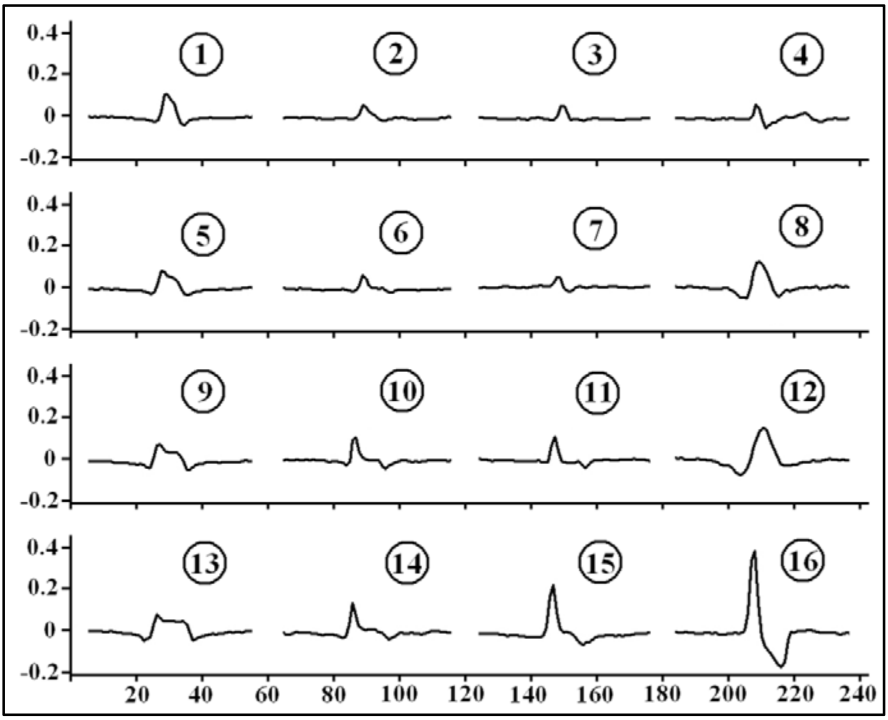

Fig. 3-30 B-B' section view of each crack seen in Fig. 3-28

Fig. 3-31 shows the relationship between the real volume of a crack and the calculated $\partial V_{RMS}/\partial x|_{total}$ as shown in Eq. (37). The filled marks (●) show the case where the crack length direction is vertical to the magnetization direction and the magnetic field leakage could be a main factor in inspecting each crack. The empty marks (○) designate the case of the crack's length direction being vertical to the induced current. The distortion of the induced current could be a main factor for inspection of cracks. The intensity of $\partial V_{RMS}/\partial x|_{total}$ due to the magnetic flux leakage is 4.26 times larger than $\partial V_{RMS}/\partial x|_{total}$ due to the distortion of the induced current. Also, $\partial V_{RMS}/\partial x|_{total}$ is increased without distinguishing changes when the crack volume is over 0.75 mm^3 (No.14). This phenomenon is because of the crack width. That is, the magnetic flux leakage can be offset with a magnetic field due to the distortion of the induced current when the crack width increases.

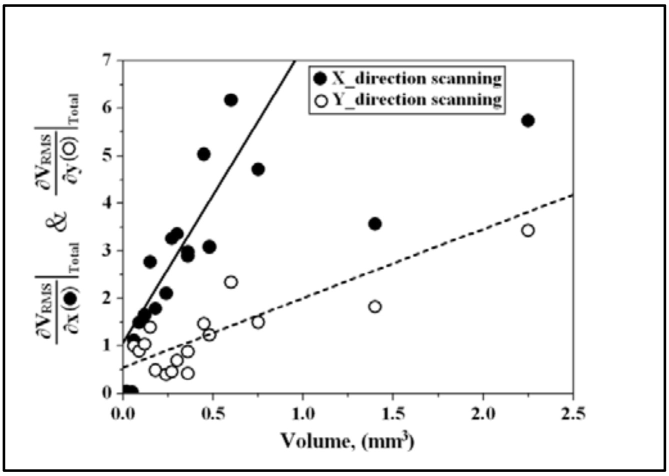

Fig. 3-31 Evaluation of the slit type crack volume using the proposed algorithm

Conversely, both of the magnetic flux leakage and the distortion of induce current could affect the $\partial V_{RMS}/\partial x|_{total}$ for hole type cracks. The $\partial V_{RMS}/\partial x|_{total}$ increased proportional to the increase of crack volume as shown in Fig. 3-32. The magnitude of the $\partial V_{RMS}/\partial x|_{total}$ values are on the extension line of the case of distortion of the induced current, as shown as a dotted line in Fig. 3-31. This tendency is because the leakage of the magnetic flux around the hole type crack is minimized compared with the slit type crack having an immediately changed section area.

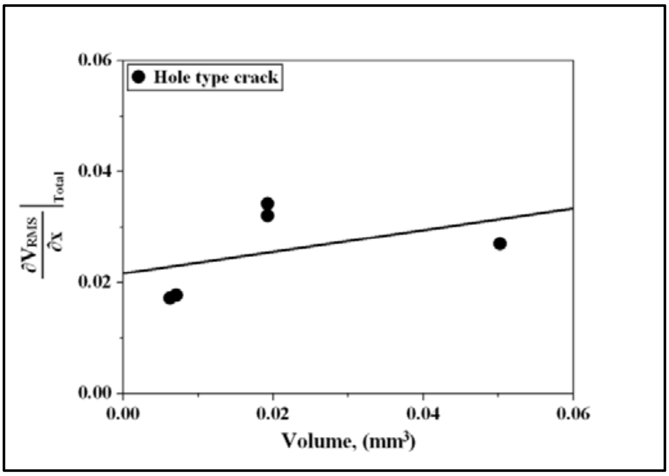

Fig. 3-32 Evaluation of the hole type crack volume using the proposed algorithm

We proposed an inspection and evaluation method for cracks on a cold rolled steel plate. The slit type crack could be detected independent of the length direction by using an improved magnetic source; that is, the Combined induced current, the magnetic flux leakage, and the linearly integrated InSb Hall sensor array on a NiZn ferrite wafer. The hole type crack, with 0.2 mm of diameter and depth, respectively, could be detected on a lift-off 0.6 mm. The slit type crack, with 2, 0.3, and 0.1mm of length, width, and depth, could be detected, also. The calculated $\partial V_{RMS}/\partial x|_{total}$, obtainable from experimental data, showed a good relationship with the real crack volume.

D. NDT OF INCONEL BY PENETRATING OF THE MAGNETIC FLUID

The Inconel series of materials has been used in nuclear plants as an important structural material because of its anticorrosive and heat-resistant properties. Cracks in the components of a plant must be detected easily and evaluated quantitatively. Inconel is a paramagnetic material, and its electrical conductivity (0.986×10^6 S/m) is much less than copper (5.08×10^7 S/m) and aluminum (3.82×10^7 S/m). Therefore, electromagnetically-based methods such as magnetic particle testing (MT), magnetic flux leakage testing (MFLT) and eddy current testing (ECT) have difficulty detecting and evaluating small cracks in Inconel specimens [9]. Dye penetration testing (PT) has been used to detect cracks in Inconel; however, the quantitative evaluation of a crack is difficult using this method [48].

We propose a novel nondestructive testing (NDT) method to detect and evaluate open surface cracks in paramagnetic materials using penetrating magnetic fluid. Magnetite particles several nanometers in diameter are combined with surfactant, and dispersed in menstruum such as water or kerosene, in the magnetic fluid. The magnetic fluid can thus penetrate a crack by capillary action. A magnetic camera developed by the authors is used to detect and evaluate the penetrated magnetic fluid, and thereby determine the shape and size of the crack. The proposed method is verified by detecting and evaluating cracks of various sizes in an Inconel 600 specimen.

1. ***Principles***

a. **Penetrating of the magnetic fluid**

Ferromagnetic nanometer-scaled particles can be dispersed in a menstruum such as hydrocarbon, ester, ether, kerosene, or water, after bonding with surfactant. This dispersed magnetic fluid has been classified as a super-paramagnetic material, which has ferromagnetic and paramagnetic properties in and without an external magnetic field, respectively, with a single magnetic domain structure [49]. Therefore, a magnetic fluid shows little hysteresis in its magnetization curve, and has little residual magnetization. In addition a magnetic fluid demonstrates capillary phenomenon. Such a fluid can therefore penetrate an open surface crack according to following equation [50]:

$$h = \frac{2T \times \cos\theta}{r \cdot \rho \cdot g} \tag{38}$$

Eq. (38) shows that the penetration height *h* of the liquid in a capillary is directly proportional to the cosine of the contact angle θ and surface tension T, and is inversely proportional to the diameter of capillary r, density of liquid ρ, and acceleration of gravity g. The liquid can easily penetrate when the diameter of the capillary is small. For the water-based magnetic fluid used in this chapter, magnetite (Fe_3O_4) particles of nanometer-scale bond with the hydrophobic radical of the first layer surfactant, sodium oleic acid, and with the second layer surfactant with the hydrophilic radical, sodium dodecyl bensene sulfonate, in the magnetic fluid [49]. Therefore, we can assume that the surface tension of the magnetic fluid is same as water, 73 mN/m [50]. The density of the magnetic fluid used in this chapter (Ferrotec Co., exp. 92017) is 1,227 kg/m^3. The contact angle was approximately 60˚ with acrylic resin.

Therefore, according to Eq. (38), when the diameter of a crack is 200 μm, the penetration height is 30.4 mm. Furthermore, the penetrated magnetic fluid in a crack can be removed and recycled by using a strong magnetizer and water after testing.

b. **Numerical analysis of EMF**

A small yoke magnetizer, located on the bottom of the LIHaS as shown in Fig. 3-33(a), was used in our magnetic camera. Alternating current (AC) or direct current (DC) are applied to the coil, which was wound on the core. Fig. 3-33(b) shows an analysis model of the magnetizer shown in Fig. 3-33(a). The x- and y-direction represent the scanning direction and the sensor array direction on the LIHaS, respectively. The vertical direction to the specimen is represented as the z-direction. The magnetizer has the following specifications: core length = 40 mm, x-directional width = 16 mm, z-direction height = 27 mm, core thickness = 3.5 mm, magnetic relative permeability (MURX) = 250, and electrical resistivity (RSVX) = 1.6 x 10^{-7} Ωm.

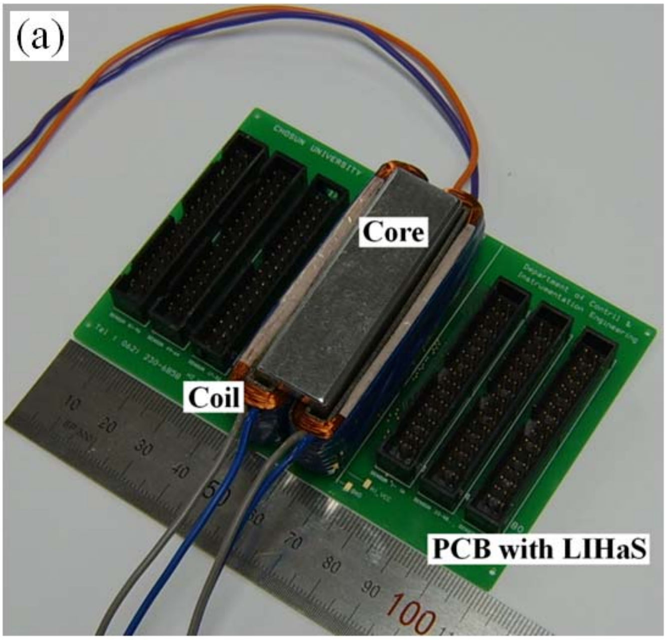

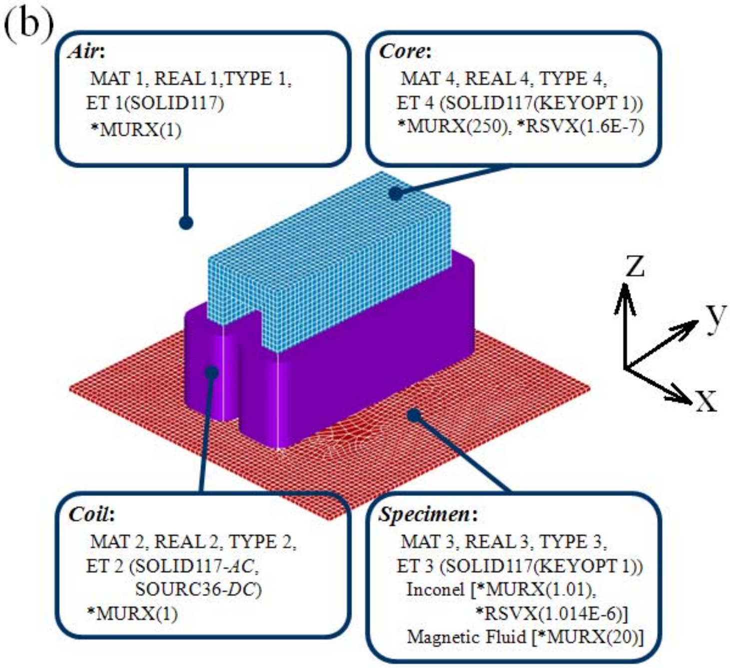

Fig. 3-33 Small yoke-type magnetizer and analysis model; (a) photograph, (b) analysis model

The magnetizer is located on the Inconel specimen (60 mm × 60 mm × 0.8 mm, MURX = 1.01, RSVX = 1.014 x 10^{-6} Ωm) with 2 mm of lift-off. A crack (width = 1 mm, length = 10 mm, depth = 0.8 mm) is positioned on the specimen, and filled with magnetic fluid (MURX = 20). When DC of 0.28 A is applied to each coil (MURX = 1), a magnetic field is generated in the x-direction in the specimen as shown in Fig. 3-34. We represent this magnetization method as the direct current-magnetic flux leakage (DC-MFL) method. Fig. 3-34(a) and Fig. 3-34(b) show the distribution of the magnetic field on the x- and y-directional crack with magnetic fluid penetration, respectively. The leakage magnetic field is maximized around the crack when the crack length direction is perpendicular to the magnetization direction (x-direction), as shown in Fig. 3-34(b). Also, the crack will be difficult to detect when the length of the crack is parallel to the magnetization direction because of the minimization of the leakage magnetic field, as shown in Fig. 3-34(a).

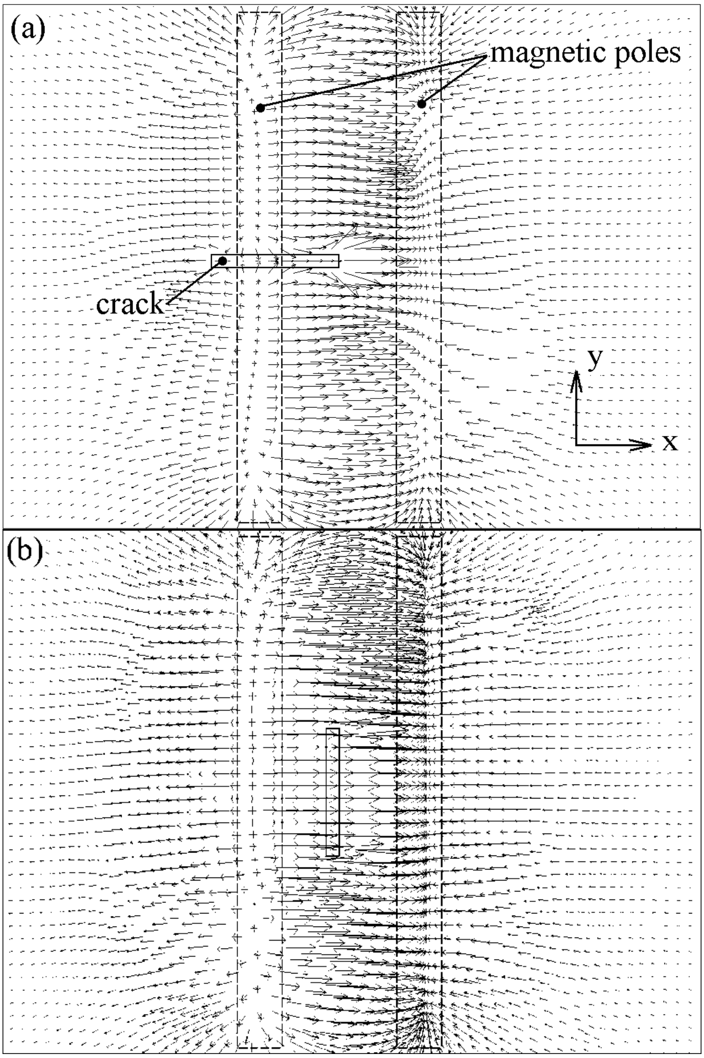

Fig. 3-34 Analyzed distribution of magnetic field on the Inconel specimen with DC current supply; (a) x-directional crack with magnetic fluid penetration, (b) y-directional crack with magnetic fluid penetration

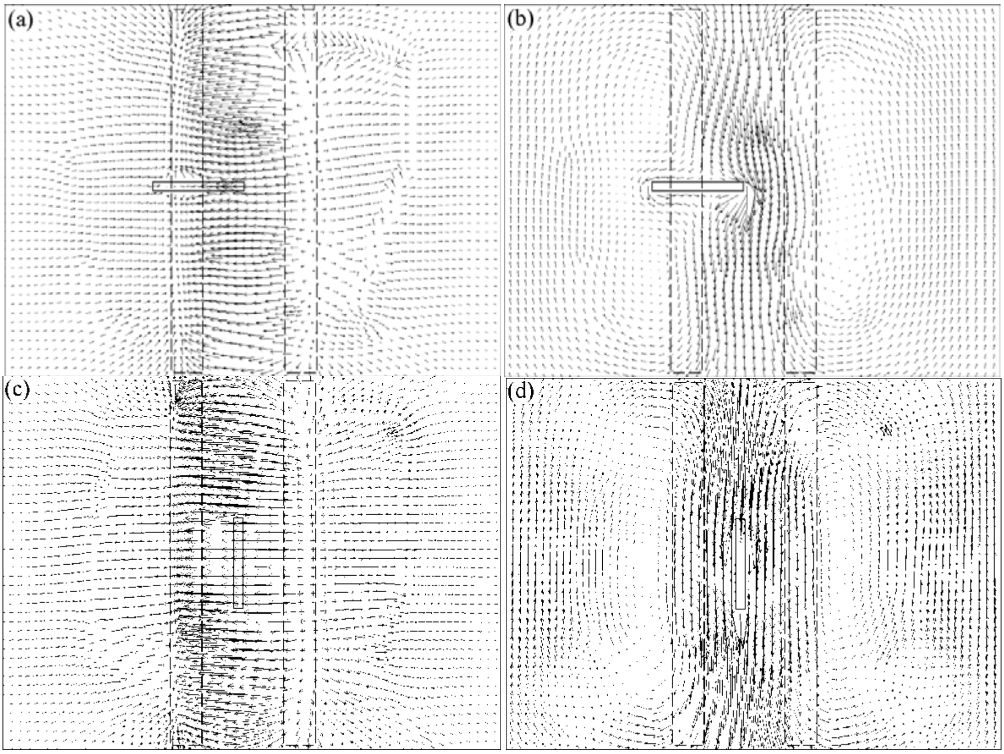

Fig. 3-35 Analyzed distribution of magnetic and electric field on the Inconel specimen with AC current supply; (a) magnetic field on x-directional crack with magnetic fluid penetration, (b) electric field on x-directional crack with magnetic fluid penetration, (c) magnetic field on y-directional crack with magnetic fluid penetration, (d) electric field on y-directional crack with magnetic fluid penetration

The crack, shown in Fig. 3-34(a), can be detected using AC input to the coil. Fig. 3-35 represents the analyzed distribution of the magnetic field (Fig. 3-35(a) and (c)) and the electric field (Fig. 3-35(b) and (d)) on the specimen when AC of 0.28 A and a frequency of 1 kHz is applied to the coil. That is, the magnetic fluxes appeared to the magnetization direction (scanning direction and x-direction) and the electric fluxes appeared to the LIHaS direction (y-direction) at the same time. The distortion of the electric field around a crack is maximized when the crack length direction is parallel to the x-direction, as shown in Fig. 3-35(b). Also, the z-directional magnetic field due to the distortion of the electric field can be measured using a

LIHaS, so the crack can be detected easily even though it was difficult to detect at the DC supply, as shown in Fig. 3-34(a). Conversely, the crack can be detected effectively using the magnetic field when the crack length direction is perpendicular to the magnetization direction, as shown in Fig. 3-35(c). Because both the electrical field; that is, induced current (IC), and the magnetic field; that is, the magnetic field leakage (MFL) , can be used to detect a crack, we have called this method a combined induced current and magnetic field leakage method (CIC-MFL) [9].

A Hall sensor has two power input pins and two output pins. The difference in voltage between the two output pins is proportional to the intensity of the external magnetic field. Usually, a differential operational amplifier has been used to measure the z-directional magnetic field intensity. The output voltage after the differential operational amplifier (V) is the alternative signal, which includes information about magnetic field leakage and distortion of induced current in the CIC-MFL method. Also, the amplitude of V can be converted to a DC signal using the root-mean-square (RMS) [13]. The differential value ($\partial V/\partial x$ ($\partial V_{RMS}/\partial x$) or $\partial V/\partial y$ ($\partial V_{RMS}/\partial y$)) of the RMS signal V_{RMS} in the CIC-MFL method, and the amplified Hall voltage V in the DC-MFL method, in the x-direction (or y-direction), allows a more clear indication of the crack than V_{RMS} or V [17].

2. *Specimen and Experimental Equipment*

a. **Specimen**

Fig. 3-36 shows cracks on an Inconel 600 specimen with dimensions of 185 mm × 146 mm × 2 mm. Slit-type cracks of various sizes were introduced using electro-discharge-machining. Each crack size is indicated in Table 5. The x-direction represents the length direction of crack, and the y-direction is vertical with respect to the x-direction on the specimen. The water based magnetic fluid (Ferrotec Co., exp. 92017) was dropped on each crack, and the specimen was scrubbed out after 6 minutes. The penetrated magnetic fluid in each crack was isolated with air by putting tape on the specimen. After the experiment, most of penetrated magnetic fluid could be removed using a neodymium magnetizer in water for 10 minutes. Conversely, the ferromagnetic impurities of AISI 1018 and AISI 4340 were inserted in same specimen at locations D2, D3, E2, and E3, as shown in Fig. 3-36. Also, two particles of AISI 4340 were attached at location of D5 and E5.

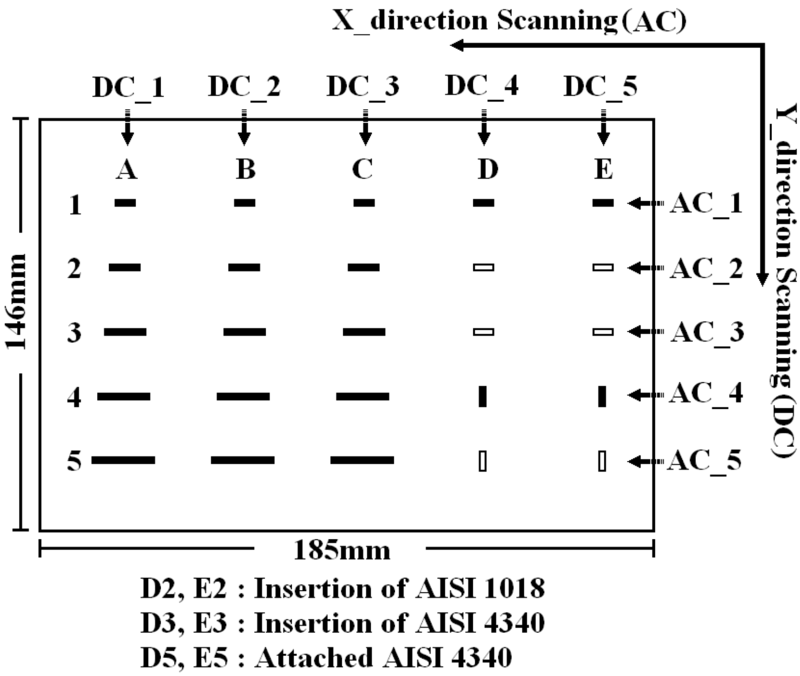

Fig. 3-36 Inconel specimen

Table 5 Shapes and Sizes of each crack

No	Width [mm]	Length [mm]	Depth [mm]	Volume [mm^3]	No	Width [mm]	Length [mm]	Depth [mm]	Volume [mm^3]
A1	0.12	2	0.2	0.048	D1	0.15	1.6	0.5	0.12
A2	0.12	4	0.2	0.096	D2	0.15	1.6	0.5	0.12
A3	0.12	6	0.2	0.144	D3	0.15	1.6	0.5	0.12
A4	0.12	8	0.2	0.192	D4	0.15	1.6	0.5	0.12
A5	0.12	10	0.2	0.24	D5	0.15	1.6	0.5	0.12
B1	0.12	2	0.4	0.096	E1	0.5	1	0.2	0.1
B2	0.12	4	0.4	0.192	E2	0.7	1.6	0.2	0.224
B3	0.12	6	0.4	0.288	E3	0.7	1.6	0.2	0.224
B4	0.12	8	0.4	0.384	E4	0.5	1	0.2	0.1
B5	0.12	10	0.4	0.48	E5	0.15	1.6	0.2	0.048
C1	0.12	2	0.6	0.144					
C2	0.12	4	0.6	0.288					
C3	0.12	6	0.6	0.432					
C4	0.12	8	0.6	0.576					
C5	0.12	10	0.6	0.72					

b. **Experimental equipment**

Fig. 3-37 shows our experimental setup. 64 InSb Hall sensors were arrayed at 0.52 mm intervals on a NiZn ferrite wafer on LIHaS. The LIHaS with a small yoke magnetizer, as shown in Fig. 3-33, is established on the bottom of a high precision scanning system. The lift-off is 1 mm, and the spatial resolution in the scanning direction is 0.5 mm. DC 200 mA and AC 200 mA at 1 kHz were supplied to the magnetizer for the DC-MFL and CIC-MFL methods, respectively. The amplitude rate of the Hall voltage is 1,500 for the DC-MFL method, and 400 for the CIC-MFL method. The y-directional scanning data, $\partial V_{RMS}/\partial y$, was obtained using the DC-MFL method. The x-directional scanning data, $\partial V/\partial x$, was obtained using the CIC-MFL method.

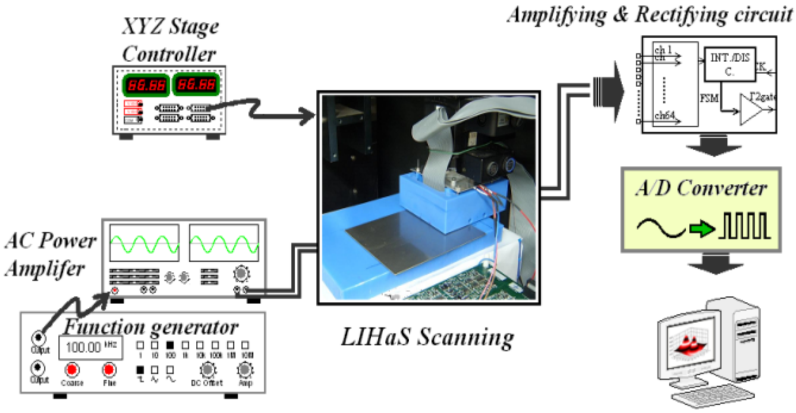

Fig. 3-37 Experimental equipment

3. ***Discussions***

Fig. 3-38 shows the $\partial V_{RMS}/\partial x$ distribution using the CIC-MFL method. A large distortion of induced current, as shown in Fig. 3-35(b), appeared at the tips of the crack. Therefore, $\partial V_{RMS}/\partial x$ is maximized at the crack tips as shown in Fig. 3-38. Note that the crack length direction is parallel to the magnetization direction in Fig. 3-38. Usually, the crack is difficult to detect in DC-MFL. However, by using CIC-MFL, the crack was detected. Conversely, the D4 and E4 cracks were difficult to detect on AC_4 in Fig. 3-38 because the crack sizes were small and the distorted induced current at the tips of cracks were minimized due to the crack length direction. The crack length could be estimated from the $\partial V_{RMS}/\partial x$ distribution as shown in Fig. 3-38.

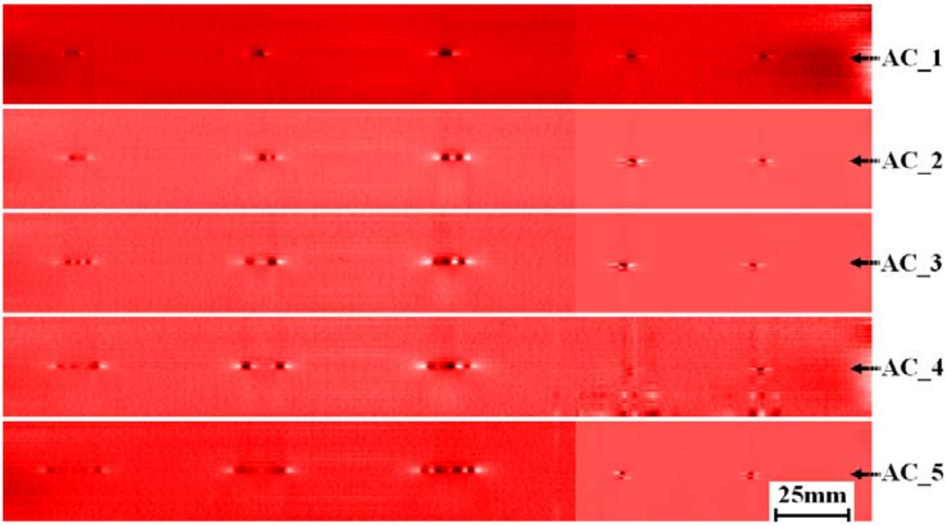

Fig. 3-38 $\partial V_{RMS}/\partial x$ distributions obtained by scanning to the x-direction with CIC-MFL method

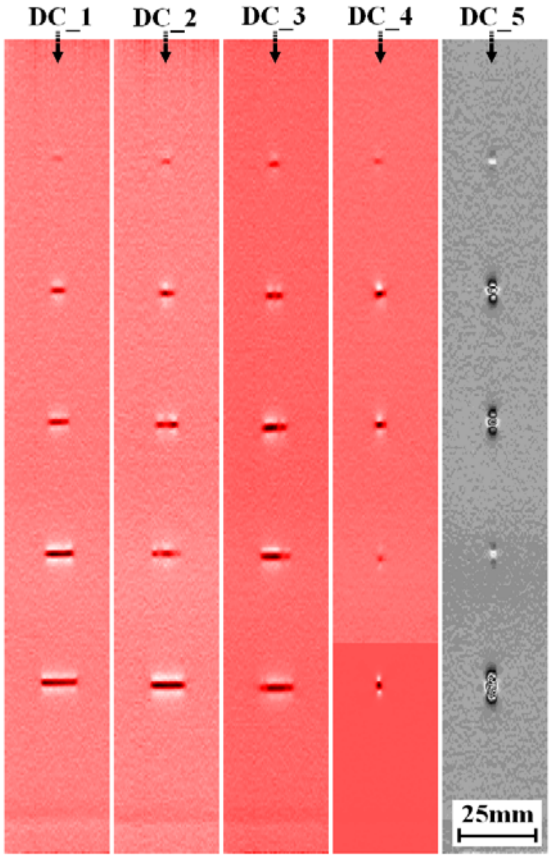

Fig. 3-39 $\partial V/\partial y$ distributions obtained by scanning to the y-direction with CIC-MFL method

Fig. 3-39 shows the $\partial V/\partial y$ distribution using the DC-MFL method. The length of the crack could be estimated more clearly than in Fig. 3-38. Also, the crack indication images more clearly appeared to be proportional to the increase in length and depth of the crack, similar to Fig. 3-38. Correspondingly, crack sizes can be evaluated using the distribution of $\partial V/\partial y$ and $\partial V_{RMS}/\partial x$.

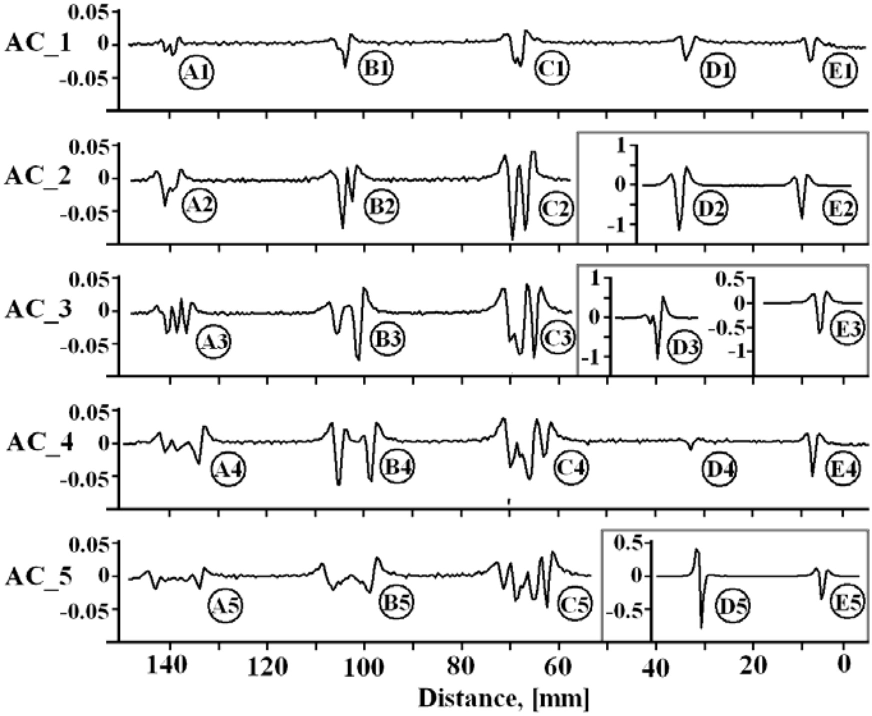

Fig. 3-40 Section view of $\partial V_{RMS}/\partial x$ on each crack at Fig. 3-38

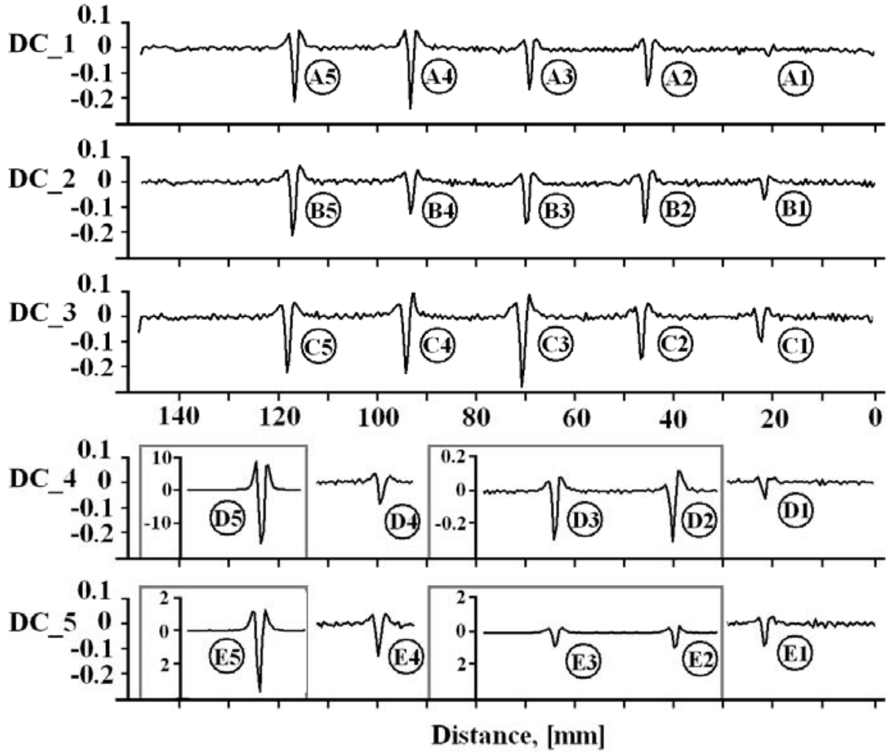

Fig. 3-41 Section view of $\partial V/\partial y$ on each crack at Fig. 3-39

Figs. 3-40 and 41 show the section views of the $\partial V_{RMS}/\partial x$ and $\partial V/\partial y$ distributions on each crack, respectively. Let us express the terms $\partial V/\partial y$ and $\partial V_{RMS}/\partial x$ as $\partial V_H/\partial C$. Ferromagnetic particles such as AISI-1018 and 4340 allow for larger (20 times) $\partial V_H/\partial C$ values at the D2, D3, D5, E2, E3, and E5 locations than in the case of magnetic fluid penetration. This is because of the difference in permeability. The absolute values of maximum and minimum $\partial V_H/\partial C$ (Max[$\partial V_H/\partial C$], Abs[Min[$\partial V_H/\partial C$]]) around each crack increase with increasing crack size. Furthermore, the number of large $\partial V_H/\partial C$s, which are over the average values, increases according to the increase of crack length. Authors proposed a weighting method using the length information in the previous paper [6, 10] expressed as:

$$\left.\frac{\partial V_H}{\partial C}\right|_{TOTAL} = \sum_{i=1}^{L_C/2S}\left[Max\left(\frac{\partial V_{H,i}}{\partial C}\right) + Abs\left(Min\left(\frac{\partial V_{H,i}}{\partial C}\right)\right)\right] \qquad (39)$$

Here L_C represents the crack length on the $\partial V_H/\partial C$ images, shown in Fig. 3-38 and Fig. 3-39. And S represents the spatial resolution (0.5 mm in this chapter). Also, $Max[\partial V_{H,i}/\partial C]$ and $Min[\partial V_{H,i}/\partial C]$ express the large and small values on the $\partial V_H/\partial C$ image around the crack.

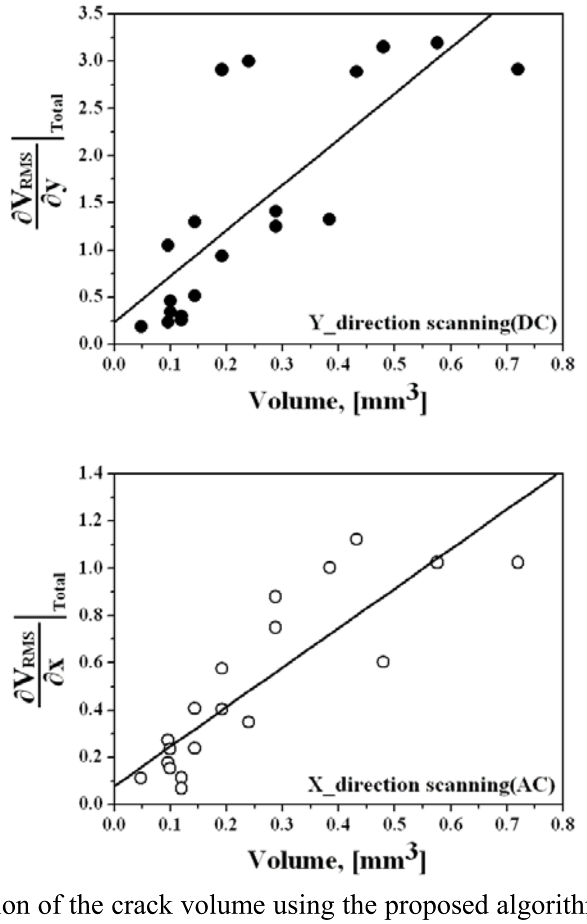

Fig. 3-42 Evaluation of the crack volume using the proposed algorithm without D2, D3, D5, E2, E3, and E5

Fig. 3-42 shows the relationship between the real volume of the crack and $\partial V_H/\partial C|_{total}$, which is calculated using Eq. (39) and L_C. Correspondingly, the crack length and the volume could be evaluated with either the DC-MFL or CIC-MFL methods using the scan magnetic camera with LIHaS and the proposed magnetic fluid penetration method.

A novel method was proposed to detect and evaluate a crack in a paramagnetic material with low electrical conductivity and low magnetic permeability. Magnetic fluid was penetrated into a crack according by capillary action, magnetized by a small yoke-type DC and AC magnetizer, and detected by using the linearly integrated Hall sensor array. A crack on an Inconel 600 specimen of 0.12 mm width, 2 mm length, and 0.2 mm depth was detected at lift-off of 1 mm. Also, the length and volume of each crack were evaluated. These results show that our method can be used to detect and evaluate cracks on non-ferrous and non-metallic materials such as ceramic, composite, and synthetic resins.

E. DISCRIMINATION OF METALLIC COIN

Coins are cast from metals or precious metals, and can be divided into weight currency and mintage. The weight currency mainly uses precious metals such as gold bar or placer gold. Mintages comprise the cast coins, such as gold, silver and copper coinage. The edges of coins are usually rugged for commercial usage. General coins commercialized in each country are less likely to be falsified or modulated than are bills. But, given circumstances in which metal prices acutely increase or currency value depreciates as caused by inflation, coins are often melted for their ore value. Moreover, in case of coins from different countries but with similar shapes and weights, the coins with the lower face value could be used to defraud automatic vending machines at the country where the legitimate coins have a larger face value. The materials used for coinage, *i.e.* gold, silver, copper, bronze, brass, aluminum, zinc, tin, nickel, platinum and rhodium, are all either paramagnetic or ferromagnetic. Therefore, to identify the value or legitimate use of coins in situations in which coins came from all over the world are mixed together and to count the mixed coins, it is currently necessary to depend upon knowledgeable workers to hand-process the work.

The current study concerns the use of a magnetic camera [13, 23] that can automatically separate coins and identify their legitimacy based upon given criteria. As the magnetic source, the method of simultaneous excitation of induced current and magnetic flux leakage, the Combined Induced Current –Magnetic Flux Leakage Method [9] was applied. A linearly integrated Hall sensor array (LIHaS) [34] on a wafer was used in a scanning-type magnetic camera [9, 34] to detect mixed coins with ferromagnetic, paramagnetic and combined ferro-paramagnetic compositions. An algorithm using the test data was subsequently suggested in order to separate the mixed coins. Through the experiments on coins originating from around the world, the utility of the suggested algorithm was verified.

1. ***Prologue***

In particular, when the test material is paramagnetic, the yoke-type coil induced current operated by alternating current, has been used frequently. Since the scanning-type magnetic camera considers the movement of specimens over the sensor head, it is not necessary for the magnetic sensor to be arrayed in 2 dimensions. Specifically, when the Hall sensor arrayed on the wafer (LIHaS) was used, a magnetic image of spatial resolution as high as 0.52 mm could be rapidly acquired.

Fig. 3-43 (a) and (b) are diagrams of a small yoke type electromagnet to realize the CIC-MFL Method. The axis of the LIHaS sensor array was selected to be along the y-axis, the scan direction was selected to be along the x-axis and the direction normal to the specimen's surface was selected to be along the z-axis. If a yoke-type electromagnet is installed at the back of the LIHaS, a magnetic flux is developed between the prongs of the electromagnet in the x-direction. The input of alternating current to the electromagnet generates an induced current that is perpendicular (*i.e.* in the ±y-direction) to the magnetic field lying in the x-direction, regardless of the coin material constituting the xy-surface as illustrated in Fig. 3-43 (b).

Induced currents of this kind cause eddy currents to develop at the edges of the coin, which in turn generate a magnetic field in z-direction. The strength of the electromagnetic field developed at that time will be stronger as the edge of the coin approaches being perpendicular to the axis of the of the LIHaS array. Accordingly, with the introduction of a CIC-MFL yoke together with a LIHaS array that both have their long axes oriented in the y-direction, ferromagnetic and paramagnetic coins could be detected.

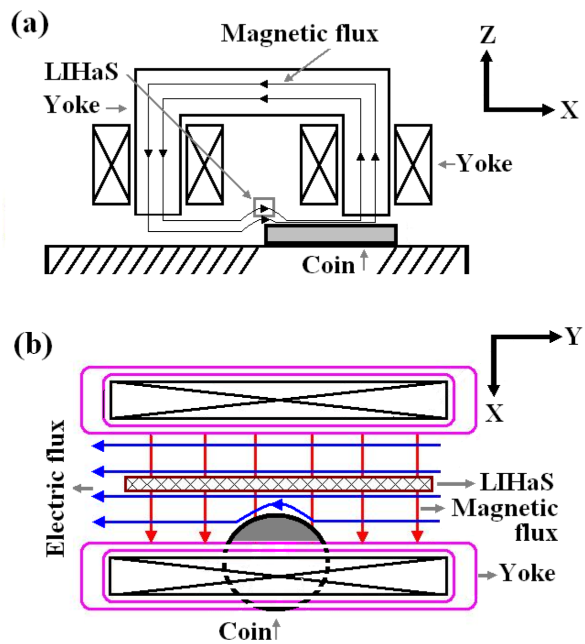

Fig. 3-43 Small size yoke type electromagnetic coil operated by alternative current.

In the CIC-MFL Method, the detection of alternating magnetic field is necessary, and the amplitude of each Hall voltage output from the LIHaS is proportional to the disturbance of induced current or to the magnetic flux leakage strength. Therefore, the root-mean-square (RMS) circuit [9] was used to effectively extract the amplitude of Hall voltage.

Namely, an independent RMS circuit was connected at each Hall element of LIHaS to extract the signal that corresponds to the amplitude of the alternating magnetic field (V_{RMS}). In addition, previous studies reported that the differentiated value ($\partial V_{RMS}/\partial x$) toward the scanning direction of V_{RMS} provides useful information to effectively detect and evaluate the change of magnetic field change.

2. ***Specimens***

To verify the utility of coin detection and separation by using CIC-MFL and LIHaS techniques, the coins listed in Table 6 were tested. It was not possible to test all coins from all countries, but the diameter, thickness, weight of these selected coins were all comparable to the Korean 100 won coin. The lift-off for all coin tests was set at 1mm.

Table 6 Coins(KR:Korea, EU:Europe, US:United Stated, JP:Japan, CH:China, PL:Poland, IN:Indonesia, NZ:Newzland, GM:Germany, EL:England)

	Unit	Diameter [mm]	Weight [g]	Thickness [mm]	Value	Mark
KR	10 won(a)	22.87	4.08	1.49	0.1	■
	10 won(b)	18.03	1.24	1.38	0.1	□
	50 won	21.61	4.17	1.59	0.5	⊞
	100 won	23.99	5.44	1.56	1	⊠
	500 won	26.51	7.77	1.89	5	⊟
EU	5 cent	21.29	3.95	1.07	0.71	●
	10 cent	19.72	4.14	1.90	1.43	○
	20 cent	22.26	5.76	2.07	2.85	⊕
	50 cent	24.25	7.77	2.40	7.12	⊗
	1 euro	23.30	7.54	2.35	14.2	⊖
US	1 cent	19.02	2.80	1.45	0.09	▲
	5 cent	21.25	4.93	1.86	0.47	△
	1 dime	17.90	2.26	1.30	0.94	
	25 cent	24.14	2.62	1.75	2.34	
JP	1 yen	20.02	1.01	1.48	0.09	▼
	5 yen	22.03	3.77	1.51	0.45	▽
	10 yen	23.52	4.52	1.52	0.90	
	50 yen	20.96	4.04	1.75	4.51	
	100 yen	22.58	4.82	1.68	9.03	
	500 yen	26.50	7.03	1.82	45.2	
CH	5 jiao	20.51	3.84	1.67	0.13	◆
	1 yuan	25.03	6.05	1.83	1.32	◇
PL	1 grosze	15.47	1.64	1.24	0.04	◀
	2 grosze	17.56	2.15	1.28	0.08	◁
	5 groszy	19.31	2.60	1.27	0.19	
	10 groszy	16.44	2.51	1.57	0.38	
	50 groszy	20.50	3.94	1.65	1.92	
	1 ztoty	22.81	5.07	1.68	3.85	
	2 ztoty	21.54	5.22	1.97	7.69	

IN	100 rupiah	23.00	1.82	1.96	0.10	
	200 rupiah	25.03	2.40	2.29	0.21	
	500 rupiah(a)	27.19	3.13	2.25	0.52	
	500 rupiah(b)	24.04	5.38	1.82	0.52	
NZ	5 cent	19.29	2.86	1.26	0.37	
	20 cent	28.53	11.28	2.24	1.51	
	50 cent	31.68	13.71	2.31	3.76	
	1 dollar	23.01	8.11	2.64	7.52	
GM	50 pfennig	20.00	3.52	1.58	3.02	
	1 mark	23.61	5.52	1.69	6.03	
EL	5 pence	17.96	3.26	1.67	0.96	
	20 pence	21.38	5.02	1.75	3.73	
	1 pound	22.53	9.56	3.18	18.6	
	2 pound	28.42	12.00	2.53	37.3	

3. *Discussions*

Fig. 3-44 illustrates the actual image of coins from each country listed in Table 6 and the result of differentiated RMS signal voltage, $\partial V_{RMS}/\partial x$ in the scanned direction (x-direction). These values were determined after acquiring the V_{RMS} around the fault by means of the Hall sensor and RMS circuit and after applying a 1 kHz current to the yoke-type electromagnet, as illustrated in Fig. 3-34. In addition, Fig. 3-44 shows a cross-sectional diagram of $\partial V_{RMS}/\partial x$ taken through the central part of the coins. It is evident that the maximum gradient values, ($\partial V_{RMS}/\partial x|_{MAX}$), were for the most part detected at both edges of the coins and that the lowest values, ($\partial V_{RMS}/\partial x|_{MIN}$), were detected at the central parts of the coins. However, the 1-euro, and the 1-yuan pieces all showed anomalous results compared to the other coins.

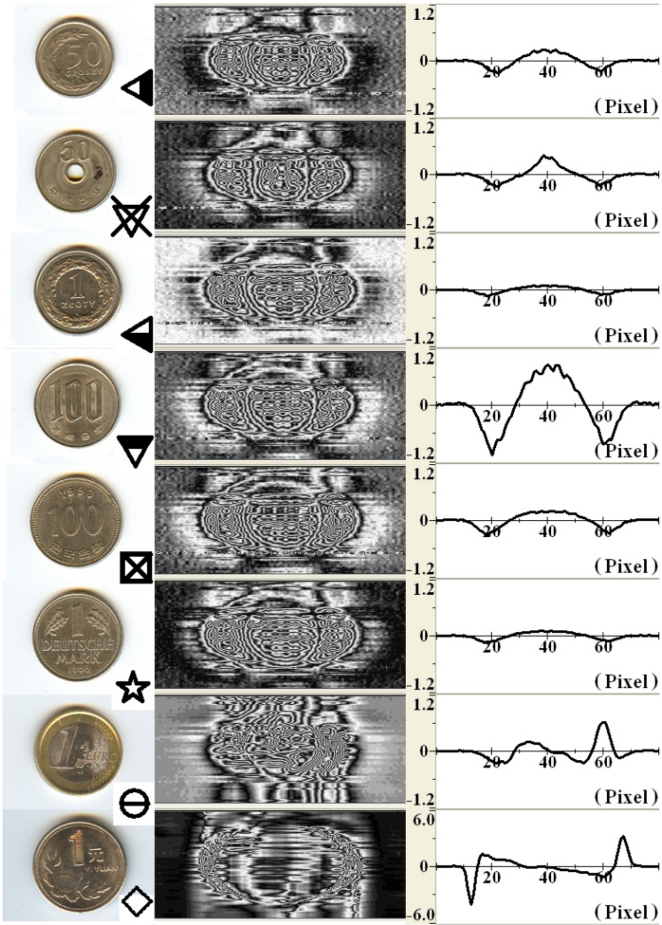

Fig. 3-44 Coins, $\partial V_{RMS}/\partial x$ images and section view

These results were attributed to the use of different coin materials at the central and outer rings of the 1-euro coin. Moreover, the ferromagnetic composition is mixed in the case of the 1–yuan coin. Consequently, the resultant magnetic flux leakage that is relatively stronger than the induced current has a major effect on the measurement results. Accordingly, the signal from the 1-yuam, 5jiao and Europe 5 cent are approximately ten times larger than the signals acquired from the other coins.

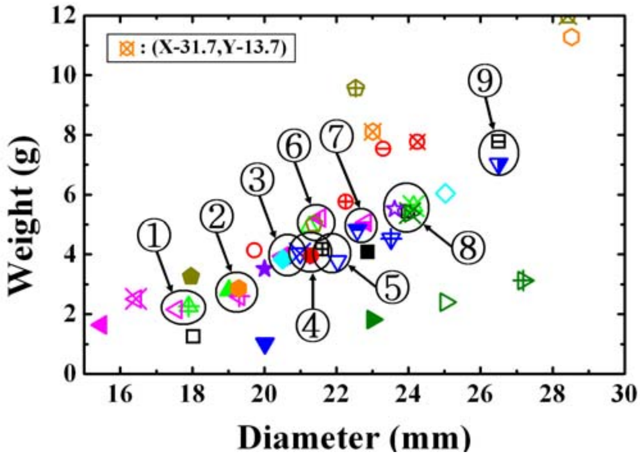

Fig. 3-45 Diameters and weight of each coin. Group① is PL-2grosze(◁) and US-1dime(⟰). Group② is US-1cent(▲), NZ-5cent(⬣), and PL-5groszy(⟴). Group③ is PL-10groszy(⋇), CH-5jiao(◆), and JP-50yen(⋇). Group④ is JP-50yen(⋇), EU-5cent(●), and KR-50won(⊞), Group⑤ is KR-100won(⊠), and JP-50yen(⋇). Group⑥ is US-5cent(△), EL-20pence(⬠), and PL-2ztote(◂). Group⑦ is JP-100yen(▿), and PL-1ztoty(◂). Group⑧ GM-1mark(☆), KR-100won(⊠), US-25cent(⋇), and IN-500rupiah(b)(⋇). Group⑨ is KR-500won(⊟), and JP-500yen(▾).

Fig. 3-45 illustrates the actual diameter and weight of the coins used in the test. A conventional coin discrimination-coin counting machine operates only on the basis of the diameter and weight of the coin. Graphically, the PL-2grosze together with the US-1dime and the US-1cent together with NZ-5cent, PL-5groszy and the PL-10groszy together with the CH-5jiao, the JP-50yen and the JP-50yen together with the EU-5cent, the KR-50won and the KR-100won together with the JP-50yen and the US-5cent together with the EL-20pence, the PL-2ztote and the JP-100yen together with the PL-1ztoty and the GM-1mark together with the KR-100won, the US-25cent, the IN-500rupiah(b) and KR-500won together with the JP-500yen are located close enough to cause trouble in the discriminating between them. Note that the NZ -5 cent and US-1 cent differ by a factor of four in value. Similarly, the values of the ID 500-rupiah and US-25 cent differ by a factor of 4.5. The ID 500-rupiah and GM 1-mark differ in value by a factor of 13. The KR 500-won and the JP 500-yen have an approximate eight times difference in value and also the highest risk of falsification. Actually in Japan, KR the 500-won has been used at vending machines after reducing its weight by drilling a small hole through it. The problem can thus be seen to have sociological overtones.

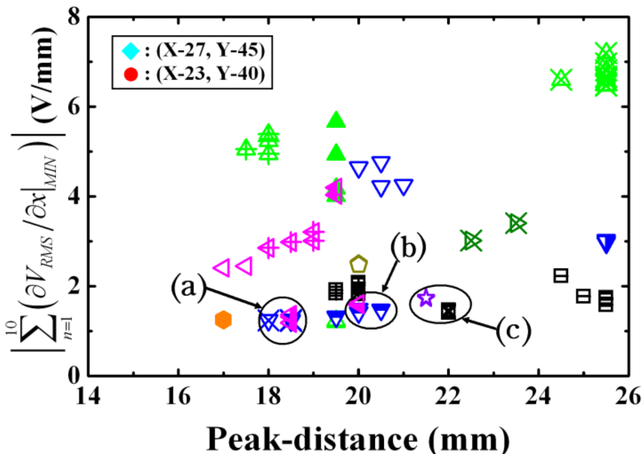

Fig. 3-46 Relationship between the peak-distance and the integrated absolute minimum value of the $\partial V_{RMS}/\partial x$

As shown in Fig. 3-46, coins can be distinguished easily by using peak-distance and SV, which is given by the following expression Eq. (40):

$$SV = \left| \sum_{n=1}^{10} \left(\partial V_{RMS} / \partial x |_{MIN} \right) \right| \tag{40}$$

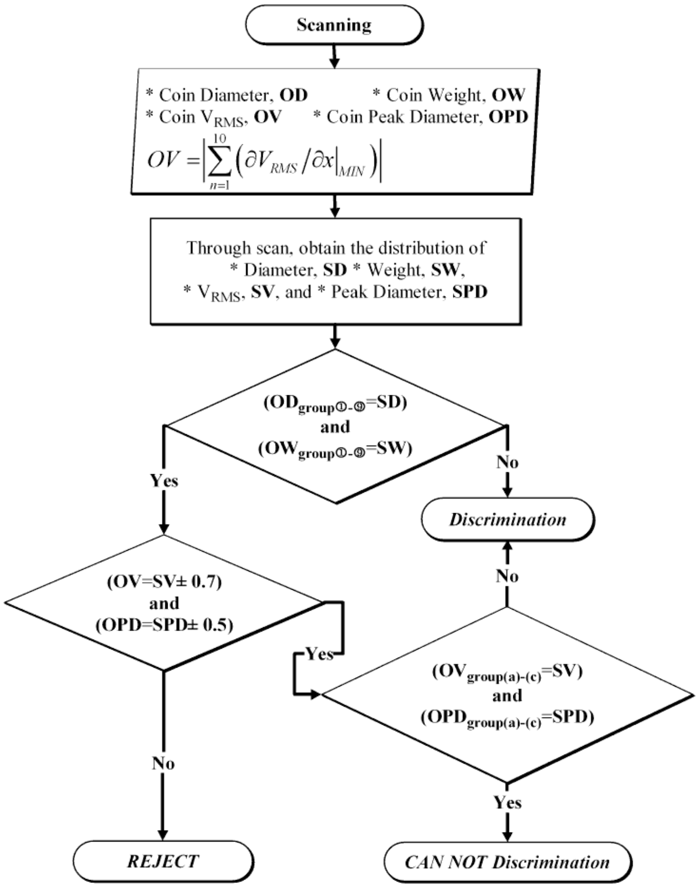

Fig. 3-47 Coin discriminating algorithm.

Fig. 3-47 is a coin differentiation algorithm established from the experiment results of Fig. 3-45 and Fig. 3-46. From the $\partial V_{RMS}/\partial x$ data that were acquired after scanning the coins by the LIHaS and CIC-MFL method at the lift-off the maximum and minimum values are extracted. After determining the peak distances, $\partial V_{RMS}/\partial x|_{MAX}$ and $\partial V_{RMS}/\partial x|_{MIN}$, coins are differentiated according to the algorithm. Following this coin differentiation algorithm, 85 coins comprising 43 denominations from total the ten countries listed as in Table 6 were tested and showed a 90.7 % rate of successful identification. Only the PL-50zroszy together with the JP-50yen, and the PL-1ztoty together with the JP-100yen could not identified.

IV. **CONCLUSIONS**

In this paper, A system for nondestructive evaluation using alternative electro-magnetic field model analysis and the scan type of the magnetic camera has proposed. The evaluation results show that the proposed algorithm can be used to detect and evaluate cracks such as the followings.

1. A nondestructive evaluation method for cracks occurring on the surface of austenitic stainless steel with δ-ferrite structure in real time was proposed. A sheet type current was induced on a specimen, and was distorted around both tips of the crack on the specimen. Also, high-pass-filters and root-mean-squared circuits were introduced to obtain the amplitude of the distorted current around the tips of the crack. The crack was inspected in real time by using HSA, which were arrayed in 3.5 mm spatial resolution. The distribution of $DRMS_{HIGH}$ was obtained by SSS. Nondestructive evaluation (NDE) algorithm was obtained by using $DRMS_{HIGH}$, the differential value $\partial(D_{HIGH})/\partial x$, the maximum value of $\partial(D_{HIGH})/\partial x$, the interval between the maximum position and minimum position (Diameter[$\partial(D_{HIGH})/\partial x$]) in the $\partial(D_{HIGH})/\partial x$, and the distance between each set of maximum positions (Distance[$\partial(D_{HIGH})/\partial x$].

The $\partial(D_{HIGH})/\partial x$ is easier to evaluate than $DRMS_{HIGH}$ because of its vivid distribution without bias. And Max[$\partial(D_{HIGH})/\partial x$], Distance[$\partial(D_{HIGH})/\partial x$] and Diameter[$\partial(D_{HIGH})/\partial x$] were selected as the NDE factors. The crack parameters, such as the depth, width, length, section area, and volume of the crack, can be calculated by equations, which were derived from the relationship between the NDE factors and the crack morphologies. And, the estimative equations of the depth, width, length, section area and volume are applied to evaluate cracks by using HSA. The application of Max[$\partial(D_{LOW})/\partial x$], which was obtained by using HSA instead of the Max[$\partial(D_{HIGH})/\partial x$], permitted large errors. However, the qualitative relationship between the calculated crack volumes and the real crack volumes was permitted, in spite of the large errors due to the spatial resolution of the arrayed Hall sensors. Therefore, the NDE of the cracks obtained by using HSA can be expected when the spatial resolutions can be secured.

2. A sheet type induced current on the specimen and single Hall sensor scanning are used to inspect and evaluate a crack quantitatively on a paramagnetic aluminum alloy. A crack can be inspected by using the distribution of RMS Hall voltages caused by the alternate magnetic flux leakage around the crack tips. Alternate magnetic flux leakage occurs from distortion of the sheet type induced current at the crack tips. The angle between the depth directional crack edge and the surface of a specimen can be obtained by using the distance between the inflection points of the distribution of the RMS magnetic flux leakage and their processed results. The real length of crack can be calculated using an empirical equation that uses the distance between the peak of the root mean squared Hall voltages at the 3.2 kHz and the calculated crack tip angle. Conversely, the volume and the section area of the crack can be estimated quantitatively by using the average of 50 maximum values of the V_{RMS}, $\partial V_{RMS}/\partial x$, $\partial V_{RMS}/\partial y$ and $\partial^2 V_{RMS}/\partial x \partial y$ distribution.

3. An inspection and evaluation method for cracks on a cold rolled steel plate was proposed. The slit type crack could be detected independent of the length direction by using an improved magnetic source; that is, the Combined induced current, the magnetic flux leakage, and the linearly integrated InSb Hall sensor array on a NiZn ferrite wafer. The hole-type crack, with 0.2 mm of diameter and depth, respectively, could be detected on a lift-off 0.6 mm. The slit type crack, with 2, 0.3, and 0.1 mm of length, width, and depth, could be detected, also. The calculated $\partial V_{RMS}/\partial x|_{total}$, obtainable from experimental data, showed a good relationship with the real crack volume.

4. A novel method was proposed to detect and evaluate a crack in a paramagnetic material with low electrical conductivity and low magnetic permeability. Magnetic fluid was penetrated into a crack according by capillary action, magnetized by a small yoke-type DC and AC magnetizer, and detected by using the linearly integrated Hall sensor array. A crack on an Inconel 600 specimen of 0.12 mm width, 2 mm length, and 0.2 mm depth was detected at lift-off of 1 mm. Also, the length and volume of each crack were evaluated. These results show that our method can be used to detect and evaluate cracks on non-ferrous and non-metallic materials such as ceramic, composite, and synthetic resins.

5. The $\partial V_{RMS}/\partial x$ data that were acquired after scanning the coins by the LIHaS and CIC-MFL method at the lift-off the maximum and minimum values are extracted. After determining the peak distances, $\partial V_{RMS}/\partial x|_{MAX}$ and $\partial V_{RMS}/\partial x|_{MIN}$, coins are differentiated according to the algorithm. Following this coin differentiation algorithm, 85 coins comprising 43 denominations from total the ten countries listed as in Table 6 were tested and showed a 90.7% rate of successful identification. Only the PL-50zroszy together with the JP-50yen, and the PL-1ztoty together with the JP-100yen could not identified.

REFERENCE

[1] Investigation Report on Pipe Rupture Incident at Hamaoka Nuclear Power Station Unit-1, July 2002, Nuclear and Industrial Safety Agency (NISA), Ministry of Economy, Trade and Industry (METI), Japan

[2] Job, Macarthur and Steve Swift. JAL 123: 520 Lost - It's 20 years since the world's worst single aircraft airliner accident. In: Flight Safety Australia. - Vol. 9, no. 4 (July, August 2005) page 28-33. [http://www.casa.gov.au/fsa/2005/aug/28-33.pdf],

[3] Applying Lessons Learned From Accidents: Accident/Incident Summary Japan Airlines Flight 123, Boeing 747, Gunma Prefecture Japan, Flight International 14.09.1985 (4-7)

[4] http://www.absoluteastronomy.com/topics/Eschede_train_disaster#encyclopedia

[5] Masayuki Nakao, Failure knowledge database / 100 selected cases

[6] Jiseong Hwang, Jinyi Lee and Sukjin Kwon, "The Application of a Differential Type Hall Sensors Array to the Nondestructive Testing of Express Train Wheels", NDT & E International, 42(1)(2009.1), pp.34-41.

[7] Jongwoo Jun and Jinyi Lee, "Nondestructive evaluation of a crack on austenitic stainless steel using the sheet type induced current and the Hall sensor array", Journal of Mechanical Science and Technology, 22(9)(2008.9), pp.1684-1691.

[8] Jinyi Lee, Jiseong Hwang, Jongwoo Jun and Seho Choi, "Nondestructive Testing and Crack Evaluation of Ferromagnetic Material by Using the Linearly Integrated Hall Sensor Array", Journal of Mechanical Science and Technology, 22(12)(2008.12), pp.2310- 2317.

[9] J. Jun, J. Lee, and D. Park, "NDT of a nickel Inconel specimen using by the complex induced current - magnetic flux leakage method and linearly integrated hall sensor array", Journal of the Korea Society for Nondestructive Testing, Korea, 27(2007.10), pp. 375-382.

[10] Jiseong Hwang, Jongwoo Jun, Seho Choi, Cheolwoong Kim, Kazuhiro Ogawa and Jinyi Lee, "A Study of Magnetic Charge per Unit Area of Dipole Model for the NDE", Key Engineering Materials, 353-358 (2007.9), pp.2371-2374.

[11] Jinyi Lee, Jongwoo Jun, Jiseong Hwang and Sehoon Lee, "Development of Numerical Analysis Software for the NDE by using Dipole Model", Key Engineering Materials, 353-358 (2007.9), pp.2383-2386.

[12] Jongwoo Jun, Jiseong Hwang, Keejoo Kim, Kazuhiro Ogawa and Jinyi Lee, "Development of Signal Processing Circuit of a Magnetic Camera for the NDT of a Paramagnetic Material", Key Engineering Materials, 353-358 (2007.9), pp.2379-2382.

[13] Jinyi Lee, Jiseong Hwang, Kyungchul Lee, Seho Choi, "A Study of Leakage Magnetic Flux Detector Using Hall Sensors Array", Key Engineering Materials, 306-308 (2006.3), pp.235-240.

[14] Jinyi Lee, Jiseong Hwang, Seho Choi, Jaekyu Lim, "Detection Probability Improvement for Nondestructive Evaluation Using a Magnetic Camera", Key Engineering Materials, 306-308 (2006.3), pp.241-246.

[15] Jinyi Lee, Jiseong Hwang, "The Detection Probability Improvement of the Far-Side Crack on the High Lift-off Using the Magnetic Camera", International Journal of Modern Physics B, 20(25-27), (2006), pp.4631-4636.

[16] Jinyi Lee, Jiseong Hwang, Seho Choi, "The QNDE Using Image Processing of the Magnetic Camera ", International Journal of Modern Physics B, Vol.20, Nos.25-27, (2006), pp.4625-4630.

[17] Jinyi Lee, Jiseong Hwang, "A Study of the Quantitative Nondestructive Evaluation Using the Cross Type Magnetic Source", Key Engineering Materials, 321 (2006), pp.1447-1450.

[18] Jiseong Hwang, Jinyi Lee, "Modeling of a Scan Type Magnetic Camera Image Using the Improved Dipole Model", JMST, 20(10), (2006), pp.1691-1701.

[19] 이진이, 황지성, 송하용, "마이크로프로세서를 이용한 자기카메라 전용 임베디드형 AD 변환기 및 잡음 감소에 관한 연구", 한국비파괴검사학회지, 26(2), (2006.4), pp.99-107.

[20] Jinyi Lee, Dowon Seo, Tetsuo Shoji, "Numerical Consideration of Magnetic Camera for

Quantitative Nondestructive Evaluation", Key Eng. Mat., 270(1) (2004.10), pp.630-635.

[21] Jinyi Lee, etc., "A display apparatus of magnetic flux density using 2D array magnetic sensor and 3D magnetic fluid", Korea, 10-0376892-0000 (Mar. 7, 2003).

[22] Jinyi Lee, etc., "Magnetic flux density apparatus for, e.g., detecting an internal crack of a metal or a shape of the metal", US 6,683,452 B2, (Jan. 27, 2004).

[23] Jinyi Lee, Jongwoo Jun, Jiseong Hwang, "Magnetic sensor array and apparatus for detecting defect using the magnetic sensor array", PCT/KR2007003801, (May. 8, 2008).

[24] 이진이, 전종우, "자성유체 침투에 의한 상자성체 비파괴검사", 2008년도 한국비파괴검사학회 춘계학술대회 논문집, (2008), pp.223-228.

[25] 이진이, 김정민, 전종우, 황지성, "원통형 자기카메라에 관한 기초연구", 2008년도 한국비파괴검사학회 춘계학술대회 논문집, (2008), pp.247-252.

[26] Jinyi Lee, Dowon Seo, Tetsuo Shoji, "Theoretical Consideration of Nondestructive Testing by use of Vertical Magnetization and Magneto-Optical Sensor", KSME International,18(4) (2004.4), pp.640-648.

[27] Jinyi Lee, Jongwoo Jun, "NDT of the crack on the austenite stainless steel using the improved sheet type induced current and the linearly integrated Hall Sensor Array", Abstracts of 13th ENDE, (2008.5), p.48.

[28] Dogaru T, Smith ST., "Giant magnetoresistance-based eddy-current sensor", IEEE Trans Magn. 37(5), (2001), pp.3831-3838.

[29] Smith CH, Schneider RW, Dogaru T, Smith ST, "Eddy-current testing with GMR magnetic sensor arrays", AIP Conf Proc 657(1), (2003), pp.419-426.

[30] Jinyi Lee, Jongwoo Jun, "Quantitative Nondestructive Evaluation of Fatigue Crack on the Aluminum Alloy Using by Magnetic Camera", NDT&E Int., (2008), contribute.

[31] Jinyi Lee, Jongwoo Jun, "Nondestructive Evaluation of the Rivet Connection Parts in Aging Aircraft Using a CIC-MFL and LIHaS", NDT&E Int., (2008), contribute.

[32] (사)일본항공기술협회, “항공기재료”, (1993).

[33] Jinyi Lee, Jongwoo Jun, "Nondestructive Evaluation of Cracks in a Paramagnetic Specimen with Low Conductivity by Penetration of Magnetic Fluid", NDT&E International, (2008), contribute .

[34] J. Hwang, J. Lee, J. Jun, R. Wang, S. Choi, and S. Hong, "Scan type magnetic camera images with a high spatial resolution for NDT obtained by using a linearly integrated hall sensor array", Proceedings of IEEE International Workshop on Imaging Systems and Techniques, Poland: Krakow, 1-6, 2007.

[35] J.Y. Lee, J.S. Hwang and T. Shoji, "Numerical Analysis of Magneto-Optical Eddy Current Imaging Using FEM, Key Engineering Materials", Korea, 306~308 (2006) 235-240.

[36] D.K. Thome, G.L. Fitzpatrick, R.L. Skaugset and W.C.L. Shih, "Aircraft Corrosion and Crack Inspection Using Advanced Magneto-Optic Imaging Technology", The International Society for Optical Engineering- SPIE Proceedings, 2945 (1996) ,pp.365-373.

[37] H. Fukuoka, et. al, "Nondestructive Evaluation", Journal of the Japanese Society for Non-destructive Inspection JSNDI, Tokyo, Japan (1998) 86.

[38] J. Panaitov, H. Krause and Y. Zhang, "Pulsed eddy current transient technique with HTS SQUID magnetometer for non-destructive evaluation", Physics C, 372-376 (2002) , pp.278-281.

[39] Oxygen-free copper—Manual 2007 CAT.NO.CE100A (Japan : HITACHI)

[40] Hwang DY. "Damage Tolerance Design and Prediction of Fatigue Life in Aircraft Structure", KSME Int J 1995;35(6), pp.468-480.

[41] Goranson UG, "Damage Tolerance – Facts and Fiction", Proceedings of the 17th Symposium of the International Committee on Aeronautical Fatigue. Stockholm, (1993).

[42] Jun JW, Hwang JS, Lee JY, "Nondestructive Testing of the Paramagnetic Materials Using a Hall Sensor", Proceedings of the KSME 2006 Fall Conference (2006), pp.1-6.

[43] Lee JY, Jun JW, Hwang JS. Patent Pending KR 10-2006-0107338, 2006.

[44] Jun JW, Hwang JS, Lee JY, "Quantitative Nondestructive Evaluation of the Crack on the

Austenite Stainless Steel Using the Induced Eddy Current and the Hall Sensor Array", 2007 IEEE Instrumentation and Measurement Technology Conference Proceedings. Warsaw, (2007); #7085.

[45] Fitzpatrick GL, Thome DK, Skaugset RL, Shih WCL, Shih EYC. "Magneto-Optic/Eddy Current Imaging of Aging Aircraft: A New NDI Technique", Materials Evaluation, 51(12)(1993), pp.1402-1407.

[46] Singh W.S., Rao B.P.C., Vaidyanathan S., Jayakumar T and Raj B, "Detection of leakage magnetic flux from near-side and far-side defects in carbon steel plates using a giant magneto-resistive sensor", Measurement Science and Technology, 19(2008), pp. 1-8.

[47] Gosselin SR, Simonen FA, Healer PG, Doctor SR, "Fatigue Crack Flaw Tolerance in Nuclear Power Plant Piping ", A Basic for Improvements to ASME Code Section XI Appendix L.(2007).

[48] Bao G, Shinozaki K, Iguro S, Inkyo M, Yamamoto M, Mahara Y, Watanabe H, "Stress corrosion cracking sealing in overlaying of Inconel 182 by laser surface melting", J Mater Process Tech 173(2006), pp.330-336.

[49] Chubachi R, Nakatsuka K, Shimoiizaka J, "Influence of Temperature and pH on the Dispersion Stability in Water Base Magnetic Fluids", J Japan Soc of Powder and Powder Metallurgy 23(6)(1976), pp. 21-25.

[50] Paul A. T., Physics, Worth Publishers (1987).

ACKNOWLEDGMENTS

어제 인생의 또 다른 방향으로의 결심을 하고 광주에 온 것 같은데 벌써 몇 해가 지났습니다. 주위의 많은 분들 덕분에 여기까지 올 수 있었다고 생각합니다. 학교로 올 수 있는 결심을 하게 해주시고, 항상 진심으로 보살펴주시는 이진이 지도 교수님께 정말 감사합니다. 인생을 오래 살지는 않았지만 뒤 돌아보면 교수님을 만난 것 제 인생에 가장 행운인 것 같습니다. 살면서 꼭 좋은 모습으로 보답하겠습니다. 좋은 논문이 될 수 있게 논문을 심사해 주시고, 많은 가르침을 주신 고낙용 교수님, 박종안 교수님, 반성범 교수님 그리고, ㈜포스코의 최세호 박사님께도 정말 감사하다는 말 전하고 싶습니다. 대학원 과정에 많은 가르침을 주셨던 김영동 교수님, 최한수 교수님, 장순석 교수님, 곽근창 교수님 그리고, 조창현교수님께도 감사의 마음 전하고 싶습니다. 많은 시험편과 연구결과에 많은 관심과 격려해주신 ㈜ POSCO 기술연구소의 최세호 박사님, 김구화 박사님, 오기장 박사님께 깊은 감사 드립니다. 그리고, 저희들의 연구를 믿고 많은 부분에 적용할 수 있게 배려해 주신 한국철도기술연구원의 권석진 박사님, 유원희 박사님, 서정원 박사님께도 감사 드립니다. 많은 관심과 격려 및 다양한 시험편을 제공하여 주신 한국원자력 연구원의 박덕근 박사님께도 감사 드립니다. 항상 기분 좋은 모습으로 많은 지원 아끼지 않았던 ㈜네드텍의 이주섭 사장님께 감사하다는 말 전하고 싶습니다. 그리고, 많은 관심 가져주신 공군 군수사령부 한성주 사령관님과 공군 항공기술연구소의 이경찬 소장님, 황영하 실장님께도 감사 드립니다. 국방대학교의 신기수 교수님, 두산중공업의 류승우 차장님, ㈜ 삼성전기의 정호철 부장님, 장기훈 대리님, 이상진과장님, 앰코테크놀로지코리아㈜의 최호민 부장님께도 진심으로 감사 드립니다. 그리고, RIST의 정우철 박사님께도 진심으로 감사 드립니다. 연구비를 지원해주신 한국과학재단, 철도기술연구원, ㈜포스코, ㈜네드텍 그리고, 지식경제부 관계자 여러분께 깊은 감사 드립니다. 밤 늦게까지 항상 같이 있었던 황지성, 조현종, 박영민, 최호윤 그리고, 김정민 정말 고맙고 감사합니다. 그리고, 6층의 모든 랩실의 대학원생

및 후배들께도 정말 감사하다는 말 전하고 싶습니다. 너무 착하고 좋은 후배들을 만나 힘든 시간들이 아니라, 아주 즐겁고 좋은 시간들이었습니다. 한 명씩 이름은 적지 못하지만 제 마음속에 새기도록 하겠습니다. 항상 부족한 저를 믿고, 격려해 주시는 장인, 장모님께 깊은 감사 드립니다. 형님, 형수, 누나, 자형들께도 정말 고맙다는 말 전하고 싶습니다. 마지막으로 2년 반을 애들 돌본다고 고생한 선영이와 아빠없이 외롭게 지낸 아들 재영이와 딸 예솔이에게 사랑한다는 말 전하고 싶습니다.

저작물 이용 허락서

학 과	정보통신공	학 번	20067608	과 정	박사
성 명	한글: **전 종 우** 한문: 全 鍾 虞 영문: Jun Jongwoo				
주 소	**부산시 수영구 망미2동 수영강변대림**ATP 105**동** 1903**호**				
연락처	E-MAIL : jongwoo119@korea.com				
논문제목	한글 : **교류 전자기장 가시화 시스템의 개발 및 응용** 영문 : Development and Application of Visualization System of Alternative Electro-Magnetic Field				

본인이 저작한 위의 저작물에 대하여 다음과 같은 조건아래 조선대학교가 저작물을 이용할 수 있도록 허락하고 동의합니다.

- 다 음 -

1. 저작물의 DB구축 및 인터넷을 포함한 정보통신망에의 공개를 위한 저작물의 복제, 기억장치에의 저장, 전송 등을 허락함
2. 위의 목적을 위하여 필요한 범위 내에서의 편집・형식상의 변경을 허락함. 다만, 저작물의 내용변경은 금지함.
3. 배포・전송된 저작물의 영리적 목적을 위한 복제, 저장, 전송 등은 금지함.
4. 저작물에 대한 이용기간은 5년으로 하고, 기간종료 3개월 이내에 별도의 의사 표시가 없을 경우에는 저작물의 이용기간을 계속 연장함.
5. 해당 저작물의 저작권을 타인에게 양도하거나 또는 출판을 허락을 하였을 경우에는 1개월 이내에 대학에 이를 통보함.
6. 조선대학교는 저작물의 이용허락 이후 해당 저작물로 인하여 발생하는 타인에 의한 권리 침해에 대하여 일체의 법적 책임을 지지 않음
7. 소속대학의 협정기관에 저작물의 제공 및 인터넷 등 정보통신망을 이용한 저작물의 전송・출력을 허락함.

동의여부 : 동의(●) 반대( )

2009년 2월 일

저작자: **전 종 우** (서명 또는 인)

조선대학교 총장 귀하